2015

Modelling of Channelization in Unconsolidated Formations Due to Liquid Injection

Juan Felipe Bautista Barake
Louisiana State University and Agricultural and Mechanical College, jbauti5@lsu.edu

MODELLING OF CHANNELIZATION IN UNCONSOLIDATED FORMATIONS DUE TO LIQUID INJECTION

A Thesis

Submitted to the Graduate Faculty of the
Louisiana State University and
Agricultural and Mechanical College
in partial fulfillment of the
requirements for the degree of
Master of Science in Petroleum Engineering

in

The Department of Petroleum Engineering

by
Juan Felipe Bautista Barake
B.S., Universidad de los Andes, 2013
December 2015

ACKNOWLEDGEMENTS

I would like to express my infinite gratitude to Dr. Arash Dahi for his guidance and unconditional support through my studies at Louisiana State University. I thank Dr. Julius Langlinais, Dr. Seung Kam and Dr. George Wang for all the guidance and constructive discussions provided through this process.

I would like to thank my parents and my sister who have always provided me with their endless love and support which are crucial to my personal, academic and professional life.

Finally, I would like to thank my friends, especially Sandeep Gupta, Ana Li, Darko Kupresan, Erin McCreery, John Whitehead and Catalina Posada for being an essential part of my life balance over the past two years.

TABLE OF CONTENTS

LIST OF TABLES

LIST OF FIGURES

ABSTRACT

Fluid injection has been increasingly implemented in oil and gas producing fields to optimize hydrocarbon production in both young and mature oil fields across the globe. This situation arises from the realization that early planning of second and tertiary recovery methods may improve project economics significantly. Injectors are then intended to perform at high injection rates with low bottomhole flowing pressures for as long as possible. In the case of injectors drilled in unconsolidated formations, deficient performance often times seems to be the norm. With a majority of these fields being offshore developments in which capital expenditures are high, a profound need for solutions arises.

From a wide range of problems leading to injectivity impairment in injectors targeting poorly consolidated formations, research on rock failure caused by fluid injection operations appears to be at its earliest stages hence it is the main subject of the present study. Some studies trying to address this issue intend to modify existing fracture mechanics theory to explain rock failure. Although many of the proposed theories properly explain some observations and are founded on well derived scientific principles, they fail to explain formation sand erosion and transportation often perceived at these wells.

To study poorly cemented sands' failure, dynamic fluid flow equations are implemented using Finite Element Methods coupled to an erosional model. Different scenarios are implemented in two and three dimensions. It can be seen from the study that the drag forces created by injecting fluid weaken and damage the target formation. The damage caused is consequence of the pressure gradient as the fluid travels through the porous media. The latter observation leads to the conclusion that limiting injection rates to avoid damage may not be sufficient and a more appropriate approach is to control the fluid velocity at the sandface given a fluid viscosity, relative permeability and porosity. If proper injection parameters are achieved, the injectivity declines in these wells can be minimized. The observations from this study can be used to better design wells and how to complete them.

CHAPTER 1: INTRODUCTION

1.1 Injectivity Issues of Injection Wells

Fluid injection is widely used for hydrocarbon sweep over a reservoir's life, either after primary depletion or in some cases since the beginning of production, to maintain reservoir pressure. Sometimes, downhole injection is also used as a waste disposal strategy. While injection effectiveness for waste disposal purposes depends almost entirely on the ability to safely inject water at high rates over the life of the project (up to decades), waterflooding requires not only high injection rates but also high sweep efficiencies (Chappell, 2006; Gadde and Sharma, 2001; Munoz et al., 2007), these two variables which have been shown to be dependent on each other are the ultimate optimization goals in EOR injection operations. The problem further expands in offshore facilities where the storing capacities are limited and it becomes critical to maintain the injection rate close to that of produced water with the equipment available on site regardless of whether the injection is for waterflooding or simply waste disposal (Henthorne et al., 2013). Variations of injectivity and sweep efficiency in injector wells could be a quite significant problem that can threaten the viability of some projects or make them underperform their initial estimates. The main causes identified for the loss of injectivity in consolidated formations are: 1) pore plugging due to deposition of solid particles and oil droplets carried by the injected water (Roque et al., 1995; Turekhanov et al., 2007; van Oort, Van Velzen, and Leerlooijer, 1993), 2) thermally induced failure promoted by the temperature difference between injected fluid and the formation (Garon et al., 1988; Lee et al., 2011; Svendson et al., 1991), 3) pressure transients as those caused by quick shutdowns which may cause the formation to mechanically fail (Choi and Huang, 2011; Tang and Ouyang, 2010; Wang et al., 2008) and 4) channelization and liquefaction of poorly consolidated sands.

If the initial injectivity changes because of any or a combination of the above mentioned reasons, an increase in injection pressure and pumping power are required to sustain the injection rate. The increased injection pressure results in stress changes that may initiate fractures or erosion at the wellbore. The grains displacement affects the local hydraulic conductivity and pressure distribution around the wellbore.

During instant shut-in of fluid injection operations, flow back from the formation towards the wellbore may also carry particles back to the well which leads to sand production (Santarelli et al., 2011; Vaziri et al., 2008). Figure 1-1 shows an example of a typical injection rate and bottom-hole pressure history of an injector in the west coast of Africa. In this particular case, the injection pressure shows a linear upwards trend over the 40 month period initiating at around 5,800 psi and finishing at 6.800psi. Initially, the well is flowing at around 18,000BWPD that increases suddenly to almost 50,000BWPD after the well is stimulated. After 40 months though, the well is pretty much flowing at the initial injection rate. This situation evidences the typically critical scenarios that arise in the field which are somehow not well understood.

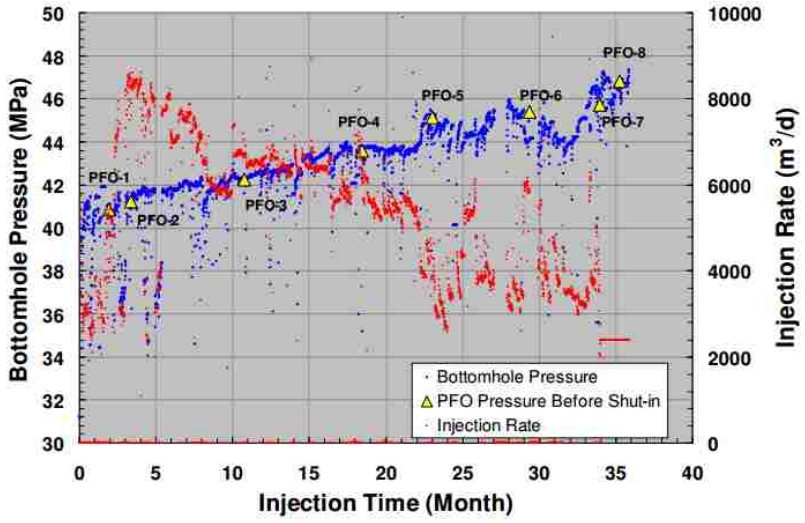

Figure 1-1. Injection history (pressure and flowrate) of a water injector in the west coast of Africa (M Khodaverdian et al., 2010).

Most of the studies consider the growth of fractures as one of the most relevant consequences of formation and/or completions damage in unconsolidated formations; however, the sanding experienced by these wells cannot be explained by fracturing of uncemented rocks. A mechanism that can represent particle detachment from the matrix and fluidization is required to appropriately represent the field observations such as those in Figure 1-1.

When formation damage occurs, fluid flow patterns are expected to vary negatively impacting the efficiency of the waterflooding. Therefore, depending on the induced channel conductivity, injection rate,

degree of consolidation, completion setup, damage on wells and formation properties, the waterfront may take different geometries. The flow geometry could vary from fully dependent on damage pattern to be completely independent of it (Huang, Zhang, Callahan, & Ayoub, 2011). Although experimental lab studies have confirmed the presence of dependent and independent flow patterns, there is a need for numerical models to simulate flow patterns to predict probable issues for injection based on the given fluid and formation properties. The feasibility of waterflooding projects mainly depends on large injection rates with long injectors' life and controllable waterflooding fronts inside the formation to maximize sweep efficiency. A clear understanding of the physics in the vicinity of injectors is crucial to reduce waterflooding costs as well as to increase its efficiency.

1.2 Formation Damage Mechanisms

1.2.1 Thermally driven failure

Thermal induced stresses have received a lot of attention in the literature as they appear to have the most severe effects on altering the formation's closure stress around the wellbore, they are present in almost every underground fluid injection project, if not all, and its effect shows up early in a project's life (Charlez et al., 1996; Svendson et al., 1991). The injection of fluid at low temperatures will increasingly reduce the temperature of the surrounding rock; the rock will contract and develop tensile stresses which are between 10-15psi/°F of cooling (Perkins & Gonzalez, 1982; Clifford et al., 1991; Paige and Murray, 1994; Svendson et al., 1991).

The induced stresses will locally reduce the overall compression ultimately decreasing the fracture gradient. The reduction of compressive stress can be significant since the temperature variations in deep wells can reach 300°F. Such large temperature changes can create fracture gradient reductions of as much as 25% of the initial value. For instance, Garon et al. (1988) reported a fracture gradient decrease from 0.6-0.7 to around 0.5psi/ft after water injection in Prudhoe Bay, Alaska, and argued that the positive effects of higher injection rates were more significant than any negative effect that could arise from the presence of fractures because of the short length (x_f<200ft), they would eventually reach a steady state

where they wouldn't expand further and would remain confined within the reservoir. Similarly, Svendson et al. (1991) argued that an overall change in fracture initiation pressure after primary depletion and cold water injection from 10,500psi to around 8,500psi at the Ula field in the North Sea. Although in most cases, the magnitude of the thermal stress may not be enough to initiate fractures (thermal cracking), an injection pressure designed to be below the fracture gradient may be enough to induce rock failure after it has been "thermally weakened" (Luo and Bryant, 2010; Tovar and Navarro, 2008). Tang and Luo (1998) presented calculations of thermal stress variations in the near wellbore region during mud circulation and showed the importance of accounting these changes in failure analysis and wellbore stability. Svendson et al. (1991) reported wells with injection rates as high as 50,000bbl/d and having almost instantaneous increments in injection rates of up to 6,000bbl/d with little change in injection pressure for the Ula field in the North Sea after cold water injection, the formation had an initial temperature of 295°F with water being injected at around a 100°F. Following their study and other observations, the operator of the field modified its injection process to ensure that the water reaching the wellbore was as cold as possible in order to maximize fracture propagation. The potential for sweep efficiency reduction was not considered in the analysis.

Thermal stresses are mainly generated due to the temperature difference between injected fluid and formation temperature. However, porosity and formation permeability could affect thermal stress distribution around the borehole. Thermal induced fracturing may occur preferably in more permeable regions that allow higher leak-off and hence faster cooling rates (Clifford et al., 1991; Paige and Murray, 1994). When fracture initiates, subsequent injection further cools down the rock in the vicinity of the fracture and promotes fracture propagation. Similarly, fracture height growth will be controlled by the vertical permeability in addition to the stress and mechanical differences between geologic layers, large vertical permeability as proposed by Clifford et al. (1991) (i.e. $k_v/k_h > 0.01$) will allow vertical fracture growth which is an undesired situation as it can create fluid migration to other formations. Thermally induced fractures' orientation and confinement will depend largely but not only on anisotropy and

heterogeneity of the target formation. The availability of information regarding the impact of directional permeability on fracture orientation is limited but could be an interesting subject for further studies.

It is important to note that thermal stresses may also appear as a result of vapor injection which is a common approach for enhanced recovery in heavy oil reservoirs which tend to be poorly consolidated. The formation temperature is increased and the rock expansion generates compressional stresses. In the case of steam injection, severe failures including shear fracturing may take place. Walters et al. (2002) studied the pressure variation of an aquifer almost 1,000ft above the Clearwater formation in Alberta, Canada. The study commenced after the stimulation of the underlying formation through cyclic steam injection generated pressure variations at the aquifer. Because of the distance between the formation and the aquifer, it would be normal to expect the pressure to remain constant unless hydraulic conductivity between the aquifer and the reservoir was established; however, the authors were able to conclude that the poro-thermoelastic effects of the steam cycles were large enough to create the pressure transients in the aquifer. The analysis was performed through the coupling of reservoir and geomechanical models.

1.2.2 Pore plugging mechanism

Fluids injected into a formation usually contain solid particles which properties (size, shape, chemical composition, density and concentration) vary depending on the source. As the injected fluids flow through the formation, the particle content may be retained as a result of either mechanical or chemical interaction of the solids with the formation rock or its fluid. Some of the mechanisms through which particles are deposited include size exclusion, deposition in caverns, chemical precipitation of solutes, formation of a logjam and bridging. Pore size distribution, tortuosity, chemical composition of the rock and fluid's velocity, density and viscosity along with the above mentioned solid particles properties will determine how, when and where the particles come to rest. Furthermore, particles are not only retained within the porous media but also at the formation face, this situation is often described as the external filtration cake. Detailed studies of these phenomena are widely discussed in the literature

(Alkindi et al., 2008; Cheremisinoff, 1998; McCabe et al., 1993; McDowell-Boyer et al., 1986; van Oort et al., 1993; Walsh et al., 1984).

Solids contained by the fluids are not able to travel long distances through the formation and are eventually deposited. When suspended particles in the injected water are retained by the formation in the vicinity of the wellbore, a local decrease in both porosity and permeability occurs due to pore throat occlusion. Such reduction in permeability implies a flow restriction which requires a pressure increment in order to keep the injection rate at the desired level. Eventually, the pressure can reach the formation's closure stress and initiate a fracture. The new void space through which the solids carrying fluid can easily flow enhances injectivity. After continuous fluid injection, the matrix surrounding the fracture is gradually plugged by the particles in the water bringing along with it the necessity of increasing the pumping pressure in order to keep up with the designed flow rate. Again, the pressure may attain the mechanical limits of the rock and the fracture expands (Bachman et al., 2003; Gadde and Sharma, 2001; Saripalli et al., 1999; Slevinsky, 2002). The cycle will repeat as long as the injection process continues. In general, it has been demonstrated that the faster interstitial fluid velocity, the less injectivity detriment caused by particle plugging is observed, this is mainly because particles are able to travel longer distances in the formation before being deposited (Roque et al., 1995; van Oort et al., 1993). As fractures grow, the contact surface for leak-off increases so the fluid velocity decreases with the inevitable consequence that as fractures grow, the formation plugs closer and closer to the fracture surface. Although the area for leak-off is increased, the injectivity could reduce faster than expected (Bachman et al., 2003; Herzig et al., 1970). At a certain point, an external filtration cake may form and restrict flow within the fracture causing a loss of injectivity (Al-Abduwani et al.2005; Shutong and Sharma, 1997), however, the effects of the filtration cake and the appropriate characterization of it has not been achieved as current models are not able to reproduce experimental observations (Turekhanov et al., 2007). Turekhanov et al. (2007) claimed that a transition time (time required for an external filtration to start growing) was not observed on many of its filtration lab experiments as no filter cake was ever formed as predicted by theoretical propositions available in the literature (Wennberg & Sharma, 1997). Many reasons may have led to such results, but a

plausible explanation could lay in the fact that often times the particle size distribution is overlooked in filtration models. Many of the mathematical propositions use a mean particle size rather than including the size range in the filtration models. Ignoring the particle size distribution could lead to unrealistic deposition locations to pressure match field data. Unlike Turekhanov et al., (2007), who used a wide range of particle size distribution in his experiments, it can be seen that many authors assume and use in experiments a single particle size (Al-Abduwani et al.2005; Shutong and Sharma, 1997; Wennberg and Sharma, 1997).

Two opposite situations where particle concentration plays a dominant role are common in the field; the first one could be described as one in which relatively low initial particle or oil concentrations are present and filtration can be used to improve fluid quality and decrease the formation plugging capacity of the fluid (e.g. in EOR processes or disposal of produced water). On the other hand, there are operations in which the solid content is high and the purpose of injection is actually the disposal and storage of the solids in the formation (e.g. the disposal of drill cuttings). As environmental regulations become more stringent, the waste slurry injection becomes more favorable (Dusseault, 2010; McLennan and Abou-Sayed, 2002). In the latter case, the formation storage capacity is the summation of void space generated through injection (fractures, channels and compaction) and available pore. Because the pore size will usually be considerably smaller than the mean particle size, solids will be deposited very close to where they access the formation or at its face hence most of the slurry's solid content will be stored in the voids induced by injection. For disposal purposes, the understanding and development of rock failure becomes important in order to safely store solid wastes (Dusseault, 2010; Guo et al., 2007). For instance, Van den Hoek et al. (1999) provide an example of a successful large untreated waste water injection project in Oman closely monitored by means of simulation, however, the authors fail to clearly identify and outline the keys to success in the project but promote the idea that the solids are being stored almost exclusively in the induced fractures. Svendson et al. (1991) simulated injector's performance at the Ula field including the effect of fracture development and concluded that as fractures grow, the area exposed for leak-off increases up to two orders of magnitude and hence the plugging capacity of fines contained by

the water is reduced. Within this study, measurements of the down-hole concentration of fines showed that water was collecting up to seven times the amount of sediment at the filter's outlet heavily increasing the solid concentration, the situation was attributed to erosion and corrosion of the flow lines between the filter and the formation. As these situations were realized, the fines filters initially in place were bypassed as it was thought that the effect of particle concentration in the injected water was not significant and even if it was, the surface filtration was not being an effective control method. Similar observations led to bypassing filtering equipment at the Forties Charlie, Gyda, and Magnus fields (Paige and Murray, 1994). It is important to highlight that these conclusions were made after 4 years of successful water injection at Forties Charlie without treating the water. In the field examples described in the preceding lines, the injecting performance was only concerned with the achievable injection rate and pressure while the sweep efficiency on EOR either received little or no attention or was not a concern because the project was for produced water disposal; also, the possibility of out of zone injection was not considered either evidencing a lack of awareness. A recent case of the impact of oil and fines concentration on injectivity is reported by Souilah et al. (2014) for an offshore Angola project. Initially, filtered seawater is injected in various wells located in different fields followed by the injection of a mixture of seawater and treated produced brine. The produced brine that has oil and a considerably higher concentration of suspended solids in comparison to the seawater even after processing (filtration) generates a dramatic decline in injectivity. When the produced brine is eliminated from the mixture, the wells recover and even surpass the initial injectivity. In these fields, the operator does consider the fracture pressure of the overlying cap rock and sets it as the limit for bottomhole pressure. By performing coupled simulations of reservoir flow and geomechanical models, Souilah et al. (2014) claimed that they were able to match the injectivity decline and restoration observed. When multiple fluid sources are available, the need for multiple filtration systems arises as filters are usually designed to treat specific crude water. The necessity of more than one filtration system implies higher equipment costs and requires extra space that may not be available in offshore facilities (Pedenaud, 2014).

Cyclic injection of solid waste has also been practiced specially for drilling and fracturing fluids, Guo et al. (2007) reported the results of cyclic drill cuttings injection on the North Slope of Alaska where the cuttings are grinded, water is added and the resulting slurry is injected into a soft sandstone formation at rates of up to 30,000bbl/d. To understand the process through which the cuttings are being placed and in order to assess the safe disposal of the material, well testing, logging and simulations were performed. The study of well testing data pointed out that the wastes injected are stored in multiple induced fractures that may close during shut-in periods of the process; when injection resumes, fractures can be re-opened. The results also indicated that fracture heights created in such wells are slightly below 2000ft. It could be thought that the drilling cuttings act as proppants that prevent the fracture from closing just as in hydraulic fracturing, however, the elasticity and the healing properties of the soft formation may be the cause for such an unexpected behavior. A similar situation was described by Chin and Montgomery (2004) that extended a fracturing model for solid material injection into soft formations basically by accounting for rock compaction. According to the author, the model results can be used to obtain maximum injected volume per well, area of influence, bottomhole pressure and provide insights into the vertical containment of injected material. The author concludes that up to 25MMbbl of slurry can be injected through a single well in such cases which is more or less in line with what had been injected in the project described by Guo et al. (2007). Rather than being a fixed number, the formation storage capacity per well should depend on formation and injection process properties.

1.2.3 Geomechanical effects of injection into unconsolidated formations

Recently, geomechanics of injection in unconsolidated formations has caught the attention of the industry as the formation's response has proven to be extremely unpredictable.

An interesting case in the Kikeh field offshore Malaysia is presented by Webb et al. (2009) where low injectivity was observed from the early development phase of the project. In an attempt to reach the design injection rates, fluid was pumped above the closure pressure in order to fracture the formation, instead of obtaining the expected pressure drop from fracture initiation, the pressure just kept increasing

and the injection rate had to be decreased to operate within safe limits. The situation was attributed to the stress increment due to the raise in pore pressure. In general, increments in pore pressure increase the total stress but it is not as significant as the stress reduction caused by temperature difference between the fluid and the formation. Unfortunately, data related to thermal stress is not provided constraining the possibility to perform a complete analysis. The solution was found in initiating a fracture with a high viscosity fluid. The results of the treatment were successful from the injectivity perspective and the injectors' performance after two years was still satisfactory. A similar situation was reported by Pedroso et al. (2009) in the Campos Basin offshore Brazil. In this case, attempts to propagate a fracture were unsuccessful and a critical situation was reached when the fracture gradient rose from 0.52 to 0.83 psi/ft. In the case of unconsolidated formations, the increment in pore pressure caused by fluid injection increases the total stress. Usually, the thermal effect previously described would overcome the pore pressure variation, however; the lower matrix stiffness of this type of formations make the thermal stress variation less significant (Souilah et al., 2014). Due to the high leak-off, as the pressure rises in the formation rock so does the resistance to fracturing.

Frac-Packs are being used increasingly in poorly consolidated formations to control sand production and maintain high injectivity at injectors. The imposed fractures might be beneficial in increasing injectivity. However, if fractures propagate the formation may absorb the gravel filling the fractures. Soon after, in the absence of the frac-pack, the soft formation tends to close the fracture in the vicinity of the wellbore (this situation is graphically described in Figure 1-2). The mechanism through which formation sand is brought back close to the wellbore is described in a later section.

Norman and McCarty (2006) documented an operational case of frac-packs used as a mechanism to minimize well intervention off the coast in West Africa. The target formation consists of unconsolidated sand with large particle size distribution requiring injection rates of 35,000BWPD. The frac-pack showed the ability to control problems associated to the water hammer caused by often shut-ins. The costs associated to the frac-pack were lower than the expected expenses for well intervention making this type of completions economically favorable.

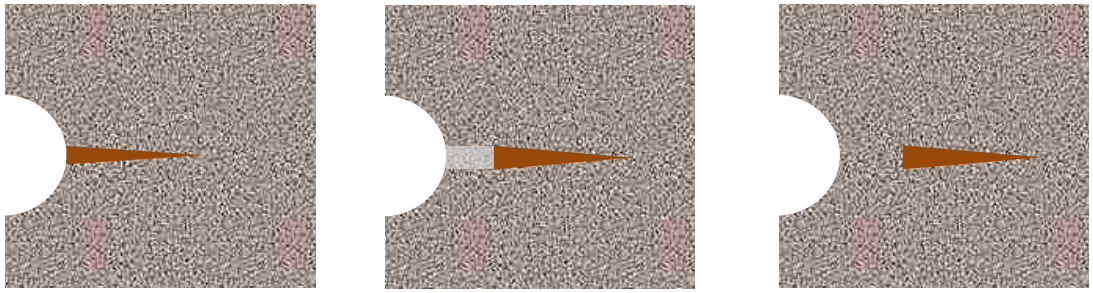

Figure 1-2. Lost frac-pack due to fluid injection. A) The frac-pack is placed at the perforations, B) the initial fracture resumes growth as fluid is injected and the proppant progresses into the formation. C) The high permeability channel between the proppant and the well is filled back with formation sand during shut-in periods**.**

Most of the studies consider the growth of fractures as one of the most relevant consequences of formation and/or completions damage on unconsolidated formations; however, the sanding experienced by these wells cannot be explained by fracturing specially fracturing an uncemented rock. A mechanism that can represent particle detachment from the matrix and fluidization is required to appropriately represent the field observations. When a significant amount of particles is taken away from a specific volume, a high porosity channel is created, the channel may have similar properties to fractures but it should not be muddled with them because the mechanisms and hence its geometric features vary significantly. Huang et al. (2011) performed a series of experiments in which glycerin and polyacrylamide are pumped into a sand pack. The results suggested that the sand can behave either like solid rock (as in fracturing) or like a liquid (as in fluidization), based on its observations the author stated that there must be a transition point between the two behaviors dictated by fluid properties and injection conditions. Similarly, Mahadevan et al. (2012) performed a similar experiment on a Hele-Shaw cell containing spherical gravel not only observing the formation of channels as a consequence of grain displacement but also the dependence of the channels' pattern on porosity heterogeneity. A set of experiments performed at the LSU's Petroleum Geomechanics and Applications Consortium (PGRAC) demonstrating the behavior of porosity changes due to fluid injections is shown in Figure 1-3. It can be observed that high porosity channels are created as a result of fluid injection which unlike hydraulic fracturing, is caused from individual grain displacement.

Figure 1-3. Two dimensional experiments on fluid injection into unconsolidated porous media. A (μ=20cP and 30ml/min), B (μ=20cP and 90ml/min) and C (Water into oil saturated sand, 90ml/min)

Experimental work in three dimensions has also been performed in order to elucidate better the effects of fluid injection into poorly consolidated sand (Hosseini, 2012). In these, a particular set of results is of special interest to this research, these are results for which the author claims that fluid induced formation failure was in shear mode which yields the tubular channels and pressure readings in Figure 1-4. Similar results have also been reported by Golovin, et al. (2011) and Germanovich et al., (2012).

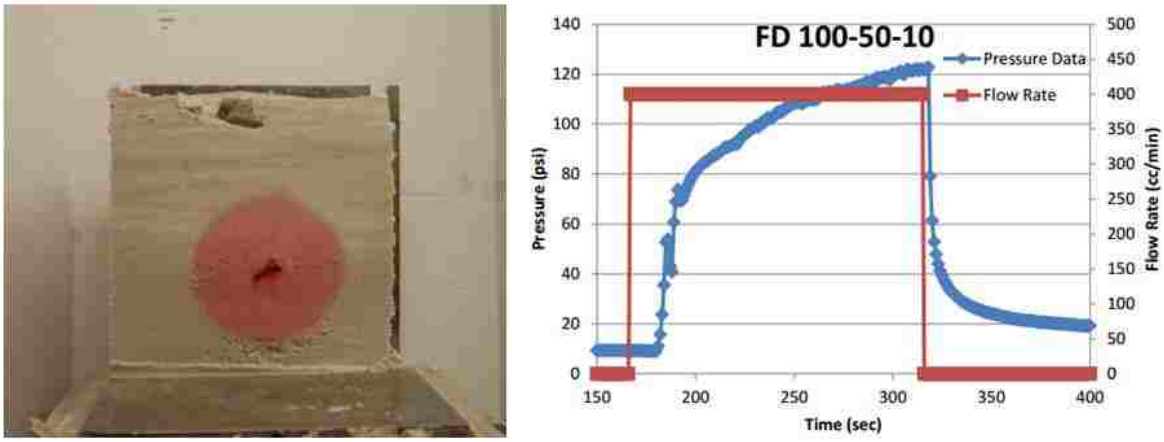

Figure 1-4. Experimental shear failure of unconsolidated sands due to fluid injection, channel extension (left) and resulting pressure readings (right). (Hosseini, 2012)

Based off of the experimental results, Mahadevan et al. (2012) proposed a relatively simple model based on the material balance that showed good agreement with the experimental observations. Using the same mass balance as Mahadevan et al. (2012), Ameen and Dahi Taleghani (2014) extended the model for a wellbore geometry and simulated the effects of water injection. Figure 1-5 has an example of the high permeability channels developed due to solid transport within the formation and the pressure profile

obtained from the author's results. A pressure profile as the one observed sheds light on how, unlike fractures, the flooding geometry has no symmetry with respect to any axis.

Theoretical propositions regarding the presence of erosion and channelization have been explored mostly to replicate the laboratory scale (short time and confined space) observations made through some experiments, however, expanding the models available to consider the effects of thermal stresses and hysteresis have not been studied and the point at which the failure mechanism goes from fracture type behavior to erosional channelization is not well understood. The theoretical models could also be extended to different types of completion systems, formations and fluids, comparison of theoretical results to field observations could promote the use of it as an effective well design tool.

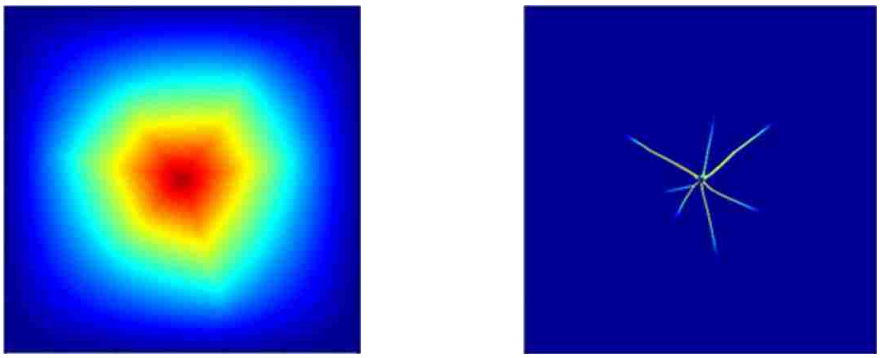

A B

Figure 1-5. A) Pressure contour after high permeability channels develop as a consequence of solid transport (Channelization). B) Fluid injection induced channels. (Ameen & Dahi Taleghani, 2015)

Unconsolidated formations can also fail due to liquefaction; this is outlined and described for oil producing wells by Sumer et al. (2006). The authors state that under the effect of waves, a formation's pore pressure increases and if it reaches the overburden, the sand can liquefy (sand behaves like a liquid). This phenomenon in water injectors is essentially attached to water hammer effects discussed in the next section.

1.2.4 Water hammer Effect

The water hammer effect is essentially fluctuating pressure surges that are generated when a sudden change in flow rate occurs due to a sudden valve closure or pump shutdown (Afshar and Rohani, 2008).

In water injection wells, this phenomenon appears during maintenance or emergency shut downs which can occur as much as 80 times per year (Norman and McCarty, 2006). The pressure transient travels down the wellbore, is reflected back and induces a series of pressure pulses over the system, this pulses can be of up to thousands of psi in magnitude and may cause damage to the wellbore completions as well as the formation (Choi and Huang, 2011). In general, damage to completions and formation is avoided during water hammer through proper shut-in control and implementation of check valves (Norman and McCarty, 2006; Vaziri et al., 2008). This phenomenon mainly affects unconsolidated formations which are believed to be more prone to fail because of a pressure gradient rather than a stress itself. The wellbore pressure behavior after a sudden well shut-in is shown in Figure 1-6. It can be seen that the initial pressure drop is fast until it reaches reservoir pressure followed by pressure pulses that attenuate over a short period of time. These pressure oscillations create flow-back into the wellbore making it possible for the formation sand to reach the wellbore and its surroundings. If that situation arises then loss of injectivity can be expected.

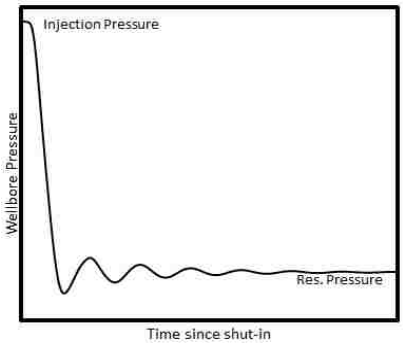

Figure 1-6. Wellbore shut-in pressure response, these pressure fluctuations may cause flowback to the wellbore.

Multiple solutions for the water hammer using numerical methods have been proposed (Afshar and Rohani, 2008; Greyvenstein, 2002; Larock, Jeppson, and Watters, 1999; Wylie, Streeter, and Suo, 1993), some of them have proven to provide relatively accurate results when compared to real data (Choi and Huang, 2011; Mondal, 2011; X. Wang et al., 2008). However, the proper coupling and solution of a model including water hammer, reservoir and geomechanical aspects has not been achieved yet. Tang and Ouyang (2010) performed a study on the water hammer effect on offshore wells using commercial

multiphase fluid flow software. Based on their results, the authors argued that the water hammer effect in a injector well is not as strong as that experienced in a closed pipeline because the reservoir absorbs part of the energy in the pressure wave, nevertheless, as the skin factor of the near wellbore region is increased the situation resembles more to that of a closed pipeline and the pressure variation may increase and be of up to thousands of psi. The use of commercial software that does not really utilizes a transient reservoir model does not accurately represent the situation, a fully coupled well-reservoir model is required to perform water hammer calculations, furthermore, the geomechanical effect should also be incorporated. A similar research using commercial software was performed by Choi and Huang (2011). Hu et al. (2007) generated a method to couple the transient reservoir and wellbore models but did not incorporate the associated geomechanical effect. Han et al. (2003) gave a semi-analytical solution to the problem incorporating a well and formation fluid flow model and the geomechanical effect but had to restrict their solution to no flow from the reservoir to the wellbore and no pore pressure variations inside the formation, restrictions that again lead to unrealistic results.

The water hammer pressure pulses can weaken the forces holding sand particles together and eventually lead to complete particle detachment which will be observed as sand production. Vaziri et al. (2008) observed that in soft rocks, water hammer is the main cause for sanding but outlined that even in the presence of water hammer, sanding in unconsolidated formations will not appear for several years as long as the pressure pulses remain below 200psi. In a separate study, Wang et al. (2008) intentionally induced pressure transients in order to compare simulation results with real well data. The induced pressure pulses of up to 200psi did not cause damage to any of the well components or the formation, however, this does not mean that pressure pulses of up to 200psi will never generate damage and it seems rather arbitrary to assure that when no fluid, completions or formation properties are accounted in the analysis. In order to develop criteria to assess whether pressure transients will damage either the completions or the formation requires a proper mechanical analysis of the formation and in-situ stresses. Furthermore, sanding has been widely attributed to pressure transients; however, this could be a partially erroneous conclusion. Sanding is observed during shut-in because it is one of the few circumstances

during regular operations in which there is flow-back from the reservoir into the wellbore, this fact does not imply that the particles are being detached from the rock matrix during stable injection.

1.3 Asymmetric Areal Sweep

Fluid and formation properties have always been related to sweep efficiency while the associated geomechanical phenomena had been overlooked until recent times. Nowadays, many effects on sweep efficiency that are related to geomechanical aspects are widely recognized and some of them have been addressed. This section provides a review of some of the reported aspects and how they can affect the performance of secondary recovery processes. Although some consequences of geomechanical associated problems might be reversible, properly managing the water injection program from the beginning of the project is key to obtain better results in waterflooding (Silin and Patzek, 2001).

A compelling study on the impact of fractures at fluid injectors on sweep efficiency was presented by Gadde and Sharma (2001), the results obtained suggest that: 1) The oil recovery may increase until a certain fracture length after which the recovery is less than that of the unfractured formation; 2) Larger spacing between injectors and producers reduce recovery due to the inherent heterogeneity of formation properties; 3) Areal sweep may increase if fractures in a five spot pattern align right in between the producers. In general and regardless of the well pattern, fractures growing in the direction of producers are likely to provide a direct path for the injected fluid and faster breakthrough to producers as depicted in Figure 1-7; and 4) Horizontal formation heterogeneities negatively impact the oil recovery in the presence of fractures. In this last conclusion however there was no acknowledgement to the fact that fractures may extended differentially in horizontal layers of dissimilar properties (Figure 1-8).

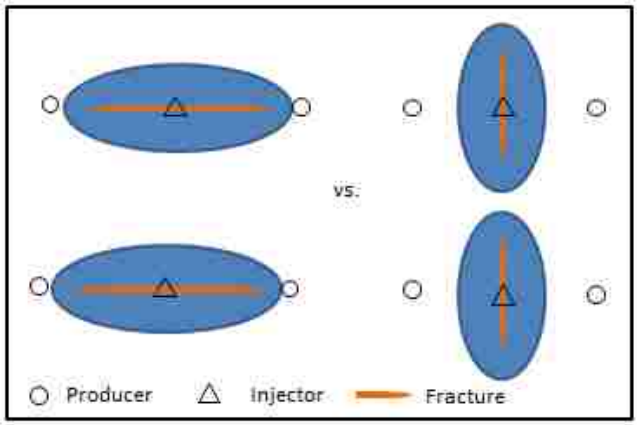

Figure 1-7. Possible flooding patterns for fracture azimuth towards producers (Left) and away from producers (Right). The situation on the left hand side might cause an early water breakthrough due to the higher hydraulic conductivity from fractures in the producer's direction.

Even if the total oil recovered by the water flooding process remains unchanged, at least the required injection time and pore volumes could increase for a specific recovery goal which implies additional costs. Wright et al. (1995) observed for a specific diatomite reservoir that the stress changes undergone in the formations during either injection or production can be severe enough to alter the direction of the minimum stress. Such changes can cause the fractures to reorient after initiation (Perkins and Gonzalez, 1982). In horizontal injectors the problem further expands as several fractures can be created throughout the injection interval. In order to appropriately model this scenario, it is important to acknowledge the variations of bottom hole pressure, flow rate and temperature throughout the perforated interval and its relation to the fractures developed as outlined by Stevens et al. (2000). Hustedt et al. (2008) used a coupled reservoir-fracture model and demonstrated that the effect of fractures on recovery for five spot patterns efficiencies can be either positive or negative and that the careful handling of the water injection processes can definitely yield better recovery factors.

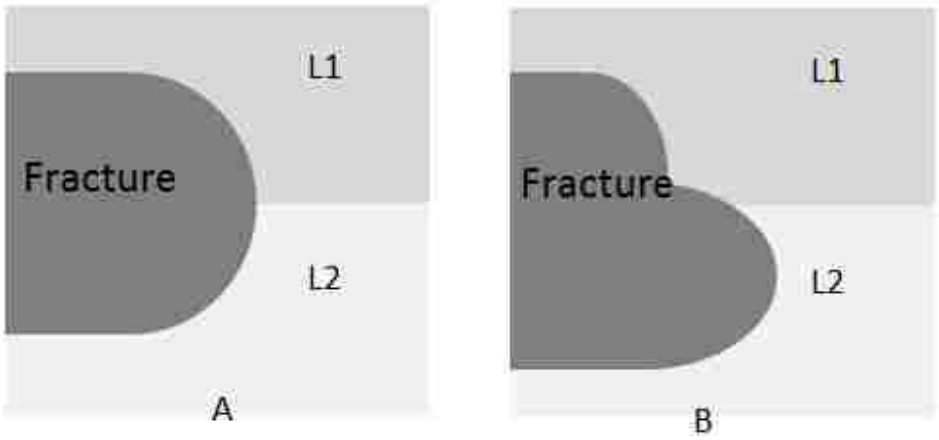

Figure 1-8. Fracture growth across heterogeneous formations. A) Fracture extension equal across layers, B) Fracture length variation across layers of dissimilar properties.

Since little or no control can be exerted over some of the effects of fluid injection, well patterns and their orientation with respect to preferred fracture orientation, inter-well distance, completions systems, well position with respect to formation boundaries and injection temperature and rate will be among the control mechanisms available to avoid the undesired effects of induced fractures in injection wells (Clifford et al., 1991; Dahm, et al. 1998; Gadde and Sharma, 2001a; Svendson et al., 1991).

1.4 Polymer Flooding Considerations

Polymer flooding has been identified as an effective EOR technique to improve the sweep efficiency by increasing the fluids mobility ratio (Delshad et al., 2008; Wang et al., 2007). Shear thinning polymers are used in polymer flooding to lower viscous dissipation, this implies that in the regions with higher permeability the sweeping is not necessarily as good as in regions with lower permeability, consequently it leads to an uneven hydrocarbon sweep (Delshad et al., 2008). Furthermore, some polymers may behave as a shear thickening fluid when flowing through porous media at high velocities (Delshad et al., 2008). Other factors that can affect the polymer's viscosity are the salinity of the formation and/or water used for dilution and polymers' molecular weight and concentration (Wang et al., 2007). In general, the complex polymer rheology may reduce injectivity which requires higher pumping pressures that can result in the initiation of fractures (K. Lee et al., 2011).

One of the most widely studied and well documented cases of polymer injection is the Daqing oil field in China, its fame is owed to the fact that more than 300,000 bbl/d of oil were produced driven by polyacrylamide flooding (Wang et al., 2004). Wang et al. (2004) reported a particular occurrence in the field; in an attempt to improve the field performance, more than 40 injection wells were hydraulically fractured but after only three months of injection, performance of fractured wells had dropped significantly. The operator realized that the fractures were gone as the proppant was taken away from the near wellbore region allowing the fractures to close back on their walls. The main reason identified for the mentioned situation was that particle plugging was increasing the bottom-hole pressure which at the end resulted in further fracture propagation. Since the polymer usually has a high carrying capacity due to its viscosity, proppants are carried away. In order to control this situation, resin coated sand proppants have been used. By using these proppants the fractures' life went from 3 months to 30 months. The reason why resin coated proppants are not carried away is probably because of the cohesive forces that the resin puts between individual sand grains thus making it more difficult to carry away as the particles would have to be carried in bulk and not individually. Another solution to address this problem is utilizing heavier proppants, this may keep the proppants in place even when fractures are further expanded.

Khodaverdian et al. (2009) provided an analysis of polymer injection in unconsolidated formations. Through experiments and simulation, the authors concluded that i) Fractures propagate at low net pressures (150-300psi), ii) there were difficulties to reproduce (through modelling and simulation) the complex fracture geometries that arise from polymer injection in unconsolidated sands as observed in their experiments and in line with Huang et al. (2011) observations, and iii) that the vertical confinement of fractures might be lost due to the excessive pressure buildup near the wellbore.

In general, the concerns with polymer injection include the thermal and particle concentration effects mentioned in the previous sections. The complicated polymer rheology, its evolution over time and response to reservoir conditions add to its complexity. Although injectivity during polymer flooding is highly dependent on the injection rate, wells undergoing polymer flooding are less susceptible to sand production. This issue could arise from the fact the higher viscosities decrease the intensity and

magnitude of the water hammer effect hence diminishing the well flow-back during shut-in periods, however, higher viscosity fluids may increase channelization during injection.

1.5 Research Objectives

Given all the scenarios mentioned in the previous sections, this research shall cover the following:

1.5.1 Channelization in two dimensions

Implementation in two dimensions of the channelization model as proposed by Mahadevan et al. (2012) and also implemented by Ameen and Dahi Taleghani (2014). This considers fully dynamic fluid flow through porous as the underlying physical behavior unlike previous authors mentioned.

1.5.2 Computational model calibration

Calibration of the two dimensional channelization model with the experiments performed at the Geomechanics lab. The experiments vary formation particle size distribution, fluid viscosity and injection rate that provide a study on the impact of relevant parameters.

1.5.3 Dynamic wellbore and reservoir modelling coupling

Coupling of a fully transient, single phase fluid flow in pipes (wells) model to the channelization model. This will allow the computation of sand production at injectors during shut-in. The transient flow in pipes model recreates the water hammer effect observed in wells when valves at the surface are closed.

1.5.4 Channelization in three dimensions

Implementation of the channelization model in three dimensions so that an accurate geometrical representation of the completions systems is achieved. This allows the use of horizontally varying formation parameters which represent multilayered systems. A more accurate visualization of injected fluid flow patterns in the reservoir would be achievable.

1.5.5 Field test design for parameter calibration

Design of a workflow that allows the model parameters calibration through field data (i.e. designing a test like injection test to derive model parameters).

CHAPTER 2: NUMERICAL MODEL

2.1 Dynamic Fluid Flow in Porous Media

2.1.1 Diffusivity equation

The basis for most of the models that try to capture the injected fluid-formation interaction in poorly consolidated formations rely on the pressure gradient (Dancey et al., 2002). As stated by Darcy's law for fluid flow in porous media, the pressure gradient is a function of the hydraulic conductivity and the flux as $q = -D\nabla P$ $(D = k/\mu)$. In other words, the drag force that a fluid in motion can exert over the rock it is flowing through depends on the fluid interstitial velocity and the resistance that the rock imposes to the fluid motion. Now the pressure gradient cannot be obtained explicitly from Darcy's law as the time varying rock properties make of this a dynamic problem. For this purpose, we shall begin by stating the diffusivity equation that can capture this non-steady state behavior as,

$$\phi \rho c_t \frac{\partial P}{\partial t} = \nabla \cdot \left(\frac{\rho}{\mu} \boldsymbol{k} (\nabla P - \rho g \nabla z) \right) \qquad \text{Eq.2-1}$$

In this equation, ϕ is the porosity, ρ and μ are the fluid density and viscosity respectively and c_t is the total compressibility which is the sum of the product of all the fluids present compressibilities and saturations plus the formation's rock compressibility $(c_t = \sum c_i s_i + c_f)$. Also, $\boldsymbol{k}$ is the formation's absolute permeability tensor, g is the gravity acceleration and z is the elevation with respect to a reference point or depth. Now, because this study deals with time changing formation porosity, it is important to make the permeability dependent on it so that it can be updated at every timestep. This is performed through the Carman-Kozeny relationship:

$$k = \frac{\psi^2 l_g^2 \phi^3}{A(1-\phi)^2}, \qquad \text{Eq.2-2}$$

here, the permeability is a nonlinear function of the porosity, the mean grain size (l_g), the sphericity of the sand particles (ψ) and *A*, a dimensionless variable dependent on the tortuosity and the sphericity that can vary between 80 and 320 (Åströmet al. 1992; Skartsis et al. 1992), the parameter can be calculated as:

$$A = S\left(\frac{L_e}{L}\right)^2, \qquad \text{Eq.2-3}$$

in which L_e is the effective streamline, L is the system length and S is the pore shape factor. Typically, A has a value of 180.

2.1.2 Two dimensions finite element implementation of the diffusivity equation boundary value problem

From the main equation (Eq.2-1), it can be said that for a two dimensional system and assuming that horizontally the fluid has a constant density and viscosity, the diffusivity equation becomes:

$$\phi \mu c_t \frac{\partial P}{\partial t} = \nabla \cdot (\boldsymbol{k} \nabla P). \quad \text{Eq.2-4}$$

With the term on the right hand side as,

$$\nabla \cdot (\boldsymbol{k} \nabla P) = \frac{\partial}{\partial x}\left(\frac{k_x}{\mu}\frac{\partial P}{\partial x}\right) + \frac{\partial}{\partial y}\left(\frac{k_y}{\mu}\frac{\partial P}{\partial y}\right). \quad \text{Eq.2-5}$$

The system then requires an initial condition, namely a known solution for time $t = 0$ as well as Dirichlet and Neumann type boundary conditions. It is assumed that before injection begins the reservoir is at rest hence the pressure throughout should be the same at every point. For a typical offshore Gulf of Mexico formation from the Pleistocene usually found at around 5,300ft of depth we can safely assume an initial formation pressure of 2,800psi which implies that:

$$P(t = 0) = 2{,}800psi \; \forall \; (x, y). \quad \text{Eq.2-6}$$

The Dirichlet boundary condition to be used is that of a constant reservoir pressure at the system's external boundary:

$$P(x, y) = 2{,}800psi \; \forall \; (x, y) \text{ on the Dirichlet Boundary } (r = r_{formation}) \quad \text{Eq.2-7}$$

At the wells, or in this case the Neumann boundaries where fluid is injected the pressure gradient is proportional to the flow rate to area open to flow ratio as:

$$\frac{\bar{Q}}{A} = \left(D_x \frac{\partial P}{\partial x} + D_y \frac{\partial P}{\partial y}\right) \rightarrow D_* = \frac{k_*}{\mu} \quad \text{Eq.2-8}$$

Note that these equations do not pose any geometry restrictions which allow computing different reservoir geometries if required. The number of Neumann boundaries is not restrained either and multiple wells can be used if desired. An injector could actually be turned into a producer by simply having $\bar{Q} = -\bar{Q}$ which all together makes the possible solutions and cases to be represented very versatile.

The diffusivity equation (Eq.2-4) and boundary conditions (Eq.2-6-Eq.2-8) are solved using numerical finite element methods. On their stead state implementation, Mahadevan et al. (2012) and Rostami and Dahi (2014) solved a similar problem using the finite volume method. The first was recreating an experimental setup in a squared hele-shaw cell with fluid injection on one of the cell sides which allowed for the finite volume variable discretization in a perfect squared grid, on the other hand, Rostami and Dahi Taleghani (2014) fluid injection takes place at a round wellbore in the middle of the system domain, this led to geometry handling difficulties which required the inclusion of ghost nodes at the wellbore. In order to overcome this issue and in an attempt to decrease the computational cost of the simulation, a Finite Element Method (FEM) is chosen.

First the weak formulation of the problem with boundary conditions has to be stated. To do this, the PDE is multiplied by an arbitrary weighting function δP and integrated over the domain, Ω:

$$\int_{\Omega} \left(\phi \mu c_t \frac{\partial P}{\partial t} \delta P\right) d\Omega = \int_{\Omega} \left(\frac{\partial}{\partial x}\left(k_x \frac{\partial P}{\partial x}\right) + \frac{\partial}{\partial y}\left(k_y \frac{\partial P}{\partial y}\right)\right) \delta P d\Omega \;\; \delta P \; \forall \, (x, y), \qquad \text{Eq.2-9}$$

when integrated by parts $\left(\int u \cdot dv = u \cdot v - \int v \cdot du\right)$, with $dv = \frac{\partial}{\partial *}\left(D_* \frac{\partial P}{\partial *}\right)$ and $u = \delta P$, the static term on the right hand side becomes:

$$\int_{\Omega} \left(\frac{\partial}{\partial x}\left(k_x \frac{\partial P}{\partial x} \delta P\right) + \frac{\partial}{\partial y}\left(k_y \frac{\partial P}{\partial y} \delta P\right)\right) d\Omega - \int_{\Omega} \left(\frac{\partial \delta P}{\partial x} k_x \frac{\partial P}{\partial x} + \frac{\partial \delta P}{\partial y} k_y \frac{\partial P}{\partial y}\right) d\Omega \,. \qquad \text{Eq.2-10}$$

Applying the Gauss theorem ($\int_V \; (\nabla \cdot F) dV = \int_{\partial V} F \cdot dS$) to the first term yields the following:

$$\int_{\partial\Omega} \left(k_x \frac{\partial P}{\partial x} + k_y \frac{\partial P}{\partial y}\right) \delta P dS - \int_{\Omega} \left(\frac{\partial \delta P}{\partial x} k_x \frac{\partial P}{\partial x} + \frac{\partial \delta P}{\partial y} k_y \frac{\partial P}{\partial y}\right) d\Omega \qquad \text{Eq.2-11}$$

For all elements e in the domain in which the problem is to be solved and satisfying the Neumann type boundary conditions in Eq.2-8 makes Eq.2-9:

$$\sum_{e}\left(\int_{\partial\Omega e}\frac{\overline{Q}}{A}\delta P dS-\int_{\Omega e}\left(\frac{\partial\delta P}{\partial x}k_x\frac{\partial P}{\partial x}+\frac{\partial\delta P}{\partial y}k_y\frac{\partial P}{\partial y}\right)d\Omega=\int_{\Omega e}\left(\phi\mu c_t\frac{\partial P}{\partial t}\delta P\right)d\Omega\right) \quad \text{Eq.2-12}$$

The solution to this system for linear triangular elements as that on the left of Figure 2-1, consisting of three nodes one on each vertex is here presented. Only the solution for linear triangular elements will be introduced, it would be redundant to do so for different types of elements, however, the code has been implemented for both linear and quadratic triangular elements.

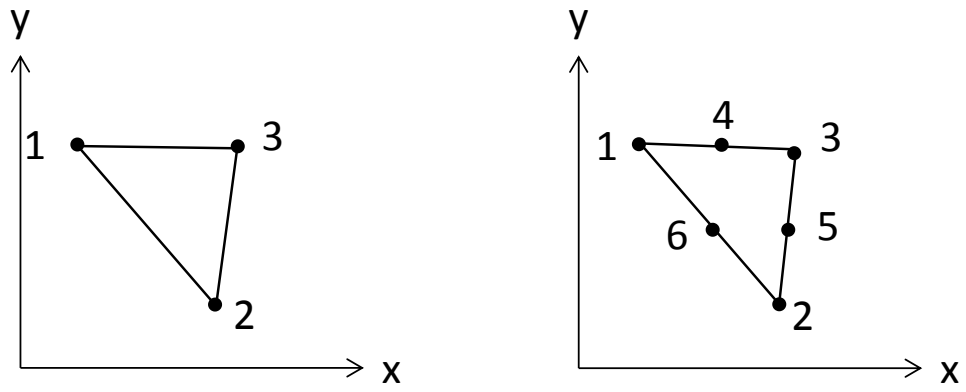

Figure 2-1. Linear (left) and quadratic (right) triangular elements.

The function that interpolates the solution between the discretized points (nodes) on the system known as shape function (N) can be obtained beginning from Eq.2-13.

$$P(x,y)=a_i+a_{ii}x+a_{iii}y \quad \text{Eq.2-13}$$

For an entire element this corresponds to:

$$\begin{Bmatrix}P_1\\P_2\\P_3\end{Bmatrix}=\begin{bmatrix}1&x_1&y_1\\1&x_2&y_2\\1&x_3&y_3\end{bmatrix}\begin{Bmatrix}a_i\\a_{ii}\\a_{iii}\end{Bmatrix}, \quad \text{Eq.2-14}$$

which becomes

$$P(x,y)=\begin{bmatrix}1&x&y\end{bmatrix}\begin{bmatrix}1&x_1&y_1\\1&x_2&y_2\\1&x_3&y_3\end{bmatrix}^{-1}\begin{Bmatrix}P_1\\P_2\\P_3\end{Bmatrix}=\begin{bmatrix}N_1&N_2&N_3\end{bmatrix}\begin{Bmatrix}P_1\\P_2\\P_3\end{Bmatrix} \quad \text{Eq.2-15}$$

In Eq.2-15, $N_i(x,y)$ are the shape functions corresponding to node i of the system. In order to simplify the system of equations that arises from the shape functions and to allow the easy computation of the integrals required to solve the diffusivity equation, the shape functions and geometrical representation of the system is translated into the isoparametric system in this case represented by ξ and η.

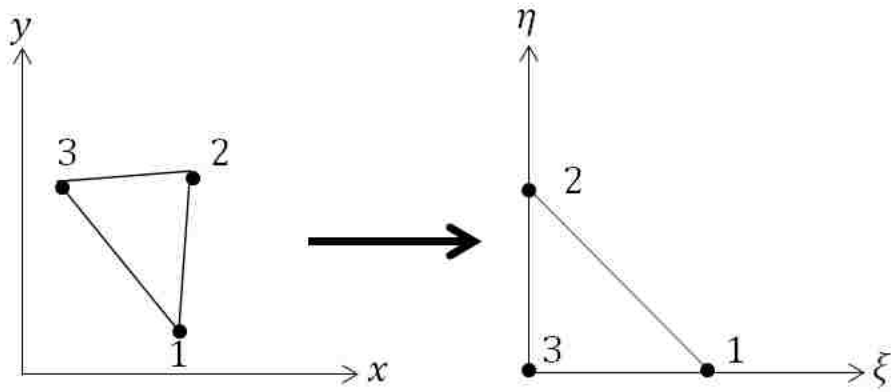

Figure 2-2. Linear triangular element on Cartesian coordinates (left) and isoparametric coordinates (right).

Then for each node i,

$$N_1(\xi,\eta) = \xi, \qquad N_2(\xi,\eta) = \eta, \qquad N_3(\xi,\eta) = 1 - \eta - \xi \qquad \text{Eq.2-16}$$

From Eq.2-14 and the new defined system of coordinates the variable of interest, in this case the system's pressure within an element becomes:

$$P = \sum_{i=1}^{3} P_i N_i(\xi,\eta), x = \sum_{i=1}^{3} x_i N_i(\xi,\eta) \text{ and } y = \sum_{i=1}^{3} y_i N_i(\xi,\eta) \qquad \text{Eq.2-17}$$

Now the goal is to obtain the differential terms in the underlying Eq.2-12, in order to do so, we shall differentiate the previous result:

$$\frac{\partial P}{\partial \xi} = \left(\sum_{i=1}^{3} P_i \frac{\partial N_i}{\partial \xi} \right) \text{ and } \frac{\partial P}{\partial \eta} = \left(\sum_{i=1}^{3} P_i \frac{\partial N_i}{\partial \eta} \right) \qquad \text{Eq.2-18}$$

and thus:

$$\begin{Bmatrix} \frac{\partial P}{\partial \xi} \\ \frac{\partial P}{\partial \eta} \end{Bmatrix} = \begin{bmatrix} \frac{\partial N_1}{\partial \xi} & \frac{\partial N_2}{\partial \xi} & \frac{\partial N_3}{\partial \xi} \\ \frac{\partial N_1}{\partial \eta} & \frac{\partial N_2}{\partial \eta} & \frac{\partial N_3}{\partial \eta} \end{bmatrix} \begin{Bmatrix} P_1 \\ P_2 \\ P_3 \end{Bmatrix} \qquad \text{Eq.2-19}$$

Using the Chain rule for differentiation as:

$$\frac{\partial u}{\partial x}=\frac{\partial u}{\partial \xi}\frac{\partial \xi}{\partial x}+\frac{\partial u}{\partial \eta}\frac{\partial \eta}{\partial x}\rightarrow\begin{Bmatrix}\frac{\partial P}{\partial x}\\ \frac{\partial P}{\partial y}\end{Bmatrix}=\begin{bmatrix}\frac{\partial \xi}{\partial x} & \frac{\partial \eta}{\partial x}\\ \frac{\partial \xi}{\partial y} & \frac{\partial \xi}{\partial y}\end{bmatrix}\begin{Bmatrix}\frac{\partial P}{\partial \xi}\\ \frac{\partial P}{\partial \eta}\end{Bmatrix} \quad \text{Eq.2-20}$$

Similarly, using the procedure that led to the results in Eq.2-18 provides the matrix containing the partial derivatives of the isoparametric coordinates with respect to those in Cartesian coordinates i.e.,

$$\begin{bmatrix}\frac{\partial \xi}{\partial x} & \frac{\partial \eta}{\partial x}\\ \frac{\partial \xi}{\partial y} & \frac{\partial \xi}{\partial y}\end{bmatrix}=\begin{bmatrix}\sum_{i=1}^{3} x_i\frac{\partial N_i(\xi,\eta)}{\partial \xi} & \sum_{i=1}^{3} x_i\frac{\partial N_i(\xi,\eta)}{\partial \eta}\\ \sum_{i=1}^{3} y_i\frac{\partial N_i(\xi,\eta)}{\partial \xi} & \sum_{i=1}^{3} y_i\frac{\partial N_i(\xi,\eta)}{\partial \eta}\end{bmatrix}^{-T}. \quad \text{Eq.2-21}$$

Since the weighting function can be arbitrary, a similar functionality to that given to the variable of interest is given to it ($\delta P=\sum_{i=1}^{3}\delta P_i N_i{}'(\xi,\eta)$), then if we define:

$$\begin{Bmatrix}\frac{\partial P}{\partial x}\\ \frac{\partial P}{\partial y}\end{Bmatrix}=[B]\{P\} \text{ and } \begin{Bmatrix}\frac{\partial \delta P}{\partial x}\\ \frac{\partial \delta P}{\partial y}\end{Bmatrix}=[B']\{\delta P\} \quad \text{Eq.2-22}$$

with $[B]_{3x2}$ for a linear triangular element as can be obtained from Eq.2-20 and Eq.2-21. This last result allows rewriting Eq.2-12 as:

$$\sum_{e}\left(\left(\int_{\partial\Omega e}\frac{\bar{Q}}{A}[N']dS-\int_{\Omega e}[B']^T[\boldsymbol{D}]\,[B]\,d\Omega\{P\}\right)\{\delta P\}=\int_{\Omega e}\left(\phi\mu c_t\frac{\partial P}{\partial t}\delta P\right)d\Omega\right) \quad \text{Eq.2-23}$$

Now, it is necessary to define the element stiffness matrix as,

$$[K_e]=\int_{\Omega e}[B']^T[\boldsymbol{D}]\,[B]\,d\Omega, \quad \text{Eq.2-24}$$

and the element force vector which applies only to the sides of the elements on the Neumann boundary as:

$$\{f\}=\int_{\partial\Omega e}\frac{\bar{Q}}{A}[N']dS. \quad \text{Eq.2-25}$$

Finally, a solution to the transient term has to be provided in a similar fashion, recalling the pressure definition, $P=[N]\{P\}$ leads to $\dot{P}=[N]\{\dot{P}\}$ and:

$$\int_{\Omega e}\left(\phi\mu c_t\frac{\partial P}{\partial t}\delta P\right)d\Omega=\{\delta P\}^T\left(\int_{\Omega e}\phi\mu c_t[N]^T[N]d\Omega\right)\{\dot{P}\} \quad \text{Eq.2-26}$$

from which the so called mass element matrix can be defined as:

$$[m]=\int_{\Omega e}\phi\mu c_t[N]^T[N]d\Omega \quad \text{Eq.2-27}$$

With the definitions of the element force vector and the mass and stiffness matrices the diffusivity equation finally becomes,

$$\sum_e\left(\{f\}_{3x1}-[K_e]_{3x3}\{P\}_{3x1}=[m]_{3x3}\left\{\dot{P}\right\}_{3x1}\right)\rightarrow\{F\}=[K]\{P\}+[M]\left\{\dot{P}\right\}. \quad \text{Eq.2-28}$$

Having defined the equation above, the only thing left to complete the solution is to define the numerical integration for the shape functions involved. The use of isoparametric coordinates enables the possibility of evaluating the integrals in a simple and orderly fashion. In this coordinate system an integral of the form $\int_{\Omega e}[C]d\mathrm{A}$ can be numerically approximated by the Gauss quadrature to:

$$\int_{\Omega e}[C]d\mathrm{A}\approx\sum_{i=1}^{n_{int}}w_i[C(\xi_i,\eta_i)]\frac{1}{2}J(\xi_i,\eta_i). \quad \text{Eq.2-29}$$

In Eq.2-29, n_{int} is the number of integration points, w_i is the weight of the integration point i and ξ_i and η_i are the coordinates of the integration point. The minimum number of integration points for linear and quadratic triangular elements are 1 and 3 respectively.

Table 2-1 Numerical values for integral computation using isoparametric coordinates.

n_{int}	Integration Points (ξ_i,η_i)	Weights (w_i)
1	$\left(\frac{1}{3},\frac{1}{3}\right)$	1.0
3	$\left(\frac{2}{3},\frac{1}{6}\right),\left(\frac{1}{6},\frac{1}{6}\right),\left(\frac{1}{6},\frac{2}{3}\right)$	$\frac{1}{3}$
3	$\left(\frac{1}{2},0\right),\left(0,\frac{1}{2}\right),\left(\frac{1}{2},\frac{2}{2}\right)$	$\frac{1}{3}$

Table 2-1 contains the number of integration points, their coordinates (ξ_i,η_i) and the respective weights required to compute the integrals in Eq.2-28. It should be noted that for the linear elements any of the three combinations of parameters presented in the table can be used to compute the integrals while

only the two last can be used for the quadratic elements. However, using a higher number of integration points than required does not increase the level of accuracy but does increase the number of computations performed for every element integration. Because this situation may add up to the computational cost of every simulation, it is desirable to use the least number of integration points possible. Finally it is important to mention that the term $J(\xi_i, \eta_i)$ within the integrals corresponds to the Jacobian of the isoparametric transformation and it is the determinant of the matrix in Eq.2-21. More detailed explanation of the method can be found in finite element textbooks (Hughes, 2012; Schrefler & Lewis, 1998).

2.1.3 Three dimensions finite element implementation of the diffusivity equation boundary value problem

The three dimensional solution for the diffusivity equation can be obtained in a similarly to the two dimensions solution in the previous section. The expansion of Eq.2-1 includes now the term for the vertical divergence which is relevant in the transport of eroded grains as it will be demonstrated in the coming sections.

$$\phi \rho c_t \frac{\partial P}{\partial t} = \nabla \cdot \left(\frac{\rho}{\mu} \boldsymbol{k} \left(\frac{\partial P}{\partial x} + \frac{\partial P}{\partial y} + \frac{\partial P}{\partial z} - \rho g \left(\frac{\partial z}{\partial x} + \frac{\partial z}{\partial y} + \frac{\partial z}{\partial z} \right) \right) \right). \quad \text{Eq.2-30}$$

Rearranging the terms on the right hand side of the previous equation leads to,

$$\phi \rho c_t \frac{\partial P}{\partial t} = \nabla \cdot \left(\frac{\rho}{\mu} \boldsymbol{k} \left(\frac{\partial (P - \rho g z)}{\partial x} + \frac{\partial (P - \rho g z)}{\partial y} + \frac{\partial P (P - \rho g z)}{\partial z} \right) \right) \quad \text{Eq.2-31}$$

This result allows the introduction of a new variable known as the flow potential ($\Psi = P - \rho g z$). In the present case this definition can be used because the only interest is to calculate the driving force for fluid motion. This would not be the case for instance if the mechanical stresses of the formation were to be coupled since this depend on the pore pressure exclusively. The transient term on the left hand side of the diffusivity equation is also defined in terms of potential as,

$$\frac{\partial P}{\partial t} = \frac{\partial (\Psi + \rho g z)}{\partial t} = \frac{\partial \Psi}{\partial t} + g z \frac{\partial (\rho)}{\partial t} \rightarrow \frac{\partial (\rho)}{\partial t} \sim 0 \quad \text{Eq.2-32}$$

The assumption of having $\frac{\partial(\rho)}{\partial t}\sim 0$ holds for the present case as very mild changes in fluid density occur during each time step. The function obtained after incorporating the flowing potential (Ψ) is,

$$\phi\rho c_t \frac{\partial \Psi}{\partial t} = \nabla \cdot \left(\frac{\rho}{\mu} \boldsymbol{k} \left(\frac{\partial \Psi}{\partial x} + \frac{\partial \Psi}{\partial y} + \frac{\partial \Psi}{\partial z} \right) \right). \qquad \text{Eq.2-33}$$

Note that unlike the two dimensional case, the density is kept within the first gradient allowing it to vary throughout the system. Repeating the steps taken towards the weak formulation in two dimensions and with the same boundary conditions, the following equation is obtained,

$$\sum_e \left(\int_{\partial\Omega e} \rho \frac{\bar{Q}}{A} \delta P dS - \int_{\Omega e} \left(\frac{\partial \delta\Psi}{\partial x} \frac{\rho}{\mu} k_x \frac{\partial \Psi}{\partial x} + \frac{\partial \delta\Psi}{\partial y} \frac{\rho}{\mu} k_y \frac{\partial \Psi}{\partial y} + \frac{\partial \delta\Psi}{\partial z} \frac{\rho}{\mu} k_z \frac{\partial \Psi}{\partial z} \right) d\Omega \right. \qquad \text{Eq.2-34}$$
$$\left. = \int_{\Omega e} \left(\phi\rho c_t \frac{\partial \Psi}{\partial t} \delta\Psi \right) d\Omega \right)$$

The system is here discretized into linear tetrahedral elements. The element representation in both cartesian and isoparametric coordinates is show in Figure 2-3

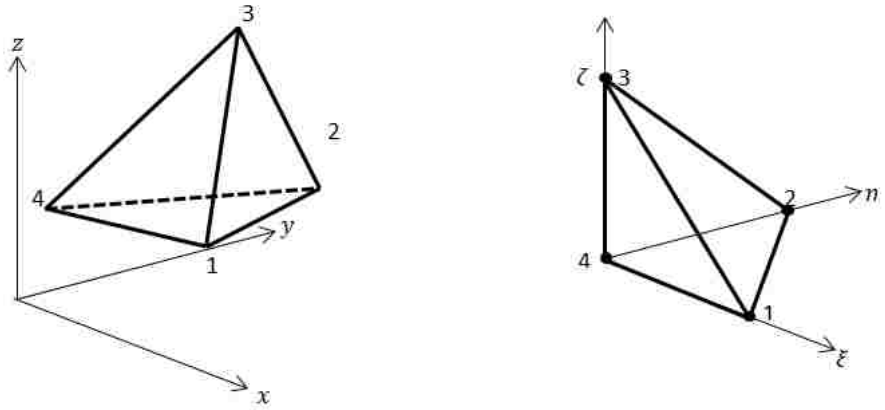

Figure 2-3. Linear tetrahedral elements in cartesian (left) and isoparametric (right) coordinates.

For the linear tetrahedral elements the shape functions are defined as,

$$N_1(\xi,\eta,\zeta) = \xi, \qquad N_2(\xi,\eta,\zeta) = \eta, \quad N_3(\xi,\eta,\zeta) = \zeta \quad N_4(\xi,\eta) = 1 - \eta - \xi - \zeta \qquad \text{Eq.2-35}$$

Following the same procedure as in two dimensions yields the following result,

$$\begin{Bmatrix} \frac{\partial \Psi}{\partial x} \\ \frac{\partial \Psi}{\partial y} \\ \frac{\partial \Psi}{\partial z} \end{Bmatrix} = [B]\{\Psi\} \text{ and } \begin{Bmatrix} \frac{\partial \delta\Psi}{\partial x} \\ \frac{\partial \delta\Psi}{\partial y} \\ \frac{\partial \delta\Psi}{\partial z} \end{Bmatrix} = [B']\{\delta\Psi\}. \quad \text{Eq.2-36}$$

This implies that,

$$\sum_e \left(\left(\int_{\partial \Omega e} \frac{\bar{Q}}{A} \rho [N'] dS - \int_{\Omega e} [B']^T [\boldsymbol{D}] \, [B] \, d\Omega \{\Psi\} \right) \{\delta\Psi\} = \int_{\Omega e} \left(\phi \rho c_t \frac{\partial \Psi}{\partial t} \delta\Psi \right) d\Omega \right). \quad \text{Eq.2-37}$$

With,

$$[\boldsymbol{D}] = \frac{\rho}{\mu} \begin{bmatrix} k_{H\_max} & 0 & 0 \\ 0 & k_{H\_min} & 0 \\ 0 & 0 & k_V \end{bmatrix}. \quad \text{Eq.2-38}$$

The element stiffness, element mass matrix and the force vector are simply

$$[K_e] = \int_{\Omega e} [B']^T [\boldsymbol{D}] \, [B] \, d\Omega, \quad [m] = \int_{\Omega e} \phi \rho c_t [N]^T [N] d\Omega \, , \{f\} = \int_{\partial \Omega e} \frac{\bar{Q}}{A} \rho [N'] dS. \quad \text{Eq.2-39}$$

Similar to Eq.2-28, the resulting system of equations requiring solution is,

$$\sum_e \left(\{f\}_{4x1} - [K_e]_{4x4} \{\Psi\}_{4x1} = [m]_{4x4} \{\dot{\Psi}\}_{4x1} \right) \rightarrow \{F\} = [K]\{\Psi\} + [M]\{\dot{\Psi}\} \quad \text{Eq.2-40}$$

The numerical integration (Gauss Quadrature) is performed as,

$$\int_{\Omega e} [C] dV \approx \sum_{i=1}^{n_{int}} w_i [C(\xi_i, \eta_i, \zeta_i)] \frac{1}{6} J(\xi_i, \eta_i, \zeta_i). \quad \text{Eq.2-41}$$

The corresponding integration points for linear elements are presented in Table 2-2.

Table 2-2. Gauss Quadrature parameters for volumetric tetrahedral elements.

n_{int}	Integration Points (ξ_i, η_i, ζ_i)	Weights (w_i)
1	$\left(\frac{1}{4}, \frac{1}{4}, \frac{1}{4}\right)$	1.0

Having achieved a similar formulation for both two and three dimensional systems, the only procedure left is to actually solve the system of equations. The following section addresses this problem discussing different methods available for both variable storage scheme and actual solution method.

$$\frac{\bar{Q}}{A} = 0. \qquad \text{Eq.2-42}$$

Additionally to the boundary conditions in two dimensions, the top and bottom of the reservoir are set as non-slip boundaries meaning no flow across them (Eq.2-42), if this is not the case, then channels formed close to this boundaries extend uncontrollably towards them as it becomes mathematically an easy flow path for the injected fluid but does not represent a realistic situation.

2.1.4 Solution to the system of equations

Solving Eq.2-28 or Eq.2-40 is rather a simple procedure and many methodologies both explicit and iterative are available in the literature to come to a solution and obtain the system's pressure. However, it is important to realize that this process is one of the most computationally intensive sections of the problem making it imperative to implement one that is both accurate and efficient.

First, the time derivative term $\{\dot{P}\}$ shall be discretized by means of backward finite difference of first order as:

$$\{\dot{P}\} = \frac{1}{\Delta t}(\{P\} - \{P\}_{t-1}) \qquad \text{Eq.2-43}$$

with Δt being the timestep $\Delta t = t_t - t_{t+1}$ that will be defined later. Introducing the time discretization and rearranging terms in Eq.2-28 results in:

$$\{F\} + \frac{1}{\Delta t}[M]\{P\}_{t-1} = ([K] + [M]/\Delta t)\{P\}. \qquad \text{Eq.2-44}$$

If we define the resulting matrix as $[K] + [M]/\Delta t = [A]$ and the vector that results from the terms on left hand side as $\{F\} + \frac{1}{\Delta t}[M]\{P\}_{t-1} = \{B\}$ then:

$$\{B\} = [A]\{P\}. \qquad \text{Eq.2-45}$$

With the methodology introduced in the previous section it is possible to obtain $\{B\}$ and $[A]$ and it is then only required to solve for the pressure $\{P\}$ as a final step to reach the solution to the boundary value problem here stated. As a first step towards the solution of the system of equations here developed, the storage of the variables in Eq.2-45 should be given consideration. The Random Accesss Memory (RAM) of a computer determines the size of a simulation that can be run on a determined machine. Storage may

sometimes become a problem, especially for $[A]$ which is a NxN matrix, where N is the number of nodes the system domain is discretized into. As it will be shown later, systems of up to 9000 nodes are used in the two dimensions problem which would require as much as $9{,}000x9{,}000x16 = 1.296\text{GB}$ of memory to build this matrix for one timestep. This situation may impair the ability of a computer to perform the calculations required to do any activity such as running an application to solve a system of equations. The problem is easily avoided by only storing the non-zero terms of the corresponding sparse and symmetric matrix $[A]$ in skyline form. It is important to notice that since we are dealing with a symmetric matrix, storing only the upper half of the system is enough. The skyline form is a way to store the corresponding NxN matrix in two vectors: the diagonal containing vector ($\{jdiag\}$) and a vector containing the matrix's values ($\{sk\}$) mostly non-zeros above the diagonal.

The vector $\{sk\}$ holds the values on the matrix for every column from the first non-zero value until the diagonal. The concept can be better understood by looking at Figure 2-4. $\{sk\}$ is an $1x(NxH_{avg})$ in size vector where H_{avg} is the average height of a column from the first non-zero term to the diagonal. On the other hand, the vector $\{jdiag\}$ contains the location in $\{sk\}$ of the diagonal value for every column which makes it a $1xN$ vector.

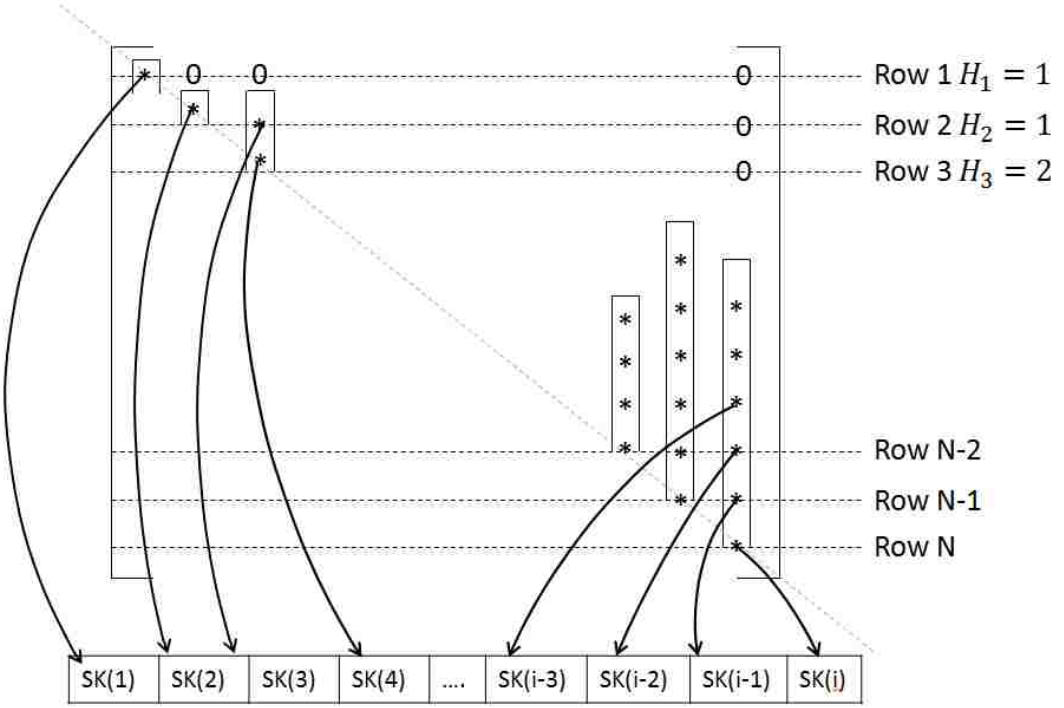

Figure 2-4. Schematic representation of SK vector for the storage of sparse matrices in skyline form

With this form of storage, the improvement is from having NxN points in $[A]$ stored to NxH_{avg}. It is hard to quantify the average height (H_{avg}) for every column since the quantity depends on the arrangement of the elements in the system which can vary significantly. Referring again to the nine thousand nodes system implemented in future sections, the improvement goes from storing 81 to around 1.1 million data points, this will free up space in the RAM allowing the fast computation of the solution algorithms.

The number of zero valued cells in $\{sk\}$ trapped between the first non-zero value and the diagonal are still significant. For the case that has been referred to it came to have a total of only 32,400 non-zero doubles while the rest, more than 1,05 million values stored were zeroes. This left room for further optimization of the storage scheme which resulted in a simpler much effective scheme later used in the three dimensional implementation. The upper half of $[A]$ was stored in three vectors, $\{col\}, \{row\}$ and {a} all of the same size. Vector $\{a\}$ has only non-zero doubles in $[A]$, while $\{col\}$ and $\{row\}$ contain the column and row respectively in $[A]$ for every number stored in $\{a\}$. For the case having almost nine

thousand nodes this reduces the storage requirements from 1.296GB to 1.555MB. The new storage scheme is crucial to the much larger systems used in three dimensions.

Having defined proper storage, inverting $[A]$ and multiplying it by $\{B\}$ is required at every time step in order to obtain the system's pressure. Many methods were reviewed mainly assessing the complexity of implementation and efficiency of them to make a proper selection. For instance Gaussian elimination, a common and explicit method was analyzed; however, it is by itself a computationally expensive method for the size of systems here implemented. The Cholesky method was also considered, it decomposes $[A]$ into $[L][L]^T$ having $[L]$ been a lower triangular matrix which through forward elimination and back substitution results in a more efficient version of Gaussian elimination. This method was actually implemented and tested against the iterative conjugate gradient method. The conjugate gradient method results in a much more efficient and easier to implement algorithm. Having an easy to implement method has the advantage of being easily altered when deficiencies or further space for optimization are realized.

The conjugate gradient method constitutes an iterative method that can solve the linear system of equations in Eq.2-45. The iterative method defines a series of approximations $\{P\}_1, \{P\}_2, \dots \{P\}_i$ which eventually converge to $\{P\}$. The error of the ith approximation is $\{P\}_i - \{P\}$, with the residual being:

$$\{R\}_i = [A]\{P\}_i - \{B\}. \qquad \text{Eq.2-46}$$

The criteria here established for convergence is based on the residual as:

$$\frac{\|\{R\}_i\|}{\|\{B\}\|} > \epsilon \qquad \text{Eq.2-47}$$

in which ϵ is the tolerance that for all the simulations in this document is 10^{-10}. The pseudo-algorithm for the method is:

- Make an initial guess for $\{P\}$. In the dynamic problem of interest it is logic to consider the pressure from the previous step as a guess since this is not expected to vary considerably between time steps, even if it was the case, at least a proper order of magnitude will be achieved reducing the number of iterations required.
- Check for convergence as in Eq.2-47. If convergence met, stop, otherwise proceed.

- Calculate α_i as:

$$\alpha_i = -\frac{\{S\}^T\{R\}}{\{S\}^T\{[A]\{S\}\}} \quad \text{Eq.2-48}$$

In this equation α_i is the magnitude in which $\{P\}_{i-1}$ is to be corrected in the direction $\{S\}$ as:

$$\{P\} = \{P\} + \alpha\{S\}. \quad \text{Eq.2-49}$$

- Update the residual:

$$\{R\} = \{R\} + \alpha\{[A]\{S\}\} \quad \text{Eq.2-50}$$

- Calculate the corrective factor for the direction in which the solution is being pursued:

$$\beta = -\frac{1}{\alpha}\frac{\{R\}^T\{R\}}{\{S\}^T\{[A]\{S\}\}} \quad \text{Eq.2-51}$$

- Finally, update the direction of search of a solution

$$\{S\} = \{R\} + \beta\{S\} \quad \text{Eq.2-52}$$

This solution, unlike the Cholesky method is easy to implement even when $[A]$ is stored in the three vector scheme described earlier. The most complicated step of the algorithm pops up whenever a matrix vector multiplication is required. This action, part of another subroutine is the key component of the method's efficiency which results in very few calculations on every iteration. The most interesting property of the method is that its computational cost is in general a linear function of the number of nodes unlike other methods which cost increases exponentially as the system is refined.

2.2 Channelization Models and Criteria for Sediment Motion

Having defined the computation of pore pressure through the diffusivity equation with respective boundary conditions leads to the next step; obtaining a mathematical model that represents the erosional phenomenon that calculates the detachment and transport of granulated material due to fluid injection. First, a theoretical background on the force required to move a grain is performed through Shield's number followed by a brief comparison of methods that directly relate to subsurface erosion.

2.2.1 Shields number as a condition for initiation of sediment movement

The Shields dimensionless number is a criterion that intends to establish the required force that a fluid in motion needs to apply to a solid particle laying on the top of a sand bed for this to initiate motion (Shields, 1936). Although in this work the particles of interest are buried under thousands of feet of sediment, are subject of immense compressive stresses and may exhibit a certain degree of cementation, the Shields number can be thought of the baseline beyond which there will not be any chance for sediment to move. Physically, the Shields number is the ratio of the fluid induced force to the particle weight. The number is defined as,

$$\theta = \tau / gd(\rho_s - \rho_f) \qquad \text{Eq.2-53}$$

In Eq.2-53, τ represents the shear stress imposed by the fluid, ρ_s is the solid sediment density, ρ_f is the fluid density and d is the grain characteristic diameter. Initially, the Shields number was plotted as a function of a critical Reynolds number which would in turn define the point at which particles begin flowing along with the fluid. The charts comprised of Shields vs. Reynolds number calculations are referred to as Shields curves.

After Shields (1936) work, researchers have accumulated a series of experimental data that contribute to the buildup of a uniform criterion aiming to predict motion initiation due to fluid induced stresses. A significant amount of data produced so far was compiled and transformed by Beheshti and Ataie-Ashtiani (2008). The observations and analysis of experimental data sources has led to the development of a new concept instead of the Shields curves: the dimensionless grain diameter,

$$D_g = \left(\frac{\rho_s - \rho_f}{\rho_f \left(\frac{g}{\nu^2} \right)} \right)^{1/3} d \qquad \text{Eq.2-54}$$

Different numerical relations between the dimensionless grain diameter (D_g) and the critical Shields number as obtained by Beheshti and Ataie-Ashtiani (2008) from different publications are disclosed in Table 2-3. The functions for the critical Shields number in the table and experimental data available in the literature have been plotted to show the predicting capabilities of the underlying equations. According to

the authors, the experimental data corresponds to more than 153 independent measurements which are considered a big enough sample in order to appropriately assess the accuracy of the different correlations.

Table 2-3 Multiple critical Shields number correlations as a function of the dimensionless diameter (D) (Table reproduced from Beheshti & Ataie-Ashtiani (2008)).

Critical Shields number as a function of dimensionless diameter		
Author	**Formula**	**Validity**
Bonnefille (1963)	$\theta_{cr} = \begin{cases} 0.118D^{-0.468} \\ 0.137D^{-0.648} \\ 0.063D^{-0.468} \\ 0.9D^{0.424} \end{cases}$	$D < 2.33$ $2.33 \leq D < 9.15$ $9.15 \leq D < 15.28$ $15.28 \leq D < 58.3$
Chien (1983)	$\theta_{cr} = \begin{cases} 0.126D^{-0.44} \\ 0.131D^{-0.55} \\ 0.0685D^{-0.27} \\ 0.0173D^{0.19} \\ 0.0115D^{0.3} \\ 0.052 \end{cases}$	$D < 1.5$ $1.5 \leq D < 10$ $10 \leq D < 20$ $20 \leq D < 40$ $40 \leq D < 150$ $150 \leq D$
Paphitis (2001)	$\theta_{cr} = \frac{0.273}{1 + 1.2} + 0.046(1 - 0.576e^{-0.02D})$	$0.01 < Re < 10^4$
Cheng (2004)	$\theta_{cr} = \begin{cases} 0.120D^{-0.5} \\ 0.026D^{0.167} \\ 0.06 \end{cases}$	$D < 10$ $10 \leq D < 150$ $150 \leq D$
Sheppard & Renna (2005)	$\theta_{cr} = \begin{cases} 0.25 + 0.1D^{-0.5} \\ 0.0023D - 0.000378D\ ln(D) + 0.23/D - 0.005 \\ 0.0575 \end{cases}$	$0.1 < D < 3$ $3 \leq D < 150$ $150 \leq D$
Cao et al. (2006)	$\theta_{cr} = \begin{cases} 0.1414R_d^{-0.2306} \\ \frac{[1 + (0.0223R_d)^{2.8358}]^{0.3542}}{3.0946R_d^{0.6769}} \\ 0.045 \end{cases}$ $R_d = d\sqrt{(S_s - 1)gd/v}\ \ S_s = \rho_s/\rho_f$	$R_d \leq 6.61$ $6.61 \leq R_d < 282.84$ $282.84 \leq R_d$

The results plotted in Figure 2-5 show that the available correlations catch the trend of the critical Shields number with respect to the dimensionless diameter; however, these could hardly be used quantitatively as the spread shown by the data is quite big. The best fit is obtained for dimensionless diameters below 10, beyond this number plenty of the data do not fit within the bands created by plotting the multiple correlations.

In 1957 and taking a slightly different approach, Liu (1957) came up with a different dimensionless number later named movability number u/w_s in which w_s is the settling velocity of particles defined by Stokes' law as,

$$w_s = \frac{2}{9}\frac{(\rho_s - \rho_f)}{\mu} g R^2. \qquad \text{Eq.2-55}$$

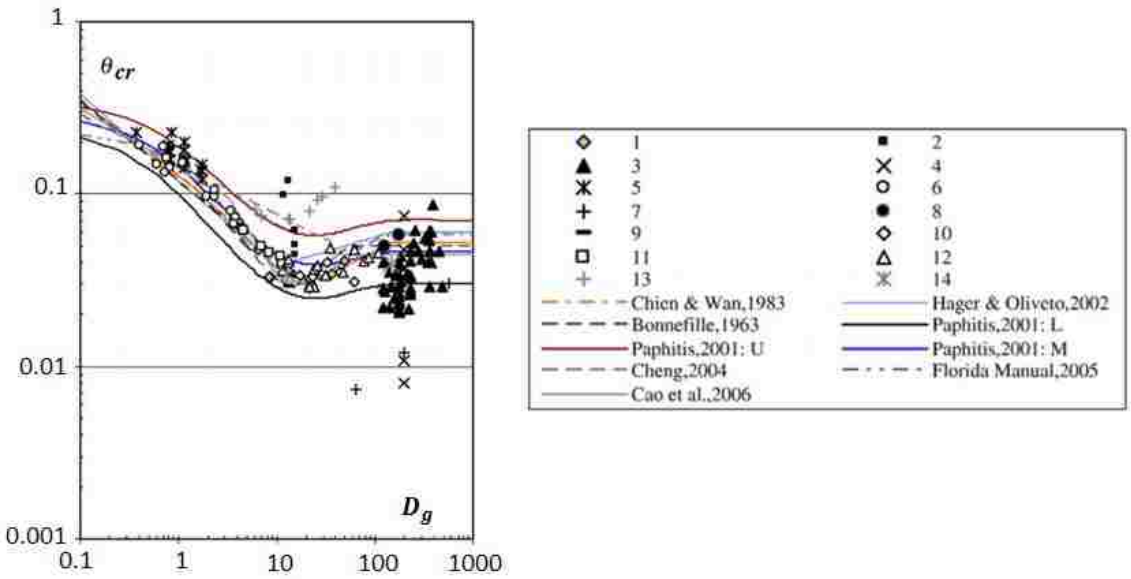

Figure 2-5. Measured data vs. empirical correlations predicting critical Shields number as a function of the dimensionless grain diameter (Beheshti & Ataie-Ashtiani, 2008).

An empirical correlation claimed to be more accurate than Stoke's Law for the settling velocity was later proposed by Wu and Wang (2006).

$$w_s = \frac{Mv}{Nd}\left[\sqrt{\frac{1}{4} + \left(\frac{4N}{3M^2}D_g^3\right)^{\frac{1}{n}}} - \frac{1}{2}\right]^n \qquad \text{Eq.2-56}$$

$M = 53.5e^{0.65S_f}; N = 5.65e^{-2.5S_f};\ n = 0.7 + 0.9S_f; S_f = c/\sqrt{ab}$ (Shape factor).

In Eq.2-56, parameters a, b and c are the length of the longest, intermediate and shortest axes of the particles. The shape factor (S_f) can be assumed to be 0.7 as it the most common factor found in natural occurring sediments. The results of the empirical equation compared to those previous to that breakthrough are displayed in Figure 2-6. The results present a mean relative error of 9.1% as stated by the authors which happens to be the smallest among a set of 4 different correlations.

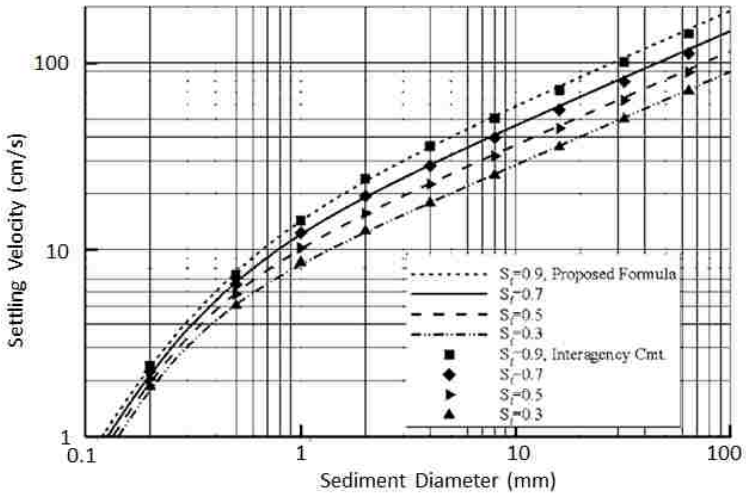

Figure 2-6. Proposed empirical correlations predicting sediment settling velocities as a function of sediment diameter compared to previously accepted correlations (Wu & Wang, 2006).

With the ability to calculate the settling velocity, Paphitis (2001) proposed a formula to determine the critical movability number at which particles begin to move (Eq.2-57).

$$\frac{u_*}{w_s} = \frac{0.75}{Re_*} + 14e^{-2Re_*} + 0.01 \ln Re_* + 0.115 \quad (0.1 < Re_* < 10^5) \qquad \text{Eq.2-57}$$

$$Re_* = u_{*_c} d/v$$

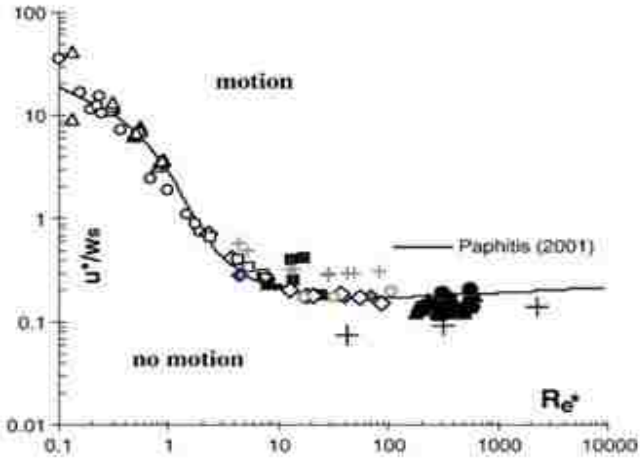

Figure 2-7. Critical movability number ($\boldsymbol{u^*/w_s}$) as a function of the critical Reynolds number with zone of no sediment motion (below the curve) and zone of motion (above the curve) (Beheshti & Ataie-Ashtiani, 2008).

When plotted with the experimental data points in Figure 2-5, the correlation yields the results in Figure 2-7. The outcome shows a substantial improvement from the use of the empirical correlations

through the dimensionless diameter to calculate the critical Shields number. The measured points' behavior is well predicted even more so for Reynolds' numbers lower than 10. With these results and in an attempt to further simplify the determination of the critical conditions for motion, Beheshti & Ataie-Ashtiani (2008) proposed the empirical correlation,

$$\frac{u_*}{w_s} = \begin{cases} 9.6674 D_g^{-1.57}, & D_g \leq 10, \quad R^2 = 0.9954 \\ 0.4738 D_g^{-0.226}, & 10 < D_g, \quad R^2 = 0.578 \end{cases} \qquad \text{Eq.2-58}$$

The resulting plot from the latter is displayed below.

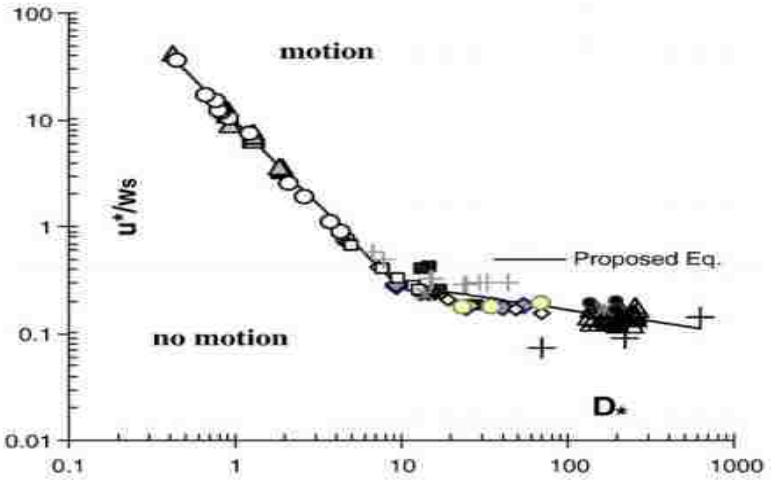

Figure 2-8. Critical movability number ($\boldsymbol{u^*/w_s}$) as a function of the dimensionless diameter (Beheshti & Ataie-Ashtiani, 2008).

Until now, a review of the available criteria to determine when particles begin moving as consequence of fluid induced forces has been performed. These criteria are in line with the believe that particles in unconsolidated porous media move as a consequence of a pressure gradient rather than a stress itself. In a porous medium, the fluid velocity (u_c) is proportional to the pressure gradient as stated in Darcy's law. Although this section does not deal directly with the mobilization of buried sand particles, it can be thought as a baseline for the underlying problem. The concepts outline are a proper base for understanding the nature of the problem that have demonstrated to be more accurately represented by empirical correlations rather than equations derived from physical principles.

2.2.2 Quantification of Number of Eroded Particles Erosion

The previous section addressed the developments made by different researchers on the required conditions to achieve grain movement, however, no efforts on quantifying the portion of particles moving has been exposed yet. This section reveals some of the numerical approximations that have been proposed in this regard, one of them is selected to be used to quantifying erosion as a function of space and time.

Dancey et al. (2002) proposed a simple and time dependent condition for the movement of particles in a particle bed,

$$n = m\Gamma(t/\zeta) \qquad \text{Eq.2-59}$$

In this equation, n is the number of grains moving over a period of time (t), m is the total available sediment particles which can be easily obtained from the discrete volumes of a system and particle size distributed over a finite space, Γ being the probability of grain movement and ζ being the average period between turbulent events. The method seems more suitable for transient events due to the latter term but could still be fitted to suite pseudo-transient events as those of interest. Γ has a proposed value of $3.58x10^{-5}$ for the threshold for movement. Rather than giving Γ a constant value, a function dependent on the drag forces induced by the fluid in motion could be proposed. This method provides two main advantages: 1) It incorporates the relevance of time dependent parameters and 2) the erosion (i.e. the amount of sediment in motion) can be computed through m and n. Unfortunately, for the present work this method would be incomplete requiring multiple additions for its implementation.

Over a relatively limited number of numerical propositions intended to represent the erosion and transport of sediment in sub surface formations, those of Spiegelman (1993), Mahadevan et al. (2012), Papanastasiou et al. (2015) were given consideration. The publications were chosen primarily because they consider that erosion is proportional to the pressure gradient that arises from the motion of the fluid through the permeable media. This concept is important because the drag forces suffered by a particle at rest are driven by the pressure gradient. Through Darcy's law, the pressure gradient is related to important properties that are here accepted to have an effect over formation erosion.

$$q = -\frac{k}{\mu}\nabla P \qquad \text{Eq.2-60}$$

The first of these variables is the permeability or rock imposed resistance to flow to a certain fluid, the lower the permeability the higher the shear forces over the rock due to fluid flow when all other variables are kept constant. Opposed to the effect of permeability, a lower fluid viscosity will decrease the forces acting on static grains. Also, the fluid flux (q) which is not the velocity that a fluid particle experiments, will proportionally dictate the effort the fluid is doing on a solid particle for this to move. The actual fluid velocity (u) is related to the pressure to the flux as,

$$u = \frac{q}{\phi}. \qquad \text{Eq.2-61}$$

Eq.2-61 implies then that in general terms porosity (ϕ) is the last variable on which erosion depends at least in the case in which compressive stress are not considered.

Another important consideration that the three models under scrutiny account for is the definition of three different phases, namely, a fluid phase, a static granular phase and a mobile granular phase. The three phases are important because they allow the use of continuity equations or in other words the mass balance of the solid particles in motion. Failure to account for this physical phenomenon makes it unsuitable to properly model sand transport within the formation.

The model by Papanastasiou et al. (2015) proposes radial or ring shape erosion, this implies that erosion is strictly a function of the distance to the wellbore. This consideration has been widely proven wrong through experiments and simulations (Hosseini, 2012; Mahadevan et al., 2012; Zhang, et al., 2013). Moreover, having radial erosion makes hard to consider cases in which the wellbore has complex completions such as frac-packs in which the formation cannot be considered axisymmetric. Due to the radial consideration of erosion and the tough task that it would represent to make the equations more general, the model was disregarded. However, it is important to outline that the system of equations includes geomechanical considerations (i.e. it considers formation compressive stresses) which are relevant.

Finally, the formulation by Spiegelman (1993) is not implemented as it is intended for phenomena such as magma migration which is not exactly the interest of this research. An important consideration from this model is the independent approach to particle flow and fluid transport. This capability could be given consideration if this last property is deemed relevant to the problem on future studies. Along with the reasoning behind discarding the previous formulations, the model proposed by Mahadevan et al., (2012) is chosen for two main reasons: 1) It does not consider any axis of symmetry and 2) it has been tested against experimental results which demonstrates its capabilities to recreate actual physical observations.

2.2.3 Erosion Model Implemented

The basis of the model developed for sand particles motion due to erosion is defined in the context of multiphase theory implemented similarly to Mahadevan et al. (2012). In this section, a brief description of the mathematical model used to simulate fluid-induced channelization in porous media is described. The model decomposes the sand matrix into three phases, liquid, mobile grains and the solid matrix which volumetric fractions are represented by ϕ_l, ϕ_m and ϕ_s respectively. The time-evolution of these phases is described by the mass balance of each phase and the conversion of mobile into immobile solids and vice versa (Eq.2-62-Eq.2-64). The exchange between the solid phases is described by Eq.2-66 and Eq.2-68 that represent the rates of erosion (e) and deposition (d).

$$\frac{\partial \phi_s}{\partial t} = d - e \qquad \text{Eq.2-62}$$

$$\frac{\partial \phi_m}{\partial t} = e - d - \nabla \cdot (\phi_m u_g) \qquad \text{Eq.2-63}$$

$$\frac{\partial \phi_l}{\partial t} = -\frac{\partial (\phi_s + \phi_m)}{\partial t} = -\nabla \cdot (\phi_l u_l) \qquad \text{Eq.2-64}$$

Adding equations the latter 3 yields the global mass balance,

$$\nabla \cdot (\phi_m u_m + \phi_l u_l) = 0. \quad \text{Eq.2-65}$$

If the velocities of the mobile and liquid phases are assumed to be the same, such that $u_m = u_l = u$, then, the continuity equation reduces to $\nabla \cdot (\phi u)$. In the latter, the porosity (ϕ) is given by the addition of both liquid and mobile phases fractions as $\phi = \phi_l + \phi_m$.

$$e = k_e \phi_s ((\gamma^{-1} \nabla p)^2 - \sigma) \geq 0 \quad \text{Eq.2-66}$$

In Eq.2-66, k_e is the characteristic rate of erosion and γ is the ratio of the characteristic fluid velocity to the hydraulic conductivity (q_0/D_0) which is used to normalize the pressure gradient. Failure stress (σ) is a function of average volume fraction as,

$$\sigma = C * \left(\tanh\left(2\pi(\overline{\phi_s} - 0.6)\right) + 1\right). \quad \text{Eq.2-67}$$

It can be noted that *e* is dependent on the pressure gradient which as stated before is the main driving force of erosion. The critical stress σ should be a function of the solid fraction ϕ_s. However, the average of the neighbors' solid matrix fraction $(\overline{\phi_s})$ is used instead of the exact solid fraction to mimic the dependence of the granular failure (σ) on the surrounding grains. The weighted spatial average is calculated numerically as an average of the neighbors surrounding a single point. The value of σ can be thought as the inter-grain forces that the fluid has to overcome to convert an immobile particle to a mobile one and that is counteracting the fluid induced drag forces. The failure coefficient C can be varied to represent the degree of consolidation and the in-situ stresses (e.g. in the presence of resin coated proppants, the value of C should increase).

The critical stress (σ) is a key term on the model as it will make the overall erosion higher at points of higher porosity. If this was not the case, the entire matrix would erode until the porosity was evenly distributed everywhere in the system. The concept can be envisioned in Figure 2-9 in which the critical stress is plotted against the average porosity $(1 - \overline{\phi_s})$.

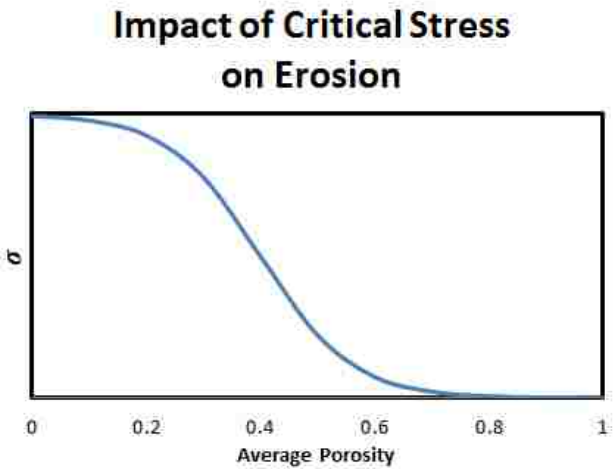

Figure 2-9 Dependence of critical stress on porosity. As porosity increases $\boldsymbol{\sigma}$ decreases making erosion higher when porosity is large.

To estimate deposition, the rate at which the mobile granular grains are transformed back to an immobile solid phase is given by,

$$d = k_d\,(\phi_s - \phi_s^*)\,\phi_m \geq 0, \qquad \text{Eq.2-68}$$

where ϕ_s^* is a depositional threshold beyond which particles cannot be deposited and the characteristic deposition rate, k_d is,

$$k_d = k_e = \frac{q_0}{L} \qquad \text{Eq.2-69}$$

When implemented by Mahadevan et al. (2012), the Carman-Kozeny equation was formulated differently to all known available correlations having the exponent in the denominator within the parenthesis,

$$k = \frac{\psi^2 l_g^2 \phi^3}{A(1-\phi^2)}, \qquad \text{Eq.2-70}$$

unlike Eq.2-2. If the Carman-Kozeny correlation is corrected and the model is implemented with the diffusivity equation as in section 2.1.1, the model fails and a simple washout of the entire formation occurs. The severity of computing using the different C-K equation can be observed in Figure 2-10.

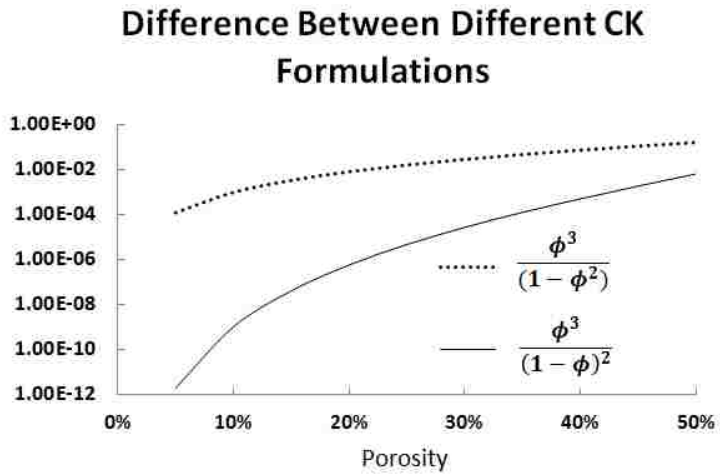

Figure 2-10. Porosity dependent factor of the Carman-Kozeny equation as a function of porosity for the correct formulation (solid line) and the wrong formulation (dashed line).

The results show the effect obtained on the porosity dependent factor of the permeability for the two different formulations for values of porosity from 5% to 50%. The wrong correlation yields at least a two orders of magnitude higher permeability which in turn makes the pressure gradient a much weaker function of permeability. The pressure gradient then affects the erosion model specifically in Eq.2-66, this situation makes the model as initially proposed hard to implement.

Through a thorough analysis of the equations and the effects of the different permeability correlations, Eq.2-66 was modified by multiplying the normalized pressure gradient by $\phi^{3/2}$,

$$e = k_e \phi_s \left(\phi^{3/2} (\gamma^{-1} \nabla p)^2 - \sigma \right) \geq 0. \qquad \text{Eq.2-71}$$

As it will be shown in sections to come, having changed the erosional model made it possible to achieve similar results to those of Mahadevan et al. (2012) while using the correct Carman-Kozeny equation.

CHAPTER 3: VALIDATION OF FLUID FLOW EQUATIONS AND EROSIONAL MODEL

3.1 Validation of Fluid Flow and Erosional Model on a Squared Two Dimensional Plate (linear case)

All the models and numerical methods presented are implemented using MATLAB, a few validations against analytical solutions are performed to assure both the validity and correct implementation of the model. The model is first implemented on the same geometry as Mahadevan et al. (2012), this is a square 1x1ft^2 plate packed with sand which representation is available in Figure 3-1. Because the author did not have a dynamic fluid flow set of equations nor did Ameen and Dahi Taleghani (2014), the simulations in this chapter are the result from using steady state fluid flow equations meaning, $\partial P/\partial t = 0$ in Eq.2-1, that is equivalent to having $[M] = 0$ in Eq.2-28.

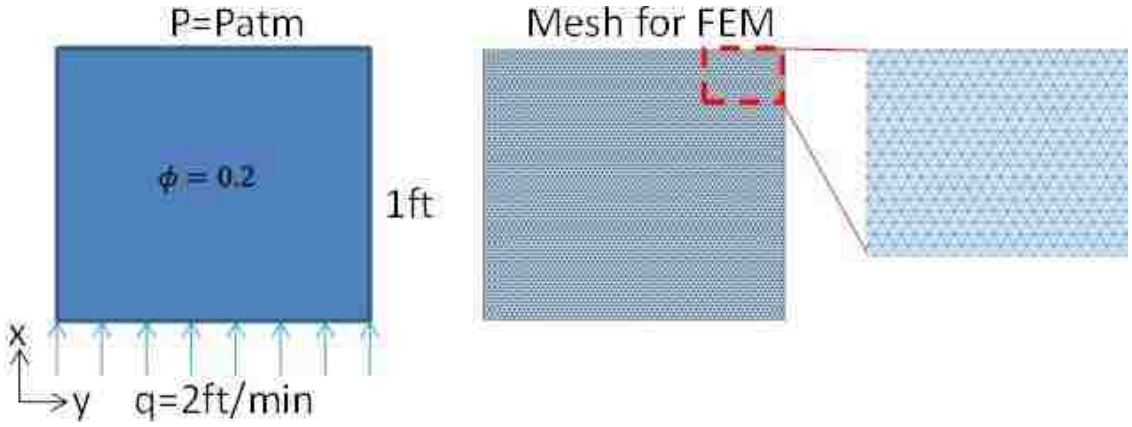

Figure 3-1. Injection plate representation (left) and system discretization for FEM (center) with zoom-in (right).

The system above consists of a plate packed with sand which initial porosity is estimated at around 20%. Water is being injected at the bottom at a velocity of 2ft/min and the other end is open to the atmosphere. The latter are the two boundary conditions required to run the channelization model in section 2.1.1. The first simulation that will be performed uses a homogeneous porosity distribution over the entire plate which is physically not achievable. This simulation is run because the pressure profile for this system is linear, this makes the solution for the FEM implementation exact which allows the comparison of it with the analytical solution of Darcy's law coupled to the channelization model. The

system has no physical significance but provides an easy way to assess the implementation of the FEM code.

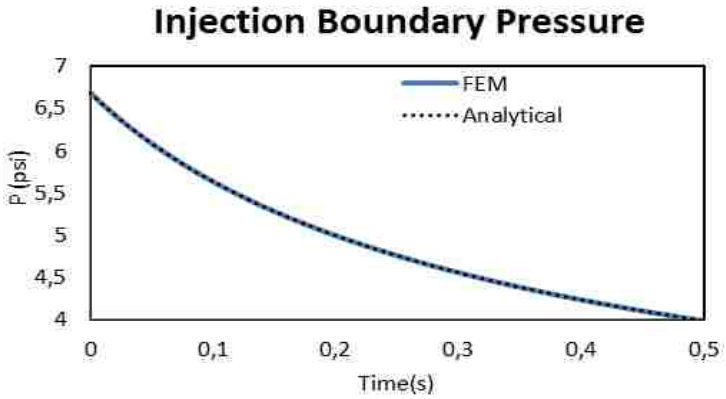

Figure 3-2.Pressure at the lower (injection) boundary of packed plate.

The pressure at the lower boundary of the system over time is shown in Figure 3-2, the parameters used in the simulations are not disclosed as the result itself only provides assurance that the model has been implemented correctly. Following this case, three additional runs on the $1x1ft^2$ plate, now for the more realistic cases in which there is porosity heterogeneity across the media were performed. The different scenarios were chosen according to past implementations by both Rostami and Dahi Taleghani (2014) and Mahadevan et al. (2012). All three final porosity distributions are presented in Figure 3-3.

The first case corresponds to a system with a random porosity distribution with a 1% standard deviation. Also, the injection velocity is one third of that of the homogeneous simulation. The results show the system basically suffering a washout with a final porosity distribution of around 60%. Although not the same, the results from the current FEM implementation and that of Rostami and Dahi Taleghani (2014) seem to lie very close. Results cannot be the same as the spatial discretization and different initial porosities are used.

The next case has a random distribution just as in the first one but has two channels with 22% initial porosity. Both results for Mahadevan et al. (2012) and the FEM code show the channels having higher erosion than anywhere else after a certain time of injection. This is an expected result as the higher porosity implies higher permeability hence more fluid will travel through these areas increasing the drag

forces on the grains. It is clear though that the FEM solution shows lower porosity around the induced channels compared to that of Mahadevan et al. (2012).

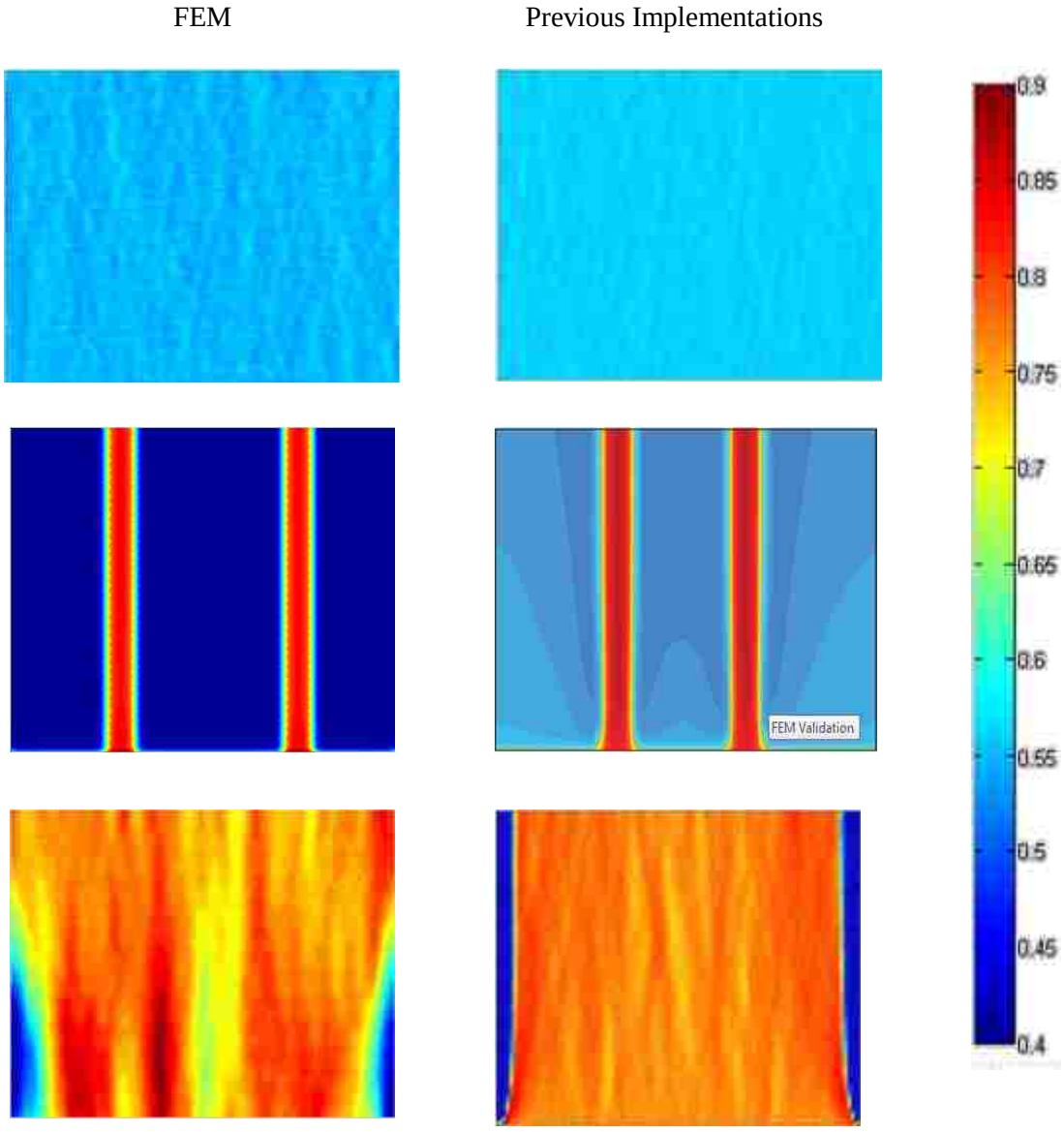

Figure 3-3. Final porosity distribution after fluid injection into sand packed plate, comparison between current FEM solution (left) and implementations by Rostami and Dahi Taleghani (2014) and Mahadevan et al. (2012) (right).

The third case consists of a plate with $20\% \pm 1\%$ with an injection velocity three times that of the first case. The resulting porosity is a complete washout of the sand in the plate having a final porosity of almost 80%. The area close to the plate walls remains at a low porosity as if there was a no slip condition

at the walls. The FEM result has a less homogeneous final porosity distribution showing areas with porosities as low as 65%.

The results displayed in Figure 3-3 had the intention of validating the FEM implementation with those performed by others. The problem of our interest lies in a reservoir-wellbore geometry that was the step after consistent results were achieved on the square shape geometry.

3.2 Validation of the Diffusivity Equation on a Reservoir-Wellbore Geometry

To perform simulations on reservoir geometry, a system consisting on a 7in wellbore and a cylindrical reservoir with a radius of 150ft was created (Figure 3-4). The MESH is refined close to the wellbore were more detailed caption of erosion during injection is required while at the outer boundary the mean element size is bigger. This configuration allows an accurate representation of the physical phenomena while diminishing the computational cost of the simulations significantly. The mesh contains 8682 nodes and over 17,000 elements and is obtained using an open source mesh generator for Matlab (Persson & Strang, 2004).

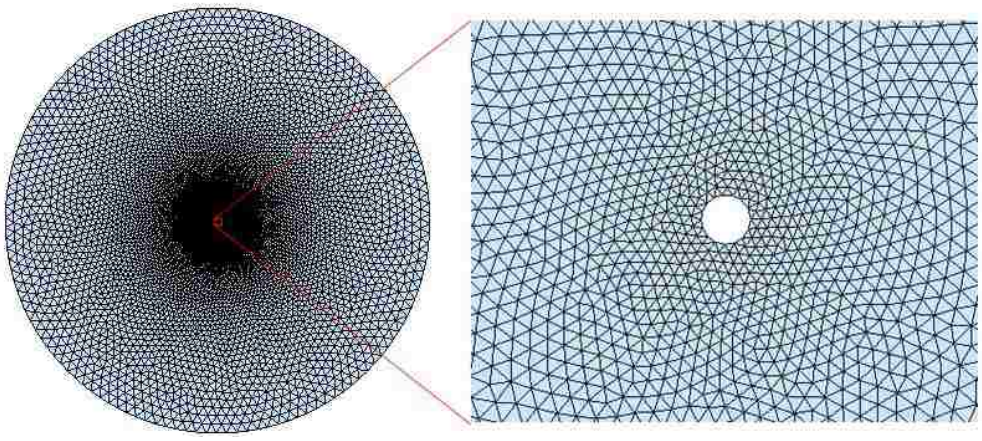

Figure 3-4. System discretization (MESH) for a reservoir geometry.

The reservoir radius might be thought of a small one but since our interest lies on calculating the pressure gradient which only depends on the hydraulic conductivity and the fluid velocity, the reservoir radius has no effect on the erosion as long as all of the channels formed through erosion remain at a safe distance from the reservoir boundary.

In order to assess both the accuracy and correct implementation of the FEM numerical solution, simple tests were conducted against known analytical results for cases for which this is possible. For the tests and future simulations unless stated otherwise, the parameters in Table 3-1are used.

Table 3-1. Relevant parameters for fluid flow simulation.

Parameter (symbol)	Value (units)
Injection rate (Q) (**NOTE**: 10ft thick payzone)	5995 (bpd)
Particle Size (l_p)	0.004 (inches)
(A)	180
Sphericity (ψ)	1
Viscosity (μ)	1(cP)
Porosity (ϕ)	25%
Formation Compressibility (c_f)	4.53E-5 (psi^{-1})
Water Compressibility (c_w)	3E-6(psi^{-1})

The injection rate is chosen as a common injection rate for this type of wells and supported by the well history in Figure 1-1, the mean particle size was obtained from the Sand Control Handbook (Suman et. al., 1983), and modified to include the completions gravel to meet that by Penberthy and Shaughnessy (1992), the authors provide a plot for the particle size distribution in the Gulf of Mexico available in Figure 3-5. The fluid viscosity is that of water, the porosity is an average porosity found in a poorly consolidated reservoirs in the Gulf of Mexico while the formation and water compressibilities where obtained from the Standard Handbook of Petroleum and Natural Gas Engineering (William & Gary, 2005).

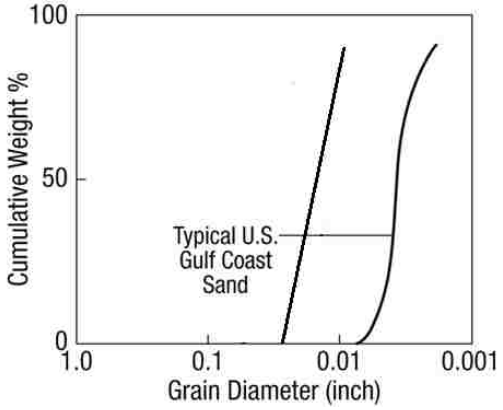

Figure 3-5. Typical offshore Gulf of Mexico formation particle size distribution (Suman et. al., 1983).

To assess the system for a heterogeneous case, the porosity is set as,

$$\phi = \begin{cases} 0.35 \text{ for } r_w < r < 50ft \\ 0.25 \text{ for } r > 50ft \end{cases} \quad \text{Eq.3-1}$$

This case is chosen as it represents a heterogeneous system for which an analytical solution is known. Remember that the formation permeability has been made a function of porosity hence a discontinuity in the pressure derivative as a function of the distance to the wellbore when steady state is reached is expected. To show the obtained results, the pressure at every node after the system stabilizes is plotted as a function of its distance to the wellbore (Figure 3-6).

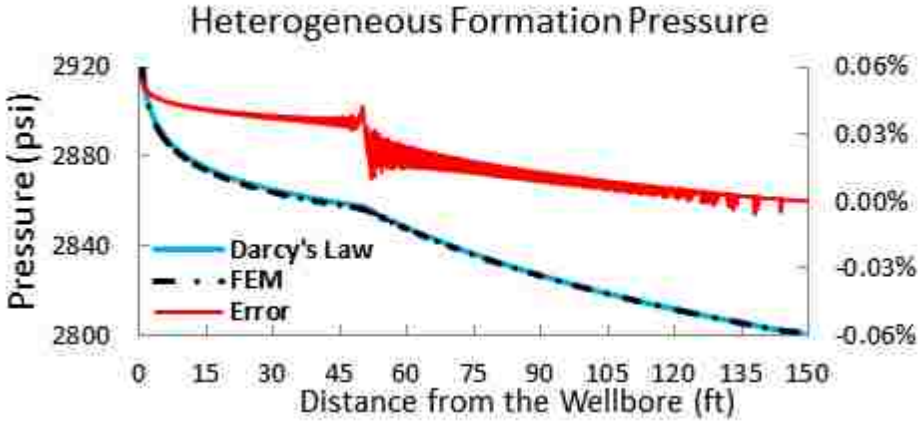

Figure 3-6. Pressure profile generated by the FEM solution and analytical Darcy solution for heterogeneous axisymmetric case. Percentage difference between both solutions on the right axis.

The graph above shows a very close prediction of formation pressure by the numerical solution of the diffusivity equation and Darcy's law, in order to get a better understanding of the pressure prediction obtained through both, the difference between solutions is plotted on the secondary axis. The error does not reach a value higher than 0.06% and it can be said that the solution is accurate enough for the requirements of this research.

Having tested the model for a homogeneous steady state case, it is then required to assure the proper dynamic response of the implementation. This is possible for a homogeneous reservoir for which the analytical solution given the assumptions of an infinite acting reservoir, constant flow rate, infinitesimally small wellbore and a reservoir initially at equilibrium is,

$$P(r,t) = P_i - \frac{Q\mu}{4\pi kh}\left[-E_i\left(-\frac{\phi\mu c_t r^2}{4kt}\right)\right] \quad \text{Eq.3-2}$$

In Eq.3-2, E_i is the exponential integral function,

$$E_i(x) = -\int_{-x}^{\infty} \frac{e^{-t}}{t} dt \qquad \text{Eq.3-3}$$

for which tabulated values can be found from multiple sources.

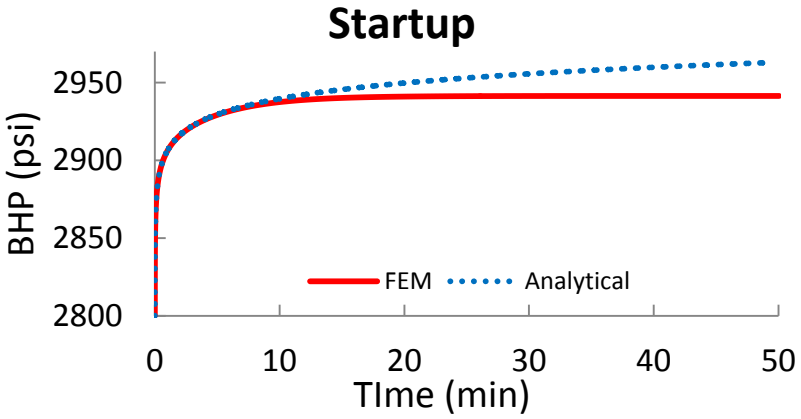

Figure 3-7. Simulated injection startup using FEM implementation of the diffusivity equation and analytical solution for homogeneous case.

Figure 3-7 contains the startup for both the FEM and analytical solutions. The difference only arises when the FEM reaches the boundary, point at which the infinite acting reservoir assumption on the analytical solution makes the BHP higher for it. The result is then useful in building confidence that the implementation of the diffusivity equation is accurate. If a big formation size in the MESH had been implemented, the solutions would stay close for longer.

3.3 Flowing Potential Validation in Three Dimensions on a Reservoir Geometry

Similar tests to those carried out in two dimensions can be extended to the three dimensional flowing potential when the density in Eq.2-33 is assumed constant. Another useful comparison can be performed by simulating a well startup for both two and three dimensions cases which proved to be useful not only in assessing the correct implementation of the model but also the accuracy of the relatively coarser MESH for three dimensions.

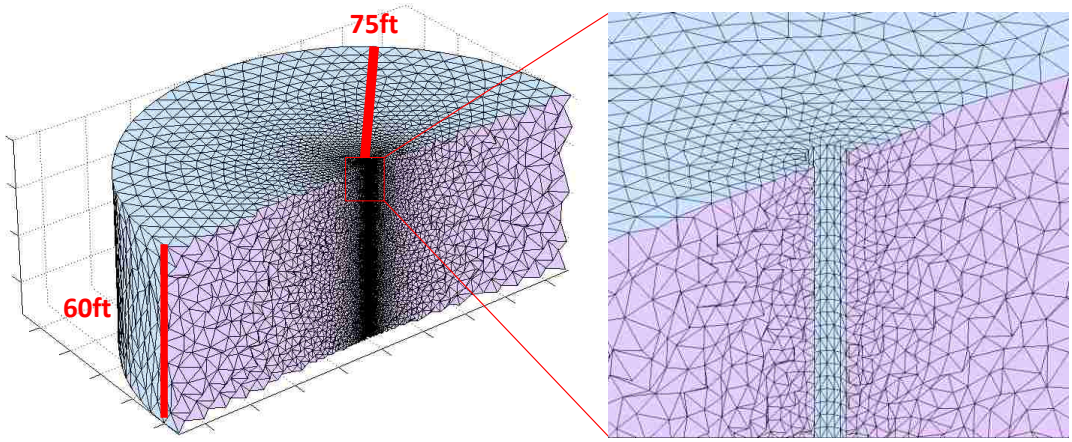

Figure 3-8. MESH for 3D FEM computation of pore pressure.

The volumetric spatial discretization for the system shown in Figure 3-8 has a radius of 75ft, a 60ft height and a 7'' wellbore. The formation radius is half of that in two dimensions in order to maintain small enough elements which provide accurate calculations while keeping the computational cost low enough for simulations to be carried out in rational timespans and avoid using high performance computing. Highly refined at the wellbore, the linear tetrahedron MESH has almost 120,000 nodes and well over 600,000 elements. Given the large size of the system, implementing the three dimensional solution to the boundary value problem in section 2.1.3 required additional optimization both in the implementation of the numerical method and the solution to it including parallelizing certain algorithms. The necessity for such improvement of the computational efficiency arises from the mesh size which varies considerably once the third dimension is added.

On this MESH, a simulation neglecting the dynamic term on the diffusivity equation in an axisymmetric but heterogeneous formation similar to that for two dimensions is executed, the pressure profile from the wellbore can be compared to the analytical solution of Darcy's Law in cylindrical coordinates. The formation is made heterogeneous through Eq.3-4 and other required properties as in Table 3-1.

$$\phi = \begin{cases} 0.25 \; r < 32ft \\ 0.20 \; r > 32ft \end{cases} \qquad \text{Eq.3-4}$$

Figure 3-9 shows a very close prediction of flowing potential by the numerical solution of the diffusivity equation and Darcy's law, in order to get a better understanding of the pressure prediction obtained through both, the difference between solutions is plotted on the secondary axis. The error does not reach a value higher than 0.25% and it can be said that the solution is accurate enough for the requirements of this research.

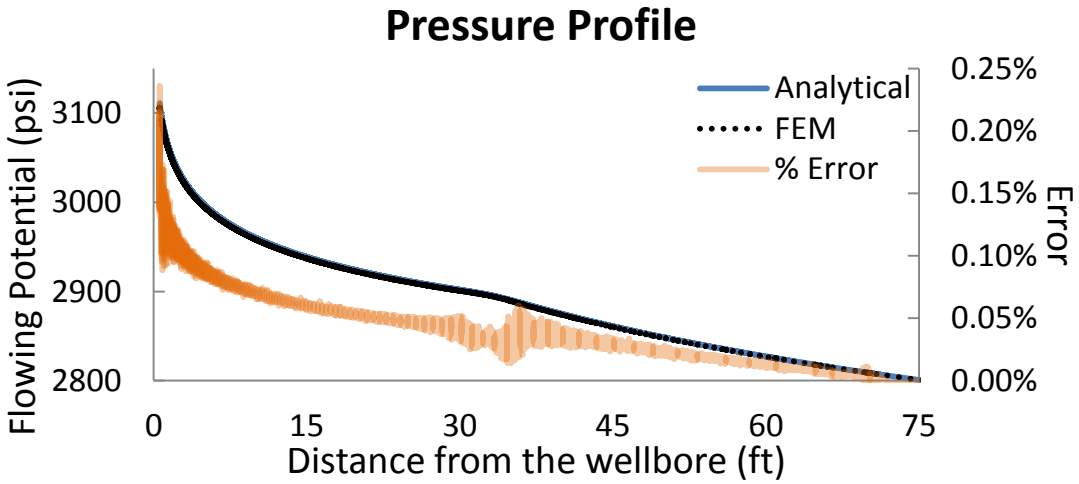

Figure 3-9. Heterogeneous implementation of the diffusivity equation in three dimensions.

Following the steady state test for accuracy, a dynamic comparison through a well startup for two and three dimensions is executed. The results should be exactly the same as all formation and fluid injection properties are the same. The bottomhole pressure readings for two and three dimensions for a well startup with no erosion are available in Figure 3-10. As expected, the downhole pressures as a function of time are almost the same differing by under 1psi for both systems throughout the entire 50 minutes period of injection.

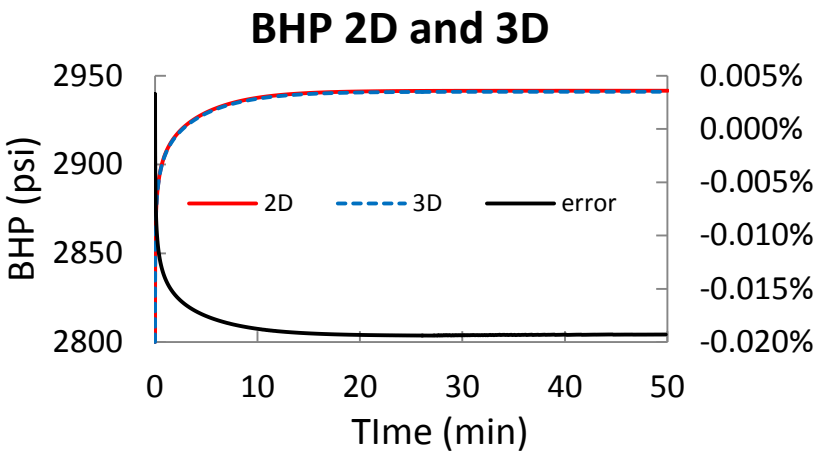

Figure 3-10. Well startup comparison between two and three dimensions FEM implementations.

Having extensively tested the numerical implementation of equations representing fluid flow at injection wells enables then the coupling of erosional phenomena on reservoir geometry for multiple spatial scales. The tests here prepared are an essential step towards the computation of formation sand transport within the reservoir which in general terms is the aim of this research.

CHAPTER 4: RESULTS OF TWO AND THREE DIMENSIONAL EROSION ON RESERVOIR GEOMETRY IMPLEMENTATION

4.1 Results on Heterogeneous Formations Using Static Fluid Flow Formulation

After extensively testing the channelization model solution through FEM on a square plate, the code was implemented on the geometry of interest (wellbore-reservoir) with induced heterogeneity. The system is made heterogeneous through a random normal porosity distribution with a mean value of 0.25 and a standard deviation of 0.1. A table containing relevant parameters for the base case simulation is available (Table 4-1). The parameters chosen combine field data, experimental results and some of the experience gather through the simulations described earlier.

Table 4-1. Relevant parameters for static base case simulation.

Parameter (symbol)	Value (units)
Injection Velocity (q)	1.063E-2 (ft/s)
Critical Stress Coefficient (C)	2
Erosion and Deposition Rate Coefficients	0.6
Total Simulation Time	20(s)
Time Step	0.01(s)
Formation Radius	1(ft)
Wellbore Radius	0.01778 (ft)

The simulation time corresponds to the timespan in which most of the relevant events take place in Huang et al. (2011) experiments. However, it is obvious that the realistic reservoir scale scenario should consider timespans of at least minutes. Multiple attempts to run the erosional model on higher timescales were unsuccessful. The main reason behind this situation is thought to be the assumption for the time derivative $\frac{\partial P}{\partial t} = 0$. A short time scale was also used by Mahadevan et al. (2012) and Ameen and Dahi Taleghani (2014). The time upscale was only successful when the dynamic term was given consideration as it will be demonstrated in sections to come. The erosion model parameters were derived from the simulations in the plate while matching the results of the authors who have previously implemented this model. These are believed to be valid as one of the authors calibrated its result with experimental observations. The fluid viscosity is simply that of water and the formation and wellbore radiuses are just a scale down of the reservoir geometry implemented for validation.

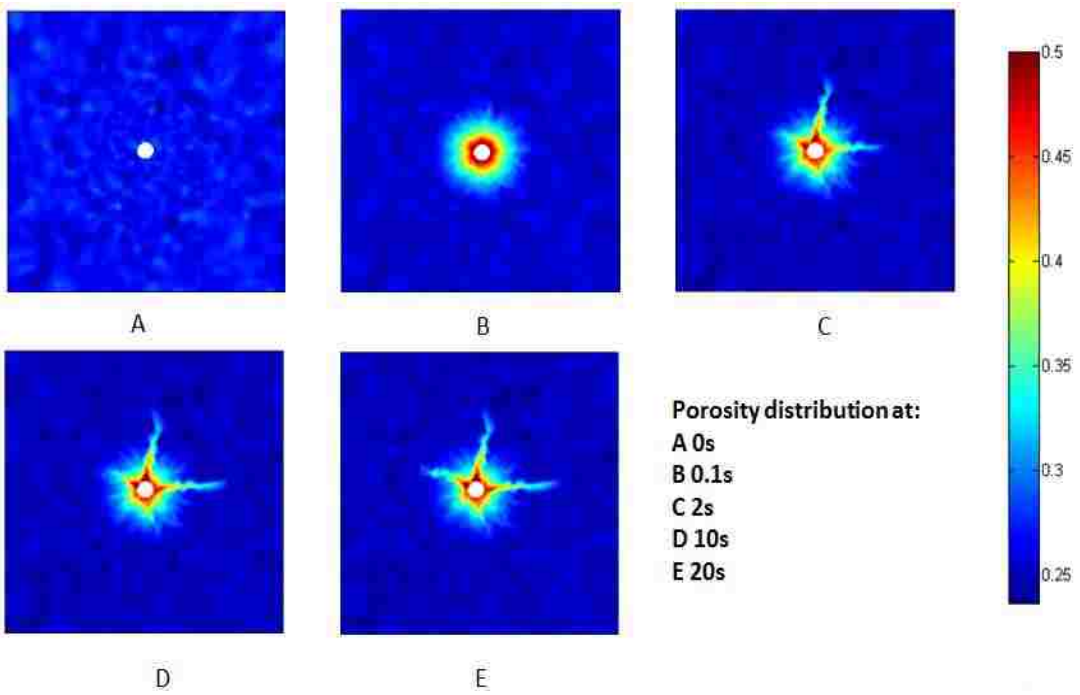

Figure 4-1. Porosity distribution after fluid injection into open-hole.

The results in Figure 4-1 show the porosity distribution around the wellbore after running the channelization model with the base case parameters. The images are a zoom-in to the wellbore in order to visualize the results more clearly before injection (A) and at 0.1s (B), 2s(C), 10s(D) and 20s(E). Initially, the formation has a random normal heterogeneous porosity distribution, after 0.1s of injection, a ring of eroded sand forms around the wellbore with porosity increasing with proximity to the wellbore. After 2 seconds of injection, a change in the erosion pattern becomes visible when two distinctive channels form. The channels seem to elongate after injection has been going on for ten seconds and at the final point (20s), the growth of a third channel to the left of the wellbore can be seen.

4.1.1 High injection rate

In order to investigate the effect of higher injection rates, the fluid velocity at the sandface was increased by an order of three using the same initial porosity distribution (Figure 4-2). Again a ring of high porosity forms around wellbore after 0.1 seconds but a set of multiple channels is visible after 2 seconds. After 10 seconds only 2 of the channels seem to be growing with porosity increasing within them closer to the wellbore. When the simulation reaches 20 seconds the channels show little change but

have increasingly higher porosities. The channels formed are measured to be around 5 times longer than those in Figure 4-1 demonstrating the significant impact of the injection rate on the physical integrity of the wellbore surroundings during fluid injection.

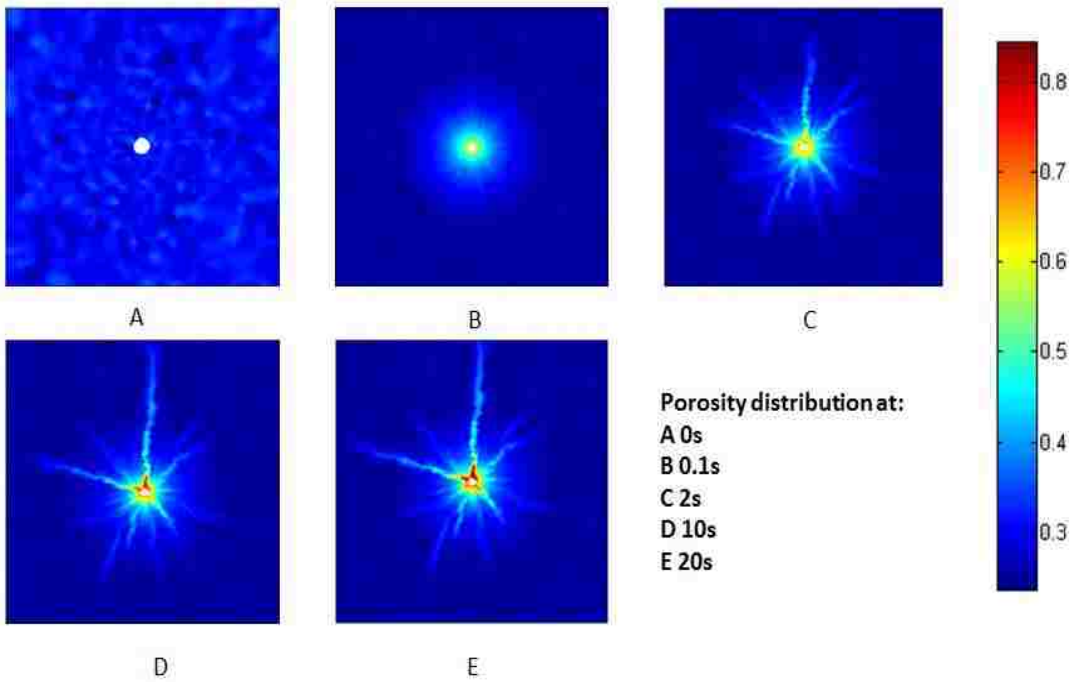

Figure 4-2. Porosity distribution after fluid injection into open-hole with three times the injection velocity of the base case.

The initial (left) and final (right) pressure distributions for the high injection rate are shown in Figure 4-3. Initially the pressure gradient close to the wellbore is high but as the vicinity of the wellbore is eroded, it dramatically diminishes. Also, the pressure distribution goes from almost radial to asymmetric as the channels provide lower resistance paths for fluid to flow through. The locations with high erosion can be clearly seen in the pressure profile and should shed some light on where injected fluid is most likely going.

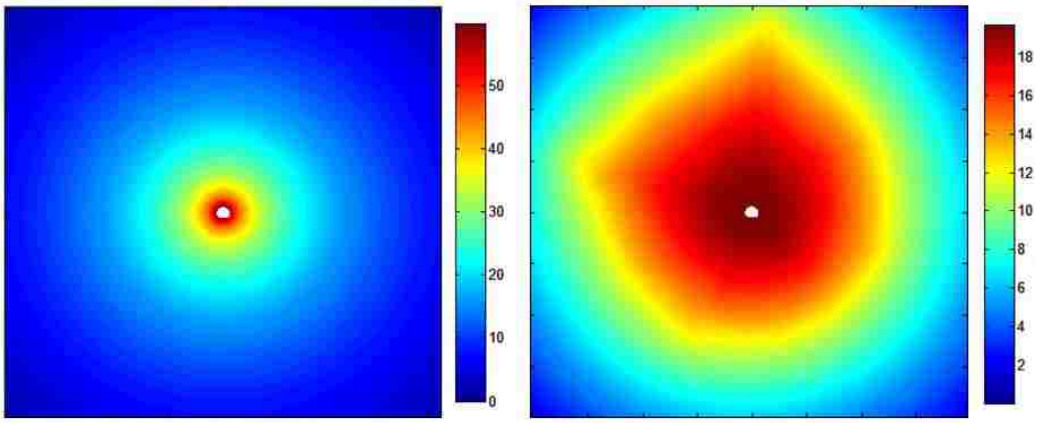

Figure 4-3. Pressure distribution after fluid injection into open-hole with three times the injection velocity of the base case.

The flowrate can be said to have a significant effect on the channels formed. Not only channels are longer but also significantly more porous reaching values of up to 90%. The flowrate is then proven to have a severe impact on the erosional phenomena and should be carefully managed to avoid severe formation damage.

4.1.2 Effect of completions

After performing the previous simulations, the effect of different completions were given consideration. An open-hole gravel-pack and a frac-pack which are the most common completions observed in wells targeting poorly consolidated formations were used. The main change in the completed zone around the wellbore for either one is the proppant size, which is usually six times that of the formation mean particle sand, concept that is also graphically displayed in Figure 3-5. The proppant size increases the permeability 36 times that of the formation when the remaining parameters are kept the same. The gravel pack used reaches 1ft into the formation and it is scaled down to the smaller system described in Table 4-1 (Figure 4-4 left).

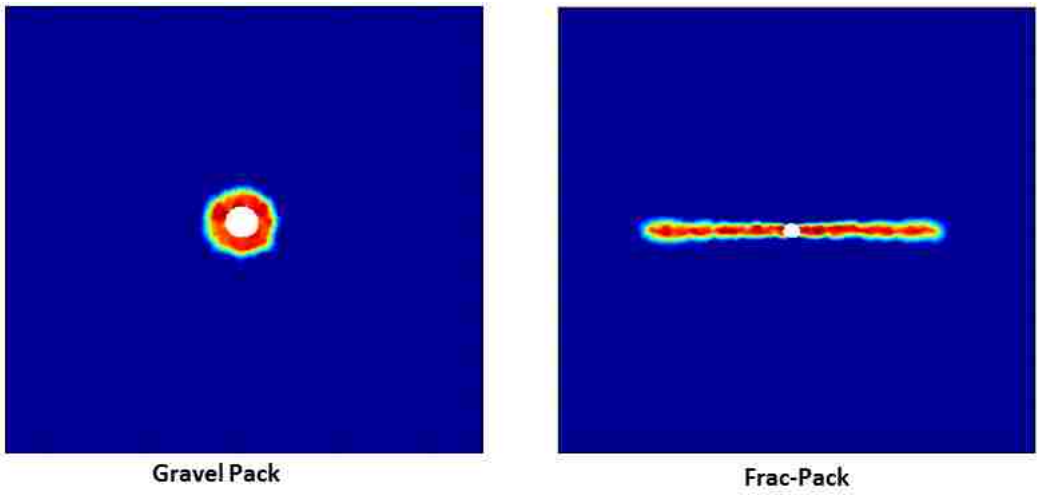

Figure 4-4. Gravel (left) and frac-pack (right) completions geometries for simulations.

A frac-pack with a half fracture length of 10ft is chosen (Figure 4-4 right). For the frac-pack injection only occurs at the perforations which are assumed to be continuous from top to bottom of the well and are at the fracture wellbore interphase.

First, a run with the base case parameters and a gravel-pack is performed with the resulting porosity distribution shown along with the wellbore pressure ratio (Figure 4-5). The wellbore pressure ratio is defined as that between the wellbore pressure at any moment to the initial (before erosion) pressure. The results for the gravel-pack show that this is not eroded and decreases the overall significance of the pressure drop generated by erosion meaning a more stable wellbore. However, the sand matrix beyond the completions is still eroded and voids that could eventually absorb the proppants are created. A similar but more critical situation takes place when injecting at three times the initial injection velocity (Figure 4-6). Multiple channels with porosities beyond 75% grow after the gravel-pack and extend as much as those of the open-hole scenario. The pressure behavior also shows the difference between the completed case and the open-hole closer together compared to those in Figure 4-5, this shows that at higher injection rates this completions method is less efficient.

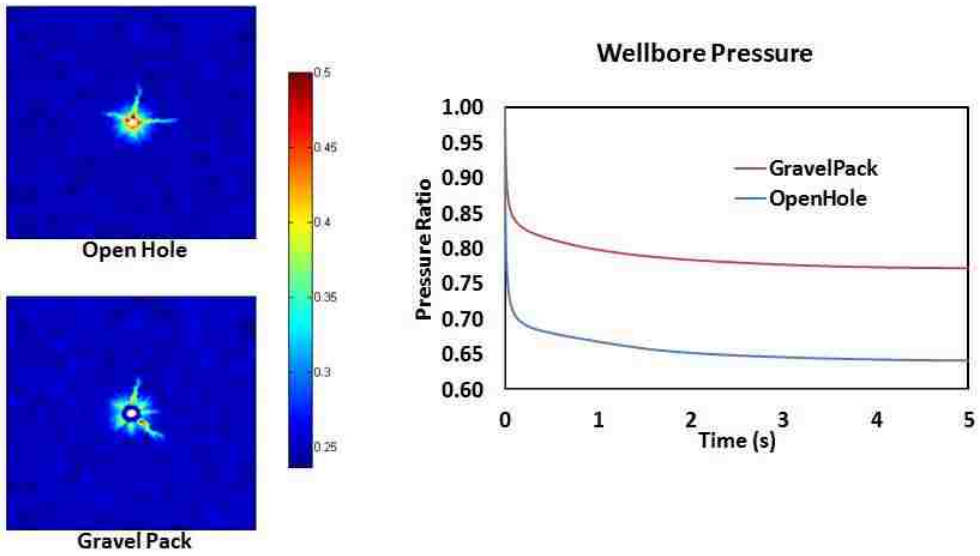

Figure 4-5. Formation channelization in open-hole and gravel-packed wellbores and relative pressure variations.

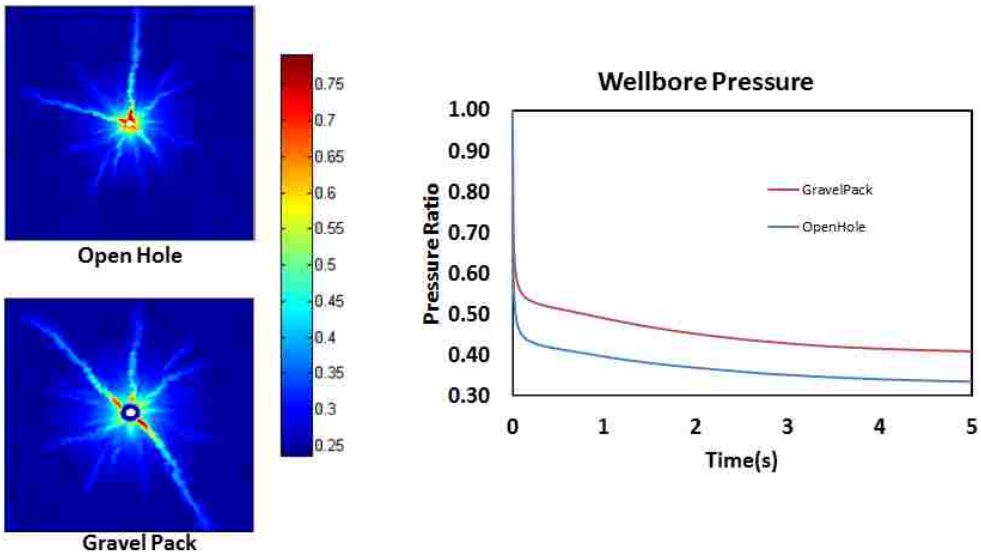

Figure 4-6. Formation channelization in open-hole and gravel-packed wellbores and relative pressure variations at high injection rates.

The high injection rate case was run for the frac-pack which resulted in a rather odd final porosity distribution (Figure 4-7 right). Channels grew perpendicular to the orientation of the frac-packs and some erosion is also evident at the fracture tips. It does not seem possible for the channels and frac-packs to extend in different directions especially when both might be created through similar mechanisms.

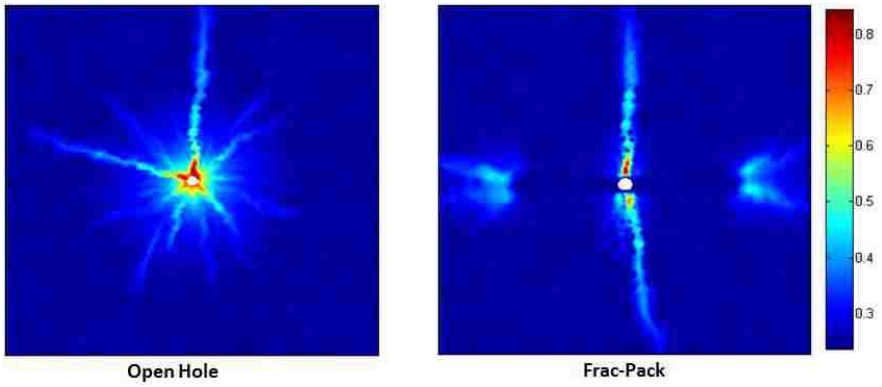

Figure 4-7. Formation channelization in open-hole and frac-packed wellbores and relative pressure variations at high injection rates.

Fractures are known to grow perpendicular to minimum horizontal stresses making anisotropy a decisive factor in their initiation and growth orientation. Here we are not dealing with fractures and the model does not consider formation stresses (at least not explicitly). However, stresses do have an effect on permeability anisotropy which is a decisive parameter within the channelization model. The grains are arranged in specific patterns depending on the formation stress state which may result in higher tortuosity in a particular direction, this lead to simulate a case in which permeability is 20% percent higher in the y-axis which seems a proper representation of formation conditions.

Results for porosity distribution around the wellbore when anisotropy is induced to the system in the presence of a frac-pack are presented in Figure 4-8, along with it is the resulting relative wellbore pressure. The effect of anisotropy is clear as the erosion in the direction perpendicular to the frac-pack is almost non-existent. The presence of voids with up to 50% porosity at the frac-pack tips could eventually be filled with the proppants recreating the situation described in Figure 1-2.

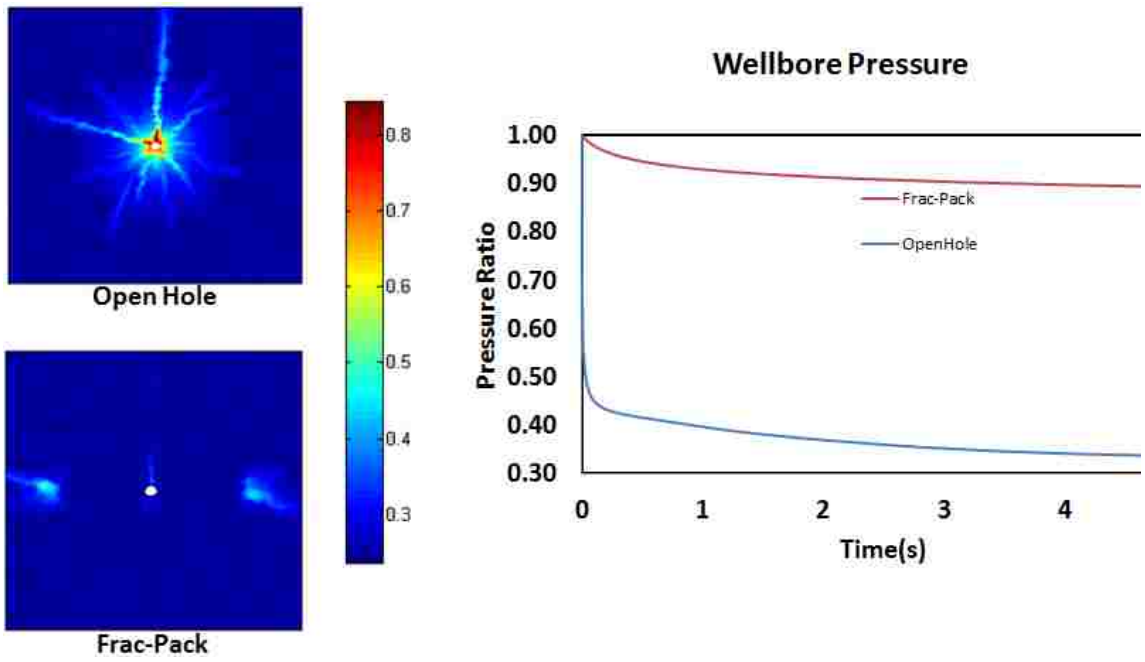

Figure 4-8. Formation channelization in open-hole and frac-pack wellbores and relative pressure variations at high injection rates (Induced anisotropy).

4.2 Results on Heterogeneous Formations Using Dynamic Fluid Flow Formulation

This section presents the results obtained when the diffusivity equation including the transient term is implemented, the main difference and achievement of incorporating this term was obtaining results for field scale reservoirs in proper simulated times of up to an hour. The results of the model implementation and its dependence on different parameters such as flow rate, formation heterogeneity, initial average porosity, fluid viscosity and stress distribution are here shown. The dynamic implementation also allows the use of well-known transient analysis tests presented towards the end of the section.

Similar to the base case in section 4.1, first the simulation on a standard scenario is shown followed by the analysis of the impact of different variables. The erosional model parameters are the main difference relevant to this section as this had to be modified to meet the new time scale implemented.

Table 4-2. Relevant parameters for dynamic channelization.

Parameter (symbol)	Value (units)
Time step (Δt)	0.1 (s)

Table 4.2 (continued)

Simulation time (t)	25(min)
Erosion and deposition rate coefficients (k_e and k_d)	1.0 E-3
Characteristic velocity to hydraulic conductivity ratio (γ)	6.0 E04
Critical stress coefficient (C)	2
Deposition threshold (ϕ_s^*)	0.15

The parameters in tables Table 3-1 and Table 4-2 make up for the base case scenario. The resulting porosity distribution for this scenario at multiple times during the simulation is available in Figure 4-9 (A) before injection after (B) 1min, (C) 3min, (D) 8min, (E) 18min and (F) 25min. The images presented are a zoom-in into the reservoir 20x20ft in size. Note that the results until 8min are very similar to those in Figure 4-2. After this point, channels only elongate and no significant changes seem to take place between 18 and 25 minutes indicating that the erosion process might have stabilized. The formation damage for this case has extended to around 3ft from the wellbore mostly radially. The porosity distribution represents the weak heterogeneities in the rock strength (σ) as well as the grain size distribution.

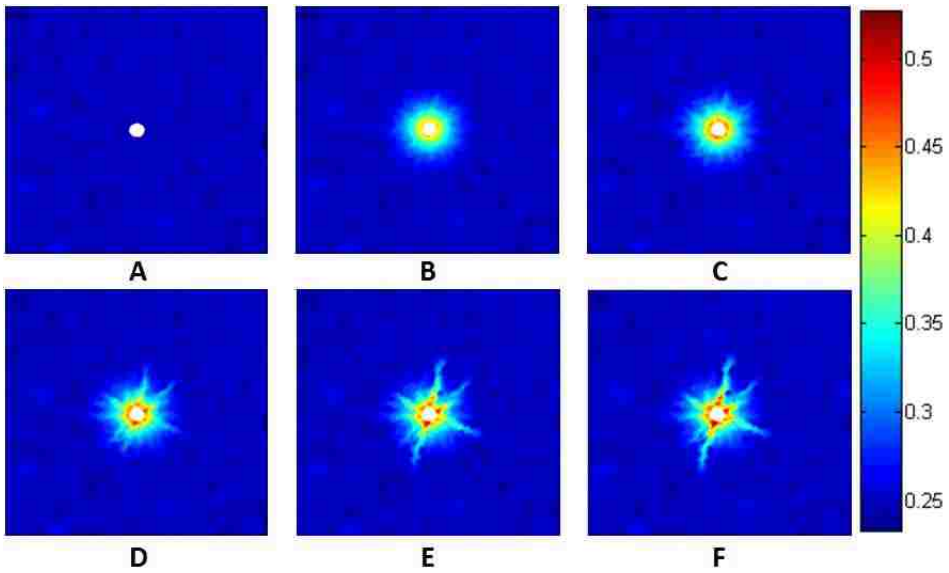

Figure 4-9. Porosity distribution after fluid injection into open-hole. at A) 0min, B) 1min, C) 3min, D) 8min, E) 18min and F) 25min

Erosion occurs when the flowing fluid drag force on the porous media is enough to break the bonding material between grains. Therefore, if a formation is assumed to be heterogeneous, there will be specific regions for channel initiation and growth instead of having the whole medium fluidized. Eventually and towards the end of the transient state, channels stop expanding as long as the injection rate

is kept constant. By the time steady state is reached, the initial pressure distribution around the wellbore has varied significantly.

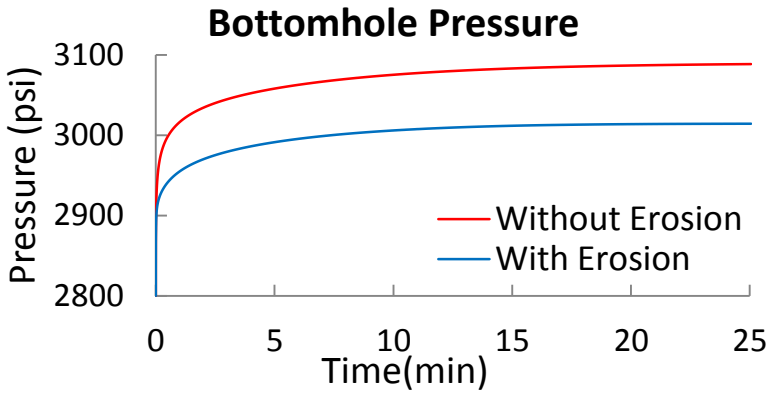

Figure 4-10. Wellbore pressure as obtained with and without channelization and dynamic fluid flow.

The effect of formation damage on the wellbore pressure is displayed in Figure 4-10. Unlike the static simulation in which the initial pressure is that of the steady state undamaged formation, the cases here recreate the pressure curves that are observed during a well startup. The pressure when there is channelization (red) and in the absence of this (blue) are plotted to allow comparison between both situations. The pressure in the presence of channelization shows an initial increment in pressure as flow develops, however, it is lower in magnitude than that of the undamaged formation as a result of erosion and transport of sediment away from the wellbore. The pressure behavior in Figure 4-10 poses a big challenge in identifying this phenomenon during an injector's startup as no abnormal trends in the curve are apparent. The observed BHP behavior observed is in line with experimental observations in Figure 1-4.

4.2.1 High injection rate

Just as in section 4.1.1, the fluid velocity at the sandface is here increased by an order of three. Recall that the fluid capacity to erode the matrix is dependent on the pressure gradient, because the gradient will fall with distance from the wellbore, at certain distance from it, the pressure gradient is not enough to erode grains. As the fluid injection rate is increased, so is the pressure gradient hence the

maximum distance from the wellbore at which grains can be eroded is expected to be further away from the well.

The results in Figure 4-11, a 40x40ft zoom-in around the wellbore again show a ring of high porosity forming around the wellbore after 1 minute, however, a set of multiple channels is visible after 3 minutes which after 8 minutes have expanded further than those in Figure 4-9F. After 18 minutes, most of the channels seem to be expanding mainly upwards. This situation is probably caused by the random formation heterogeneity that enhances channel growth in certain directions.

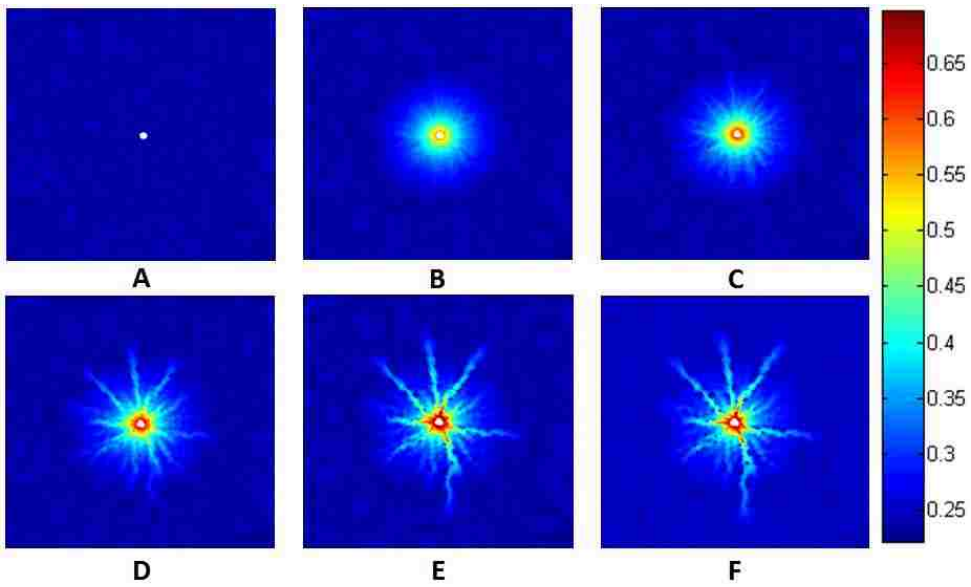

Figure 4-11. Porosity distribution after fluid injection into open-hole at high injection rate. A) 0min, B) 1min, C) 3min, D) 8min, E) 18min and F) 25min.

The pressure contours for the porosity distributions at high injection rate are shown in Figure 4-12. Because the flow is developing as the matrix is being eroded, it is hard to distinguish the effects of channelization on the pressure contour from the transient fluid flow and it is only in the final two contours that non-radial features of flow become apparent. The contours show an initially at equilibrium formation which pressure begins to increase as fluid is injected. The effects of erosion in these contours becomes clear after 18 minutes in which the first high pressure contour extends far from the wellbore evidencing the low pressure losses, this means there must be an area of high permeability/porosity close to the wellbore.

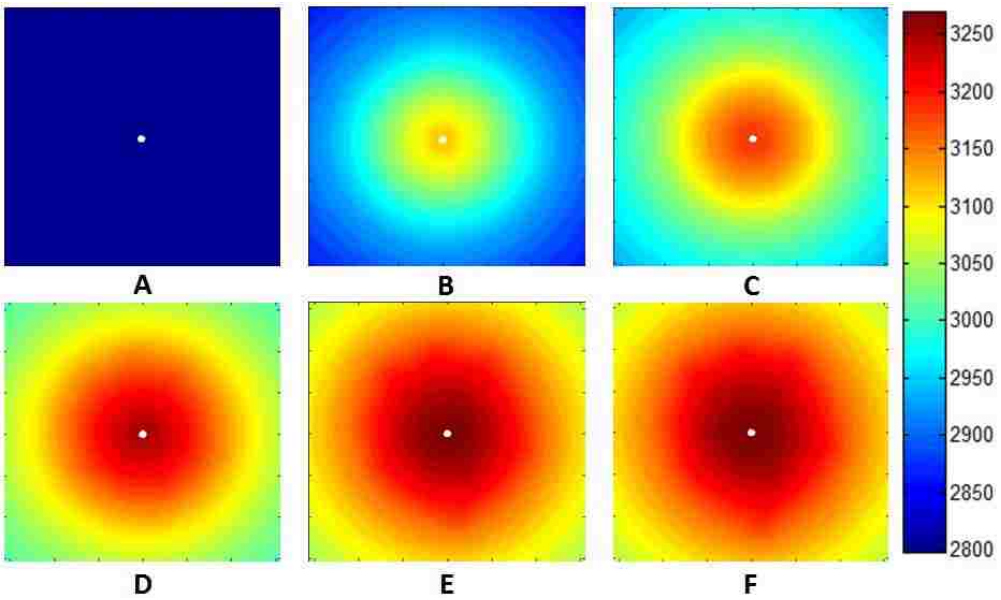

Figure 4-12. Pressure contours after fluid injection into open-hole at high injection rate.

After 25 minutes the pressure contours dilute as the damage increases having lower losses in the vicinity of the well. Although the channelization patterns are not symmetric with respect to the wellbore, the pressure contours are fairly round showing that not too far from the wellbore, the flooding pattern is pretty much ring shaped.

4.2.2 Failure threshold

In this section the effect of the failure coefficient (C) is studied, the critical stress (σ) that opposes the normalized pressure gradient in Eq.2-71 will vary significantly. The effect of three different failure coefficients on σ is shown by Ameen and Dahi Taleghani (2014), where different failure coefficients are plotted against the average volumetric fraction of the solid matrix ($\overline{\phi_s}$). A higher failure coefficient increases the resistance to failure of the matrix reducing the damaged zone achievable at determined conditions.

The final porosity based on erosion failure coefficients (C) of 0.5 and 2 is available in Figure 4-13. For a weaker rock ($C = 0.5$) many more channels with higher porosities are formed. On the other hand, an erosion threshold of 2 leads to fewer, shorter channels with porosities between 0.4 and 0.5. It is

interesting that although the initial formation had the same porosity heterogeneity, the weak spots through which channels developed are different.

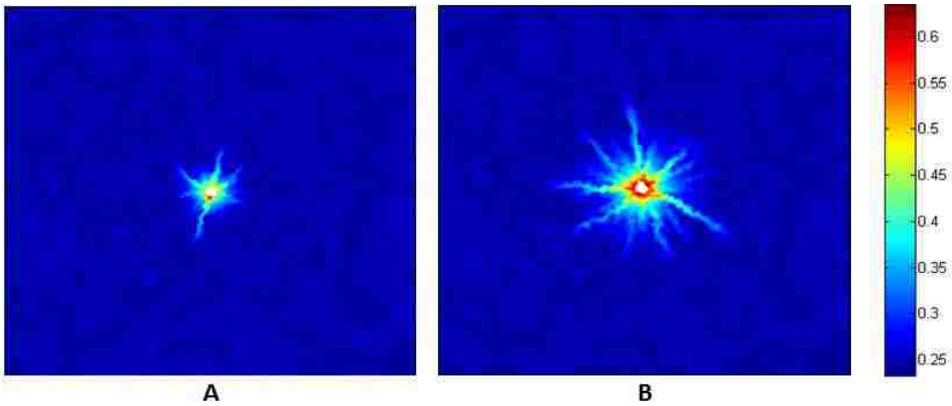

Figure 4-13. Final porosity distribution for different failure stress coefficients A) $C = 2$ B) $C = 0.5$.

In Figure 4-14 the change of bottom-hole pressures for failure stress coefficients of 0.5 and 2 are plotted. The lower stress coefficient ($C = 0.5$) has a higher pressure detriment as more damage is being caused by fluid injection, the result is expected as the lower threshold coefficient makes the rock less resistant to the fluid drag forces.

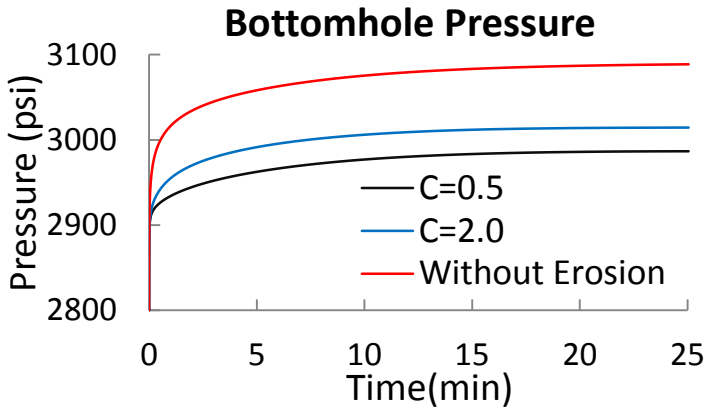

Figure 4-14. Effect of failure stress coefficient C on BHP. C = 0.5 (gray), (B) C = 2 (blue).

Similar field situations in which injectivity seems to increase short after startup are reported in the literature which could be explained by this phenomena at least in the case of very weak formations (Svendson et al., 1991).

4.2.3 Formation heterogeneity

Another parameter that can affect the way in which formation damaged is imposed during injection is the initial porosity distribution. Figure 4-15 has the final porosity distribution after injection into formations with initial porosity standard deviations of 0.001, 0.01 and 0.03. For the case with a lower heterogeneity (Figure 4-15A), the results show a more evenly distributed ring of high porosity (0.45-0.50) around the wellbore when compared to the other two cases in which the higher porosities mainly appear in the direction in which channels are developed. Aside from the difference just outlined, the erosion trends seem to be the similar showing little impact of the magnitude of the heterogeneity induced in the erosion patterns.

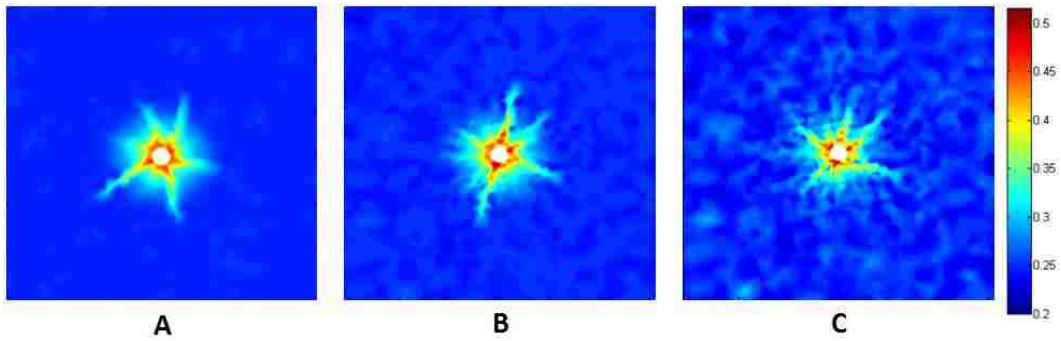

Figure 4-15. Final porosity distribution for different heterogeneities A) $SD = 0.001$, B) $SD = 0.01$, and C) $SD = 0.03$

The wellbore pressures for the three cases (Figure 4-16) show a similar trend having the three pressure curves very close to each other. This situation makes it very hard to obtain any information on how heterogeneous a formation is from injection pressure readings in the presence of erosion. However, this result shows that assumptions of homogeneity do not affect the pressure reading significantly which will be used later to derive a method to obtain simulation parameters from injection tests.

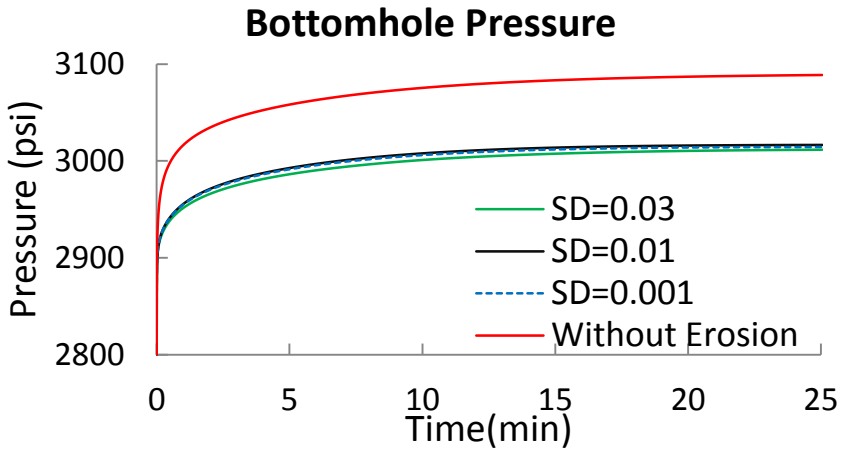

Figure 4-16. Formation channelization pressure variations with dynamic fluid flow modelling with initial formation porosity standard deviation of 0.03, 0.01 and 0.001.

4.2.4 Viscosity of the injected fluid

This section explores the impact of fluid viscosity on formation damage. Higher viscosity fluids are used in EOR operations to obtain more favorable mobility ratios. In completions operations or stimulation treatments, higher viscosity fluids are intended to obtain wider fractures as well as to increase the gravel carrying capacity of the fluid among other things. Being this a common practice makes it relevant to study its impact on channelization.

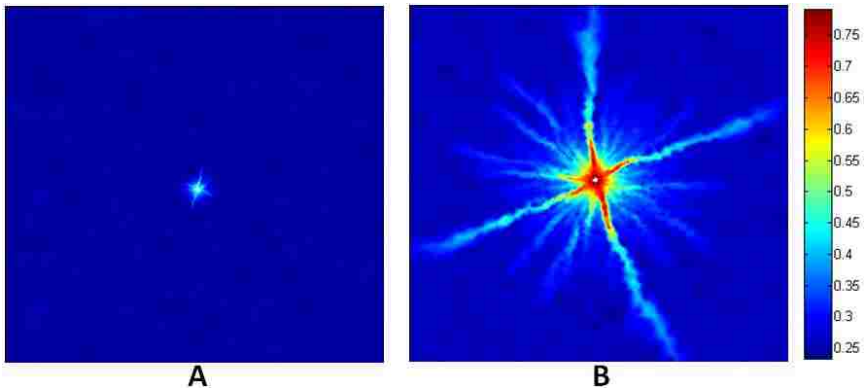

Figure 4-17. Porosity distribution after injection of fluids with 1cP and 10cP showing significantly higher erosion for high viscosity fluids

The final porosity distributions after injecting fluids with viscosities of 1cP (left) and 10cP (right) are available in Figure 4-17. Interestingly, no other parameter presented until now has shown such high impact on channelization as that of fluid viscosity. The images, which are an 80x80ft zoom-in around the

wellbore show that for the high viscosity case, multiple channels extend as much as 40ft from the wellbore. On the channel sides (walls), areas of low porosity increase the permeability contrast between the channels and their surroundings forcing more fluid to remain in the channel. The importance of this result is that it is useful in explaining two field observations; the first one is the fact that often times stimulation treatments above fracture pressure seem to have no effect on well performance, after failed attempts, injection of higher viscosity fluids completely solve the problem, such are the cases reported by Webb et al. (2009) in the Kikeh field offshore Malaysia and that of Pedroso et al. (2009) in the Campos Basin offshore Brazil. On the other hand, wells suffering from sanding seem to be less prone to this phenomenon when the fluid being injected has a higher viscosity. After looking at the erosional effects of high viscosity fluids this is not a surprising fact as the area close to the wellbore seems to be completely cleared of particles that could flow towards the wellbore over shut-in periods.

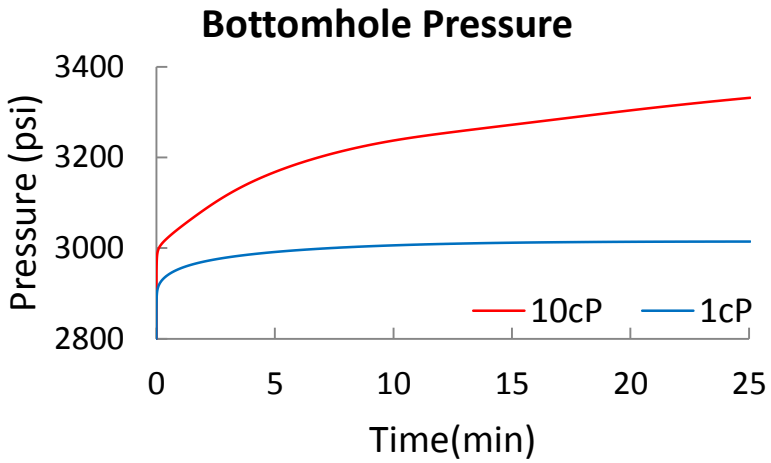

Figure 4-18. Formation channelization in open-hole and frac-pack wellbores and relative pressure variations at high injection rates (Induced anisotropy). of fluid viscosity on BHP.

Figure 4-18 has the pressure readings for both cases discussed in this section. The curve for the 10cP fluid (blue) shows a wellbore pressure far from stabilizing after 25min. The higher pressures reached also entail the damaging capacity of the higher viscosity fluid which will create larger drag forces on the particles to be loosened.

4.2.5 Effect of completions

This section uses the same completions as those in Figure 4-4, the only difference being the consideration of a longer much more realistic frac-pack with a 20ft half fracture length. First, a run with the base case parameters at high injection rate and a gravel-pack is performed with the resulting porosity shown in Figure 4-19.

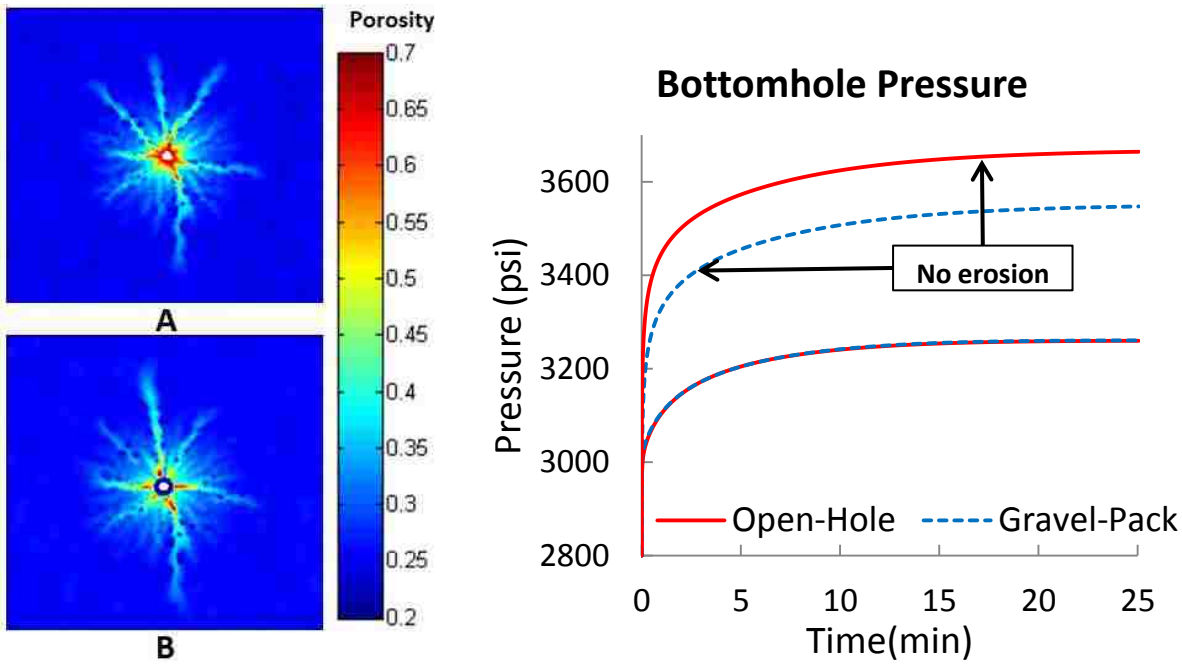

Figure 4-19. Formation channelization in open-hole and gravel-packed wellbores and pressure variations with dynamic fluid flow model.

The results for the gravel-pack show that this is not eroded meaning that the hydraulic conductivity decreases the fluid drag forces below the point of erosion. Outside the completions, the erosion has a very similar pattern to the open-hole case except for some channels that extend even further away from the wellbore. It is important to note that again voids that could eventually absorb the proppants are created.

The wellbore pressure shown to the right contain the readings with and without erosion for both completions. As expected, the gravel pack in the absence of erosion shows lower pressure readings than the open-hole, however, upon channelization, pressure readings are actually similar. This observation can

be explained by the fact that close to the wellbore both systems have a ring of high permeability represented by the highly eroded area for the open-hole and by the completions sand in the gravel-pack.

The high injection rate case was run for the frac-pack having anisotropy implemented right away so that no channels extend perpendicular to the frac-pack. The maximum to minimum permeability anisotropy ratio, which is a decisive parameter within the channelization model has been shown take values of up to 5 (Bandiziol & Massonnat, 1992). Horizontal permeability anisotropy is common in certain depositional environments even in the absence of naturally occurring fractures, among such environments are river channel depositional systems and cross-bedded sands (Ehlig-Economides et al. 1990).

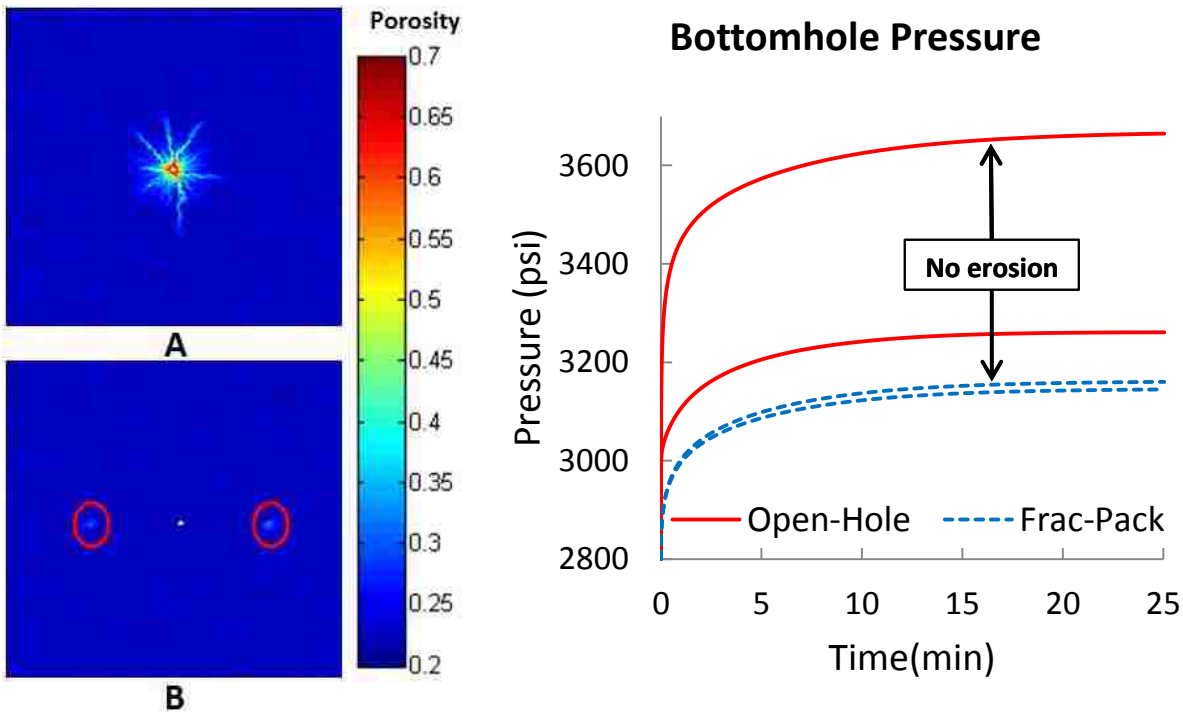

Figure 4-20. Formation channelization in open-hole and frac-pack wellbores and relative pressure variations at high injection (Induced anisotropy).

Results for porosity distribution around the wellbore when anisotropy is considered in the system in the presence of a frac-pack are presented in Figure 4-20, along with it is the resulting wellbore pressure. The effect of anisotropy is clear as there is no erosion in the direction perpendicular to the frac-pack. The presence of voids with up to 40% porosity at the frac-pack tips could eventually be filled with the gravel

recreating the loss of completions observed in the field. Note that the erosion in this case is lower to the static case probably because of the longer frac-pack. Although some alterations of the formation are evidenced even in the presence of a frac-pack, a significant improvement is achieved. Proof of the stabilization provided by the frac-pack are the close pressure readings between the two red curves representing a frac-packed formation in the presence and absence of erosion. The erosion is occurring at the frac-pack tip which is 20ft away from the wellbore. The only simulation in which erosion 20ft from the well was achieved was the 10cP fluid case.

Figure 4-21 contains the fluid velocity map around the wellbore and encloses in a box the area occupied by the frac-pack. It can be seen that the fluid velocity throughout the frac-pack is higher compared to the rest of the formation; this is expected as it is the path of less resistance making the fluid more likely to flow through it.

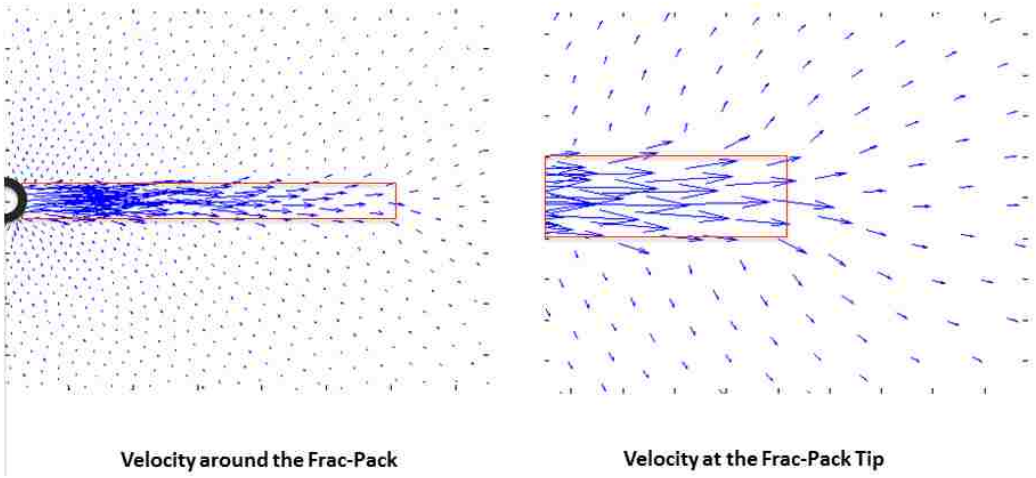

Figure 4-21. Fluid velocity within a frac-pack and around it (left) and at the frac-pack tip (right).

The problem having most of the fluid flowing through the frac-pack arises at the tip where there is a high permeability contrast between the formation and the frac-pack and the fluid hits an interface with much higher resistance to flow. The high fluid velocity at the tip creates a high pressure gradient zone far from the wellbore leading to erosion. This is a relevant result that could be hardly explained by other physical mechanisms and that has been observed in the field.

4.3 Model Calibration and Erosion effects on Well Testing

To implement this methodology for field application, it is important to somehow obtain the erosion parameters. Four parameters that must be estimated are identified. The characteristic fluid velocity to hydraulic conductivity ratio (γ) and the critical stress coefficient (C) can be thought of as time independent parameters while the erosion (k_e) and deposition (k_d) coefficients determine how fast the steady state is achieved. From, Eq.2-71, it can be seen that regardless of time, erosion will only stop when,

$$(\phi)^{\frac{3}{2}}(\gamma^{-1}\nabla p)^2 - \sigma \leq 0. \qquad \text{Eq.4-1}$$

For a point in the system where there is erosion, assuming the system is initially homogeneous, and neglecting deposition, from the above equation it comes that,

$$\frac{1}{C}\left(\frac{q\mu}{\gamma}\right)^2 = k(\phi)^2 \left(\tanh\left(2\pi\left(\left(1-\phi_{eq}(r)\right)-0.6\right)\right)+1\right)\left(\phi_{eq}(r)\right)^{-\frac{3}{2}}. \qquad \text{Eq.4-2}$$

In Eq.4-2 q is the flux or quotient of the flowrate and the area open to flow in feet per second and ϕ_{eq} is the equivalent porosity which shall not exceed 90% at the sand face. The result allows obtaining the porosity reached after the system stabilizes as a function of the distance from the wellbore that in some cases provides enough information to estimate the difference between steady state pressure in an eroded formation and the intact one. Having these, it is then possible to plot the value of the left hand side in Eq.4-2 as a function of the difference of steady state pressure between eroded and non-eroded systems. Figure 4-22 shows this plot for multiple original formations permeabilities.

Figure 4-22. Erosion model parameters as a function of pressure difference between eroded and non-eroded systems.

When an injection test is performed and allowed to stabilize, Figure 4-22 can be used to obtain the ratio of simulation parameters γ and C. Using the bottomhole pressures difference obtained for the base and the high injection rate cases with the viscosity in centipoise, the following results are obtained.

Table 4-3. Parameter estimation from characteristic lines in Figure 4-22 using pressure difference caused by erosion for base and high injection rate cases.

Case	Δp from simulation	Variable $(q\mu/\gamma)^2/C$ from chart	Calculated $(q\mu/\gamma)^2/C$
Base	74psi	1.7E-14	1.57E-14
High Injection Rate	410psi	N/A	1.41E-13

For the base case the difference between the calculated parameter and that from the chart is relatively small hence it represents good estimate of the model parameters. The close match between the simulation parameters and those used in the simulation can be explained by the fact that most of the erosion during the low injection rate simulation occurs in the form of a ring. The case for the high injection rate however entails channelization. The pressure difference between the eroded and intact formation of 408psi lies beyond the maximum achieved in the chart of Figure 4-22. The cause for this behavior lies on the assumption made to build the chart in which erosion is only a function of the distance from the wellbore while heterogeneity plays a big role in generating channels (Figure 4-11). This situation outlines the

importance of erosional models accounting for formation heterogeneities unlike some models that propose ring-shape erosion (Gravanis et al., 2015). Also, the chart then becomes useful in identifying cases in which there is channelization.

It becomes clear that the chart must be used carefully controlling the injection velocity at the sand face so that the erosional parameters relation can be obtained. For instance if a step rate test is run on an openhole prepacked screen, the lower injection rates can be used to obtain the set of variables $(q\mu/\gamma)^2/C$ while the higher injection rates may be useful in assuring the variables as read from the chart are appropriate. The test analysis procedure would consist of first trying to estimate the parameters C and γ from the low injection rates and then trying to pressure match the steady state pressures for higher injection rates using the model proposed here. Finally, parameters k_e and k_d could be found while trying to match the transient behavior between stabilization of bottomhole pressures for different injection rates.

4.3.1 Step rate, drawdown and Nolte G-function

A final simulation with an incremental injection rate similar to a step rate test is performed, injection linearly increases with time over a ten minute period from 0 to 15,000bbl/d. After the "step rate" injection, another simulation is performed injecting for 25 minutes at 2000, 6000 and 18,000bbl/d, then, the well is shut-in ($Q = 0$bpd) in order to capture the falloff behavior of the damaged formation.

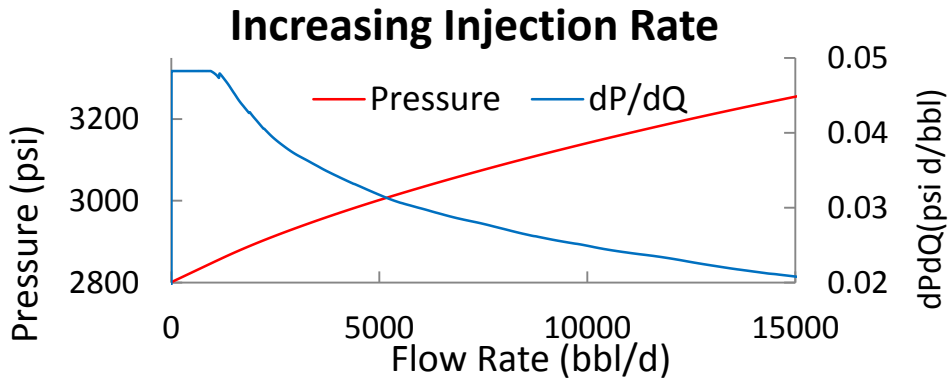

Figure 4-23. Bottomhole pressure during step rate injection.

The resulting wellbore pressure for the "step rate" injection is available in Figure 4-23. The relation between the pressure and the injection rate appears to be almost linear or with slowly decreasing slop. Making a distinction of when erosion starts from the pressure is rather complicated. A look at the pressure

derivative with respect to the injection rate clearly shows a trend change at around 1,000bbl/d. The derivative deeps downwards when erosion begins making it a good test to detect this phenomenon at punctual operation conditions.

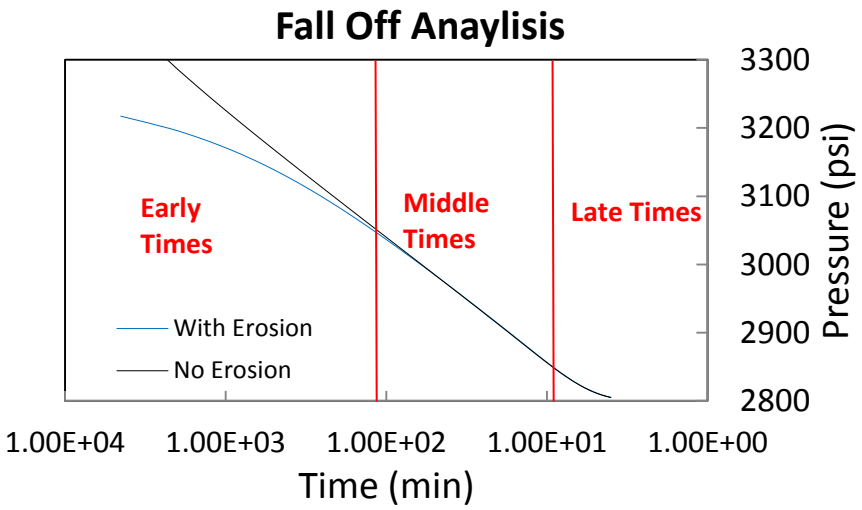

Figure 4-24. Fall off test pressure reading simulated after injector shut-in for unaltered and eroded formations.

The step rate simulation was followed by a well shut-in leading to a falloff test. The pressure reading is presented as a function of the Horner time $((t_p + \Delta t)/\Delta t)$ in logarithmic scale. In order to analyze the resulting pressure, the basic procedure as established by Lee (1982) for buildup tests is implemented. The author divides the Horner plot into early, middle and late times as displayed on Figure 4-24. The early times results in a linear plot for the unaltered formation since no damage has been caused unlike the curve for the eroded case. The middle region, which results in a linear trend on the semilog plot, corresponds to the point at which the radius of investigation has moved beyond the damaged zone. From this region, the permeability and skin can be calculated as,

$$k = 162.6\frac{Q\mu}{mh} \quad \text{and} \quad s = 1.151\left[\frac{P_{ws} - P_{wf}}{m} - \log\left(\frac{\Delta t\, k}{\phi\mu c_t r_w^2}\right) + \log\left(\frac{t_p + \Delta t}{t_p}\right)\right], \qquad \text{Eq.4-3}$$

where m is the slope in that linear region, P_{ws} is the pressure after shut-in and P_{wf} is the wellbore flowing pressure right before flow stops. The slope from the Horner plot is calculated to be 174.13psi which in turn results in a permeability of 1,680mD. Note that it was not really necessary to use this information to obtain the permeability as this is available $k = 1{,}614mD$. The fact that these results lie close to each

other is yet another test for the fluid flow model and its implementation. Now, the skin factor which is rather a pseudo-skin factor due to the non-axisymmetric nature of the erosional model here presented would be $S = -4.1$, a simple calculation on the field case reported by Svendson et al., (1991) yields a similar skin factor of -3.04. Also, one can imagine that while injection is ongoing, the pore pressure may provide enough support to keep the eroded formation stable. However, it is hard to understand what happens once the well is shut and both fluid velocity and pore pressure drop, for instance deposition of sand particles into the wellbore may plug the well causing a performance detriment.

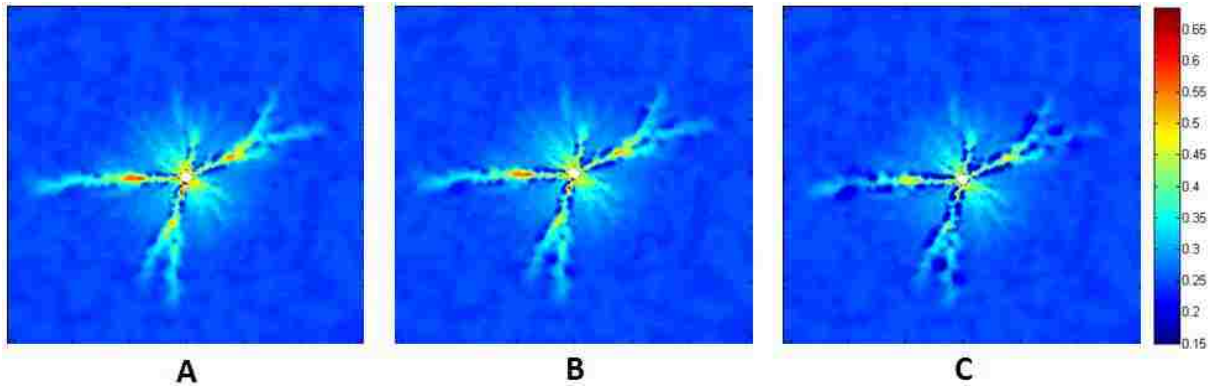

Figure 4-25. Final porosity distribution A) before shut in ,B) after 1hr, and C) after 2hrs

Finally, the porosity distribution after the well is shut entails what happens when the mobile grains stop moving and settle (Figure 4-25). Right before shutting the well, there are regions close to the wellbore of up to 0.66 porosity that in small areas drop to a range between 0.55 and 0.60 after shut-in. On the other hand, the regions relatively away from the wellbore with porosities between 0.35-0.40 end up between 0.30 and 0.35. The grains deposited will slightly decrease the hydraulic conductivity around the wellbore, if the well is restarted, then erosion can be expected but in much lower proportions than during the initial start-up.

Considering the time varying nature of the induced channels just described, it is important to use analysis tools designed for time varying formation properties. The Nolte G-function is usually used to analyze fracture closure during mini-frac tests (Economides et al., 2000) and it is here used to analyze the effect of the grain deposition during shut-in. For high leak-off cases such as injection into these high permeability sands the G-function can be found as,

$$G(\Delta t_D) = \frac{4}{\pi}(\mathrm{g}(\Delta t_D) - \mathrm{g}_0) \qquad \text{Eq.4-4}$$

with,

$$g(\Delta t_D) = (1 + \Delta t_D)^{1.5} \sin^{-1}((1 + \Delta t_D)^{-0.5}) + \Delta t_D^{0.5}, \quad g_0 = \frac{\pi}{2}. \qquad \text{Eq.4-5}$$

Only the pressure derivative with respect to the G-function multiplied by G is presented as it shows the most significant difference between the case with erosion and the one without.

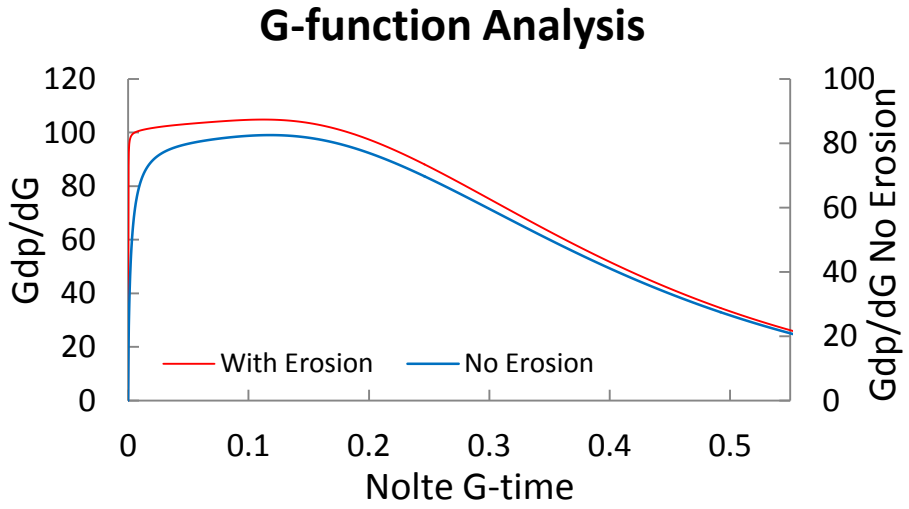

Figure 4-26. Nolte G-function for shut-in periods with erosion (blue) and without erosion (green)

The derivative for the undamaged formation is high at the beginning dropping slowly similarly to the case in which there is erosion. Note that the no erosion case has no positive slope at any point during the falloff. Usually the deviation from an initially upwards trend determines the point when a fracture closes, since there are no formation variations in the simulation, this behavior is absent. On the other hand, in the presence of the erosional model there is initially a steep increment in the G-function derivative that then deviates signaling some variations are taking place in the formation. Instead of falling steeply as in mini-frac tests, the curve decreases slowly. The curve behavior might be explained in the fact that hydraulic conductivity is decreasing as the grains deposit but the change is not as significant or fast as the one in hydraulic fracturing. This could certainly be a key point in the understanding of erosional phenomena in poorly consolidated formations.

4.4 Results in Three Dimensions

The results for different scenarios including vertical and horizontal anisotropy, completions and different formation properties for three dimensions are discussed in this section; a comparison to the solution of the problem in two dimensions is also performed in order to assess the differences that might arise when including the vertical component. Initially, the formation has a heterogeneous porosity of 0.20 with a standard deviation of ± 0.01.

Unlike the simulation in two dimensions, the magnitude for some of the erosion variables is estimated for the implementation to be more realistic. The model parameters are obtained using the dimensionless by Zhang et al. (2013) obtained from experimental results in which fluid was injected into unconsolidated porous media. With over 50 experiments performed, the authors prepared a plot of the area ratio to dimensionless time. The area ratio is defined as the quotient of the eroded area to total area packed with sand in their experimental setup. On the other hand, the dimensionless time (τ_1) is defined as,

$$\tau_1 = \frac{\mu q D_i}{Ek}. \qquad \text{Eq.4-6}$$

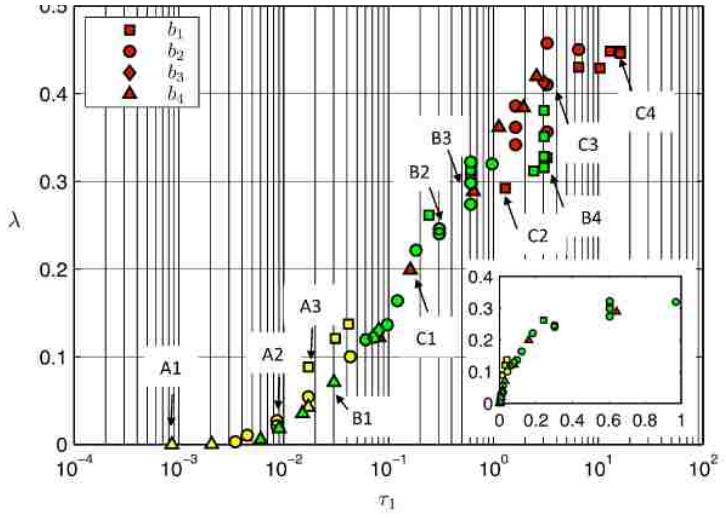

Figure 4-27. Area ratio variation as a function of dimensionless time for multiple fluid injection experiments into poorly consolidated porous media by Zhang et al. (2013)

In Eq.4-6, E is the Young's modulus and D_i is the wellbore radius. The relation of the area ratio and dimensionless time obtained for the entire set of experiments can be seen in Figure 4-27. From this plot, it

can be said that no erosion takes place for dimensionless times smaller than $1x10^{-3}$, concept that can be used as follows to obtain parameters in Eq.2-66. Using a typical Young's modulus for unconsolidated reservoirs of 600,000psi (Ispas et al., 2012), the 7" wellbore in the MESH (Figure 3-8), the permeability obtained through the Carman-Kozeny equation of 1,076mD and a water viscosity of 1cP leaves the velocity at the injection point left. Setting the value of the dimensionless time to $1x10^{-3}$ yields an injection velocity at the wellbore sandface of 4.05E-3ft/s equivalent to a flowrate of 13,500bbl/d for the system here implemented. In the model used no erosion takes place when,

$$\left(C^{-1}(\phi)^{\frac{3}{2}}(\gamma^{-1}\nabla p)^2 - \left(\tanh\left(2\pi(\overline{\phi_s} - 0.6)\right) + 1\right)\right) = 0 \qquad \text{Eq.4-7}$$

With the pressure gradient at the wellbore defined as $\nabla P = q\mu/k$, function of all previously known variables allows computing the erosional parameters $(C * \gamma^2)^{-1}$, if C is given a value of 2 as originally proposed by Mahadevan et al. (2012), then $\gamma \sim 2.2x10^5$.

4.4.1 Comparison of two and three dimensions base scenarios

For this section, the only difference introduced is the value of A increased to 270 to account for the higher tortuosity given the non-uniform particle size distribution of natural occurring formations not considered in the Carman-Kozeny equation. Also, an injection rate 0f 50,000bbl/d is chosen to match the desired injection rate of Well I-1 in Figure 1-1. A base scenario in two dimensions with the reservoir properties equal to those of the three dimensional MESH is simulated. The resulting porosity of the base scenario for erosion in two dimensions is shown in Figure 4-28 where a 10x10ft zoom-in into the formation can be seen.

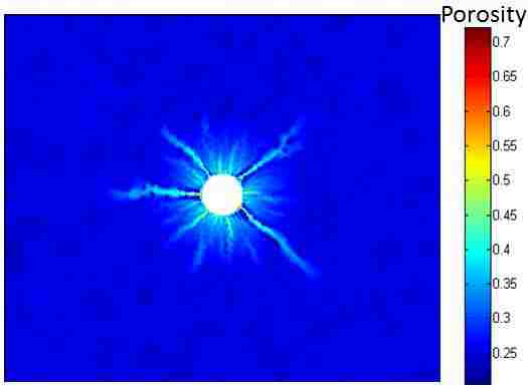

Figure 4-28. Final porosity distribution in two dimensions simulation for comparison to three dimensional simulations.

Four major channels with porosities above 70% close to the wellbore are obtained. A couple inches into the formation the channels attain porosities of under 40% and extend for about 3ft. Several other shorter and not as porous channels develop too having a significant portion of the sand around the wellbore loosened from the matrix. The most noticeable feature of the four major channels is that no erosion is caused on their sides. This observation implies that channels absorb a major fraction of the flow being injected around them which depending on the circumstances could lead to out of zone injection or poor sweep efficiency.

When a simulation in two dimensions is performed, the underlying assumption is that every parameter and resulting datum is spatially the same in the vertical direction. The comparison between two and three dimensions simulations can then be considered extremely important to assess whether it is worth taking the more computationally expensive route of a simulation in three dimensions. The bottomhole pressure readings for two and three dimensions for a well startup with no erosion and with erosion are available in Figure 4-29. The runs use exactly the same parameters which enable the use of the non-erosion runs to evaluate the accuracy and correct implementation of the diffusivity equation. As expected, the downhole pressure as a function of time is almost the same differing by under 1psi for both systems in the absence of erosion.

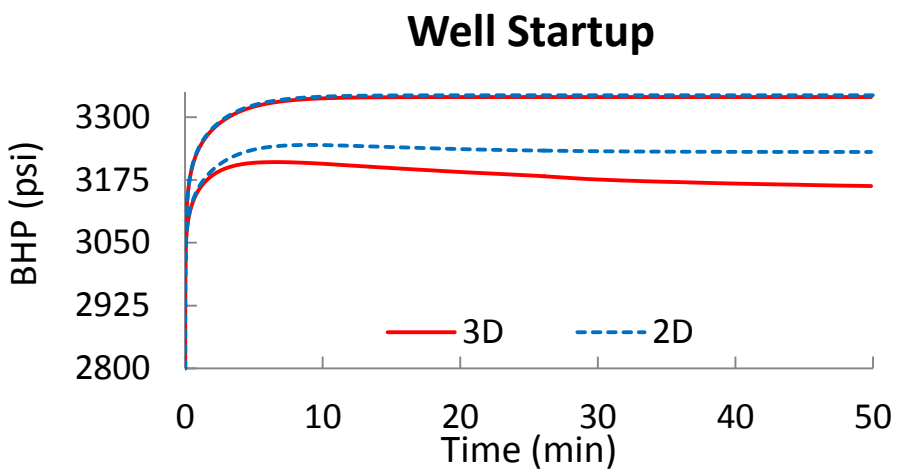

Figure 4-29. Wellbore pressure for two and three dimension with and without erosion.

The case in which the erosion model is included entails a significantly different situation. The pressure readings remain close to each other in the initial two minutes of simulation after which the pressure for the three dimensions case falls under that of the two dimensions to stabilize 70psi lower after 50 minutes. It is important to notice that unlike hydraulic fracturing, channelization does not result in an initial pressure build up followed by a steep sudden drop. The behavior is in line with Hosseini's (2012) experimental observations for cases in which shear failure was detected (Figure 1-4). Field situations in which injection above formation fracturing pressures seem to have no effect also support the idea of having formation failure in the form of channels (Pedroso et al., 2009).

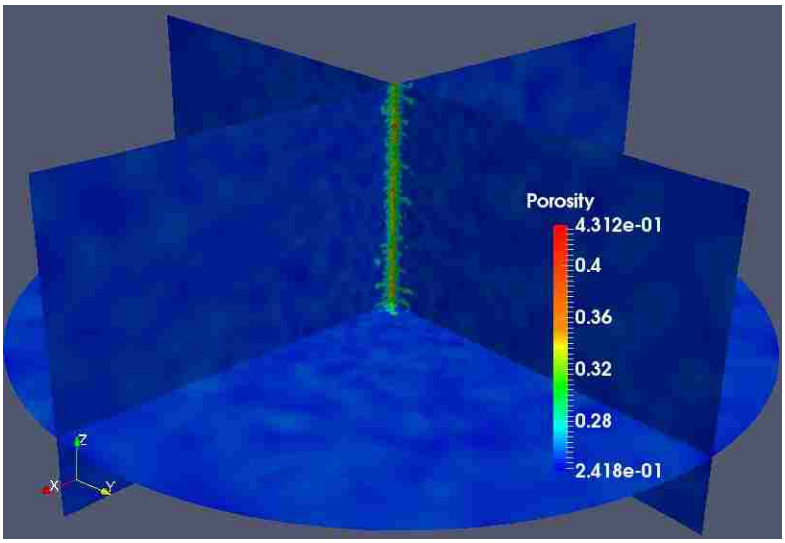

Figure 4-30. Sliced porosity planes for three dimensional eroded formation.

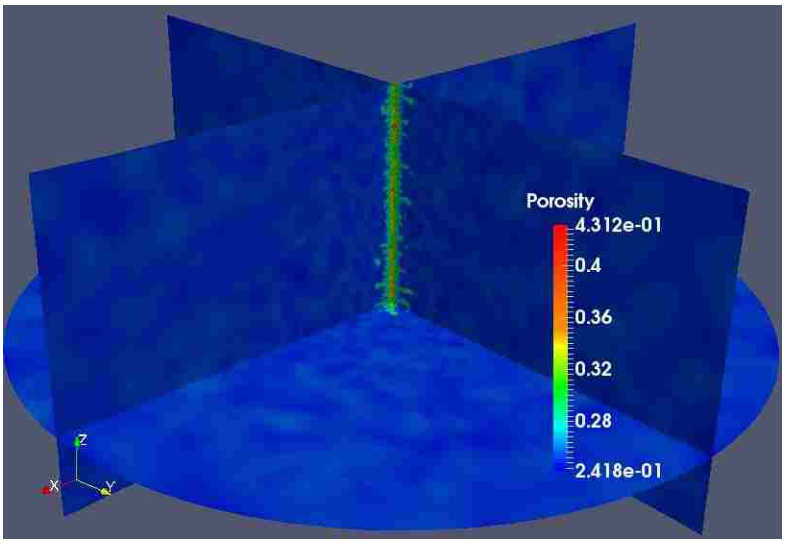

Figure 4-30 contains a sliced view of the reservoir's porosity after 50 minutes of injection. The sliced view consists of three flat planes one on each axes intercepting at zero for X and Y and 35ft above the bottom of the reservoir in the vertical axis. The porosity obtained reveals tubular channels forming away from the wellbore some of which disappear and come back into the different plains. The situation is explained by the tortuosity of the channels in every direction rather than considering that the channels contain discontinuities.

The resulting porosity is also useful in explaining the differences between the pressure readings for two and three dimensional cases. In 2D the recreated phenomenon is that of channels extending the same on the vertical axis, on the other hand, the tubular channels displayed in

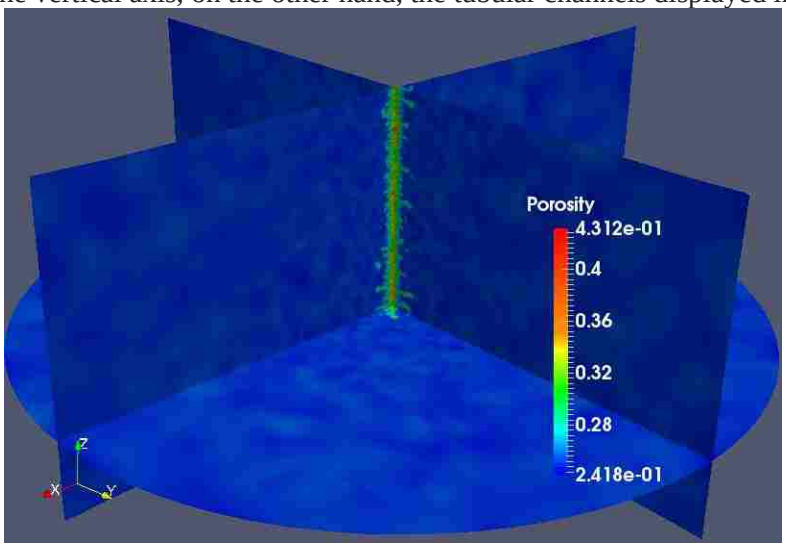

Figure 4-30 occur at an specific depth covering less volume than anticipated by the two dimensional system and resembling the tubulars on the experiments in Figure 1-4. Initially, it could be thought that

this would lead to overall higher pressure readings in the three dimensional system, however the opposite effect is observed. The pressure is lower when all dimensions are accounted because the fluid being injected far from an existing channel will have to travel further before reaching a high conductivity path. The overall effect is that although there is less volume occupied by channels, more erosion takes place close to the wellbore compared to the two dimensional case. The closer to the wellbore erosion occurs, the larger its impact on the wellbore pressure as there is less area open to flow in that region.

4.4.2 Effect of horizontal anisotropy on channelization in three dimensions

Following the comparison of a base scenario for different spatial dimensions, a study of the effect of formation variations can be performed. The first variable to be assessed is the anisotropy of the principle permeabilities matrix (Eq.2-38) which according to Her-Yuan et al. (1998) is proportional to the principal stresses and has maximum to minimum horizontal permeability ratios (k_{H_max}/k_{H_min}) of up to 5 (Bandiziol & Massonnat, 1992). For the present study, a ratio of only 1.5 is used since it proved to be big enough to have a significant influence on the results.

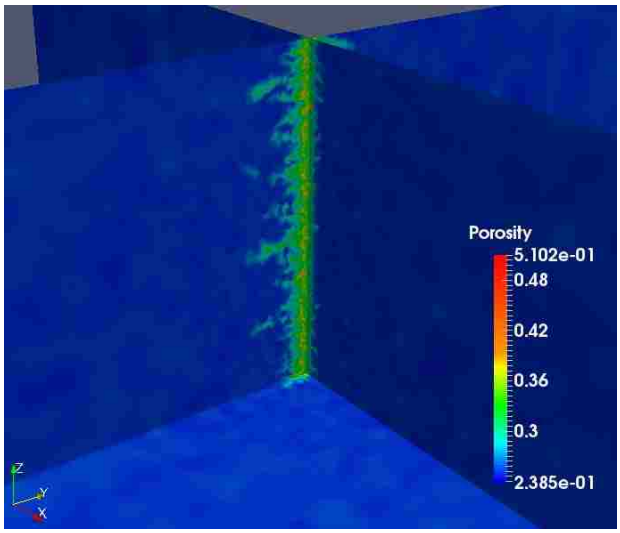

Figure 4-31. Sliced, zoomed-in porosity planes for three dimensional eroded formation with horizontal permeability anisotropy.

The effect of lower permeability on the Y-axis becomes clear in the resulting porosity distribution (Figure 4-31), the channels extend preferably in the direction of lower permeability unlike the more

random distribution found in the isotropic media. The initially higher pressure gradient caused by the anisotropy enhances erosion in a preferred direction which after a point enhances the flow through this path creating longer channels than the ones formed in the base scenario.

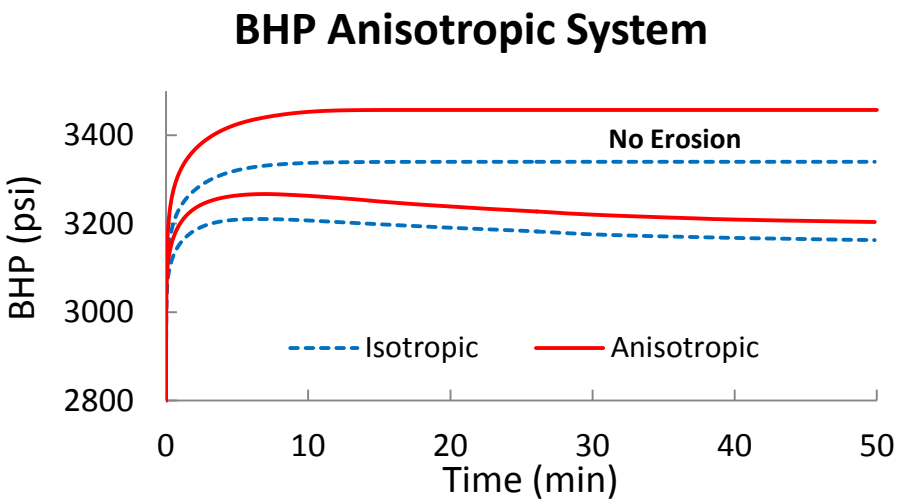

Figure 4-32. Bottomhole pressure for well startup in isotropic and anisotropic.

The bottomhole pressure for the isotropic and horizontally anisotropic cases in Figure 4-32 contains the simulated startups for unaltered systems as well as for eroded ones. As can be expected, the anisotropic non-eroded formation has a higher pressure reading due to the overall lower hydraulic conductivity. The steady state pressures differ by approximately 120psi. On the other hand, the bottomhole pressures resulting from the eroded formations lie closer with only 40psi difference supporting the observation that in the presence of anisotropy more erosion takes place.

4.4.3 Effect of horizontal and vertical anisotropy on channelization in three dimensions

Another foreseeable situation is that of vertical anisotropy having lower vertical permeability induced by the usually maximum principal stress; the overburden. Although horizontal to vertical permeability (k_h/k_v) ratios of as much as 10 have been measured (Bourdarot & Daviau, 1989), a simulation with horizontal to vertical permeability ratio of 2.5 is implemented including the horizontal anisotropy. A contour of the channels formed at the end of the simulation is displayed (Figure 4-33).

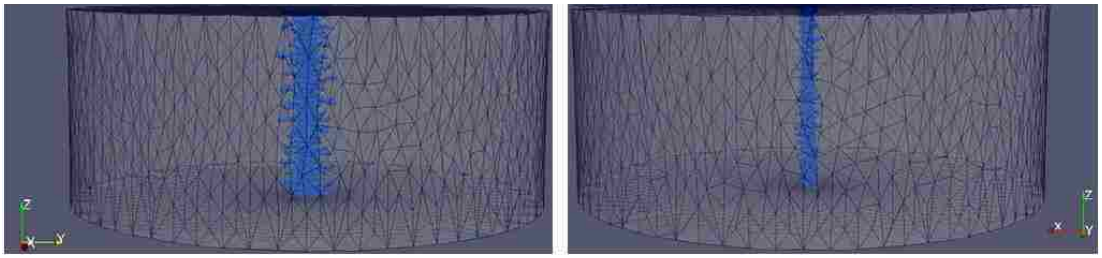

Figure 4-33. Eroded volume contours from different angles parallel to x (left) and parallel to y (right) showing preferential growth of channels in the direction of the minimum horizontal permeability and no effect from the vertical anisotropy.

The contours of the channels formed show that the preferred direction for erosion is parallel to the Y-axis or along the minimum horizontal permeability. While the effect of the horizontal permeability is obvious, it seems like the vertical anisotropy has played a minor role on the development of channels. Since fluid is injected perpendicular to the vertical axis it is expected for the pressure gradient in it to be small having then little to no effect on erosion. This analysis however does not imply that the vertical permeability is irrelevant since situations such as injection in deviated wells could be significantly affected by it. Also, it is important to state that the fluid density has been kept constant while in reality it is a function of the volumetric fraction of solid content carried by the injected fluid. Including the mixture density could alter the results for the previous simulation making the mixture with high eroded grains content drop towards the bottom of the formation due to its heavier weight.

4.4.4 Injection on finite reservoir interval with dissimilar rock strength

Following the application of anisotropy, a run having three layers with different properties was performed. The three layers resistance to channelization was altered by modifying the coefficient C in Eq.2-67. The layers are 20ft each with the middle layer having a coefficient C of 10. As illustrated in Figure 4-34, injection only occurs in the stronger 20ft of the system adding a non-slip boundary condition to the wellbore above and on top of the middle layer.

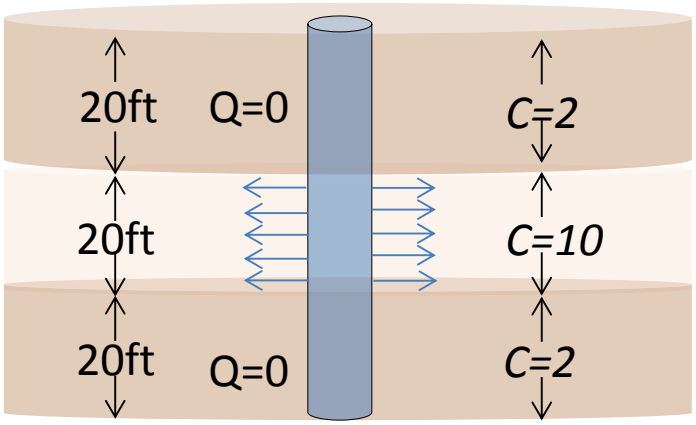

Figure 4-34. Selective injection into a layered formation containing two weaker rocks (top and bottom) with a stronger layer in the middle targeted for injection.

The surface of the eroded volume attained when selectively injecting into the middle and stronger layer of the system is shown in Figure 4-35. The middle layer is delineated by the yellow shadow while the top and bottom sands are outlined by an orange shade. A fairly round and short eroded area close to the wellbore is obtained on the injection interval while the weaker layers show significantly higher erosion. Initially the fluid erodes the vicinity of the wellbore and the top and bottom of the injection interval. This allows the flow to be redirected towards the more prone to erosion intervals. In this case both top and bottom layers erode in similar proportions, however, gravitational effects not accounted for could vary this situation enhancing erosion in one of the layers exclusively. It is hard to reach a conclusion on what would be the situation if gravity was incorporated, one could think for instance that particles eroded in the top layer should fall towards the bottom if the fluid velocity is lower than the particles' settling velocity. During shut-ins, flowback as a result of the pressure pulses induced by the water hammer effect could bring particles into the wellbore. Field studies revealing particles flowing towards the wellbore have been reported and outlined as significant sources of injectivity impairments (Olatunji et al., 2014).

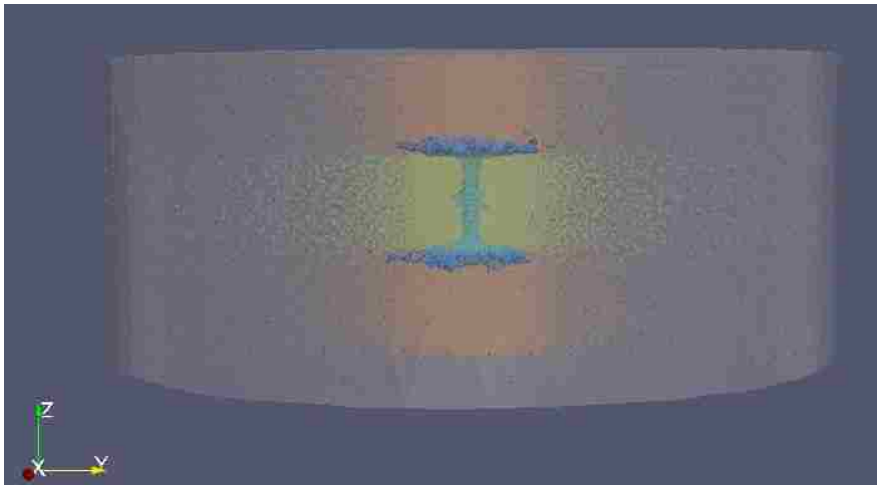

Figure 4-35. Eroded region surface resulting from selective injection in a three-layered system with dissimilar resistance to erosion.

The formation's pressure resulting from injection into the layered system can be seen in Figure 4-36 in a similar fashion to the slices of Figure 4-31. The high to mid pressure contours extend longer at the points of higher erosion at the interphase between the weak and the stronger formations. The higher pressure contours demonstrate how a significant portion of the injected fluid is moving towards weaker formations which could be described as an out of zone injection resulting in poor sweep efficiency.

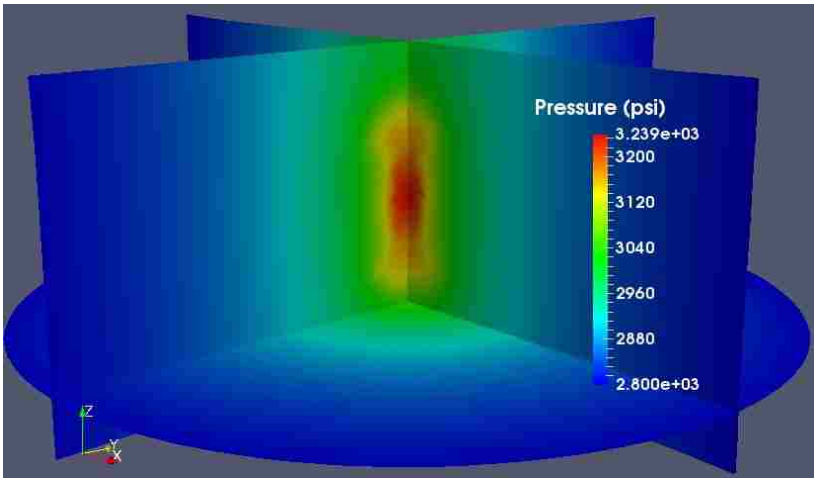

Figure 4-36. Pressure profile indicating higher fluid velocities towards the weaker formations induced by the high erosion levels.

4.4.5 Injection on finite reservoir interval with dissimilar rock strength with vertical and horizontal anisotropy

The surface contours of eroded sand as obtained from injection in the 20ft intermediate interval when vertical and horizontal anisotropy is present elucidates a significant increment in erosion of the weaker top and bottom layers (Figure 4-37). Channels extend very close to the bottom and top of the MESH but remain away from it. The latter is explained by the non-slip boundary condition (Eq.2-42) which sets the pressure gradient at the vertical bounding surfaces to zero hence eliminating erosion. Although the boundary condition could be removed, the situation would be rather unrealistic if channels extend all the way to the boundaries. If a channel reaches a boundary a significant portion of the injected fluid would be suddenly leaving the system through it since it represents a path of infinite conductivity beyond the boundary.

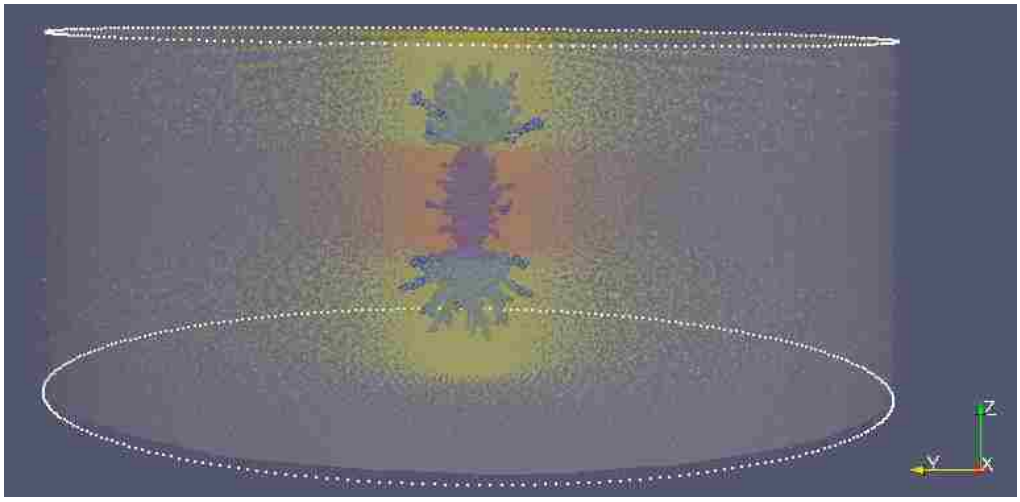

Figure 4-37. Channeling contours of injection in the presence of vertical and horizontal permeability anisotropy.

Although the limitations posed by a finite geometry bound the vertical extension of erosion, it is clear that the system heterogeneities and anisotropy have a profound influence on the areas near to the wellbore suffering erosion. Erosion away from the target zone is then deemed possible in situations in which erosion is promoted at bounding layers, situation that can redirect flow even if injection occurs below formation fracturing pressures. Although multiphase flow is not considered, the situation could

worsen if for instance injection is taking place above an oil-water contact and interfacial and buoyancy effects also redirects flow.

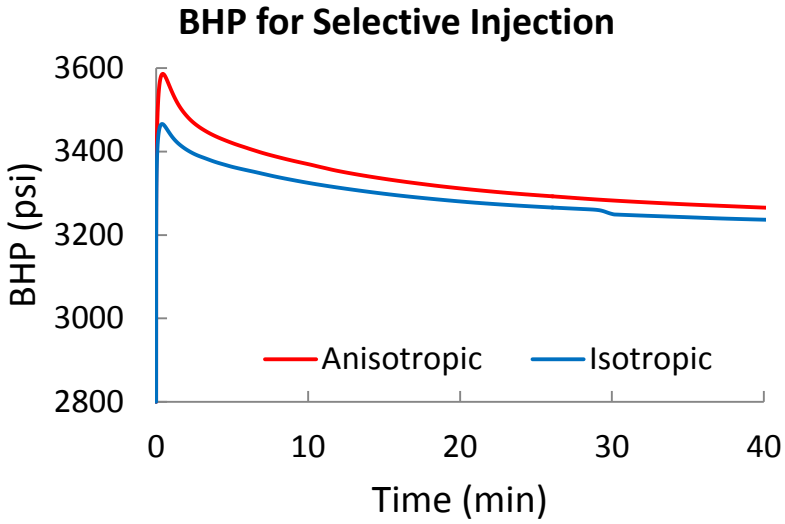

Figure 4-38. Bottomhole pressure obtained from selective injection for isotropic and anisotropic cases.

Finally, the pressure readings for the last two simulations indicate that erosion of the middle layer occurs first. The steep pressure ascent is hindered and actually decreases as injected fluid floods and erodes the top and bottom layers. The anisotropic case remains at higher pressures for most part even when absolute formation eroded volume is higher. This situation is likely due to the poorer connectivity between the wellbore and the highly eroded regions on top and below the wellbore caused by the preferential expansion of channels away from the wellbore in the vertical direction and in a single direction horizontally.

4.5 Dimensionless Analysis on Erosional Phenomena

Different solid's displacement and flow patterns can be expressed from characteristic times for the underlying flow processes (Huang et al., 2012). For instance the characteristic time (t_i) of fluid injection into porous media can be taken as the ratio of the system's characteristic length to injection velocity (L/q). For the diffusion of fluid through porous media and accounting for the medium's poroelasticity (not

considered in this study), the dimensionless time $t_t = \mu L^2/Ek$ can be defined. Now for the erosional phenomenon presented here, one can define the erosion characteristic time as

$$t_\epsilon = \frac{k_e q \mu}{Ck\gamma}. \quad \text{Eq.4-8}$$

The characteristic erosion time can be thought as the rock's resistance to erosion or cohesion between grains to fluid flow induced drag forces. Looking at Eq.2-66 makes it clear that parameter k_e determines how quick erosion occurs. With the above characteristic times stated, a dimensionless time $\tau = t_\epsilon/t_i$ can be determined. This ratio defines the nature of injection between it being erosional driven or simple fluid diffusion across the matrix.

With the dimensionless time established, the multiple simulations under different conditions allow the dimensionless analysis to be implemented. This number should be related then to the total damage caused. For the current case, the damage is quantified as,

$$P_D = \frac{P_e - P_{res}}{P_{NoE} - P_{res}} \quad \text{Eq.4-9}$$

In Eq.4-9, P_e is the pressure reached when the erosional model is on, P_{NoE} is the bottomhole pressure attained when assuming no damage to the formation and P_{res} is the original reservoir pressure. With this definition, it should be noted that $P_D$will be bounded between zero and one with one representing no damage. The formation pressure is subtracted so that only effects under flowing conditions are accounted for. A plot of $P_D$vs. τ for most of the cases presented in this study is available in Figure 4-39,

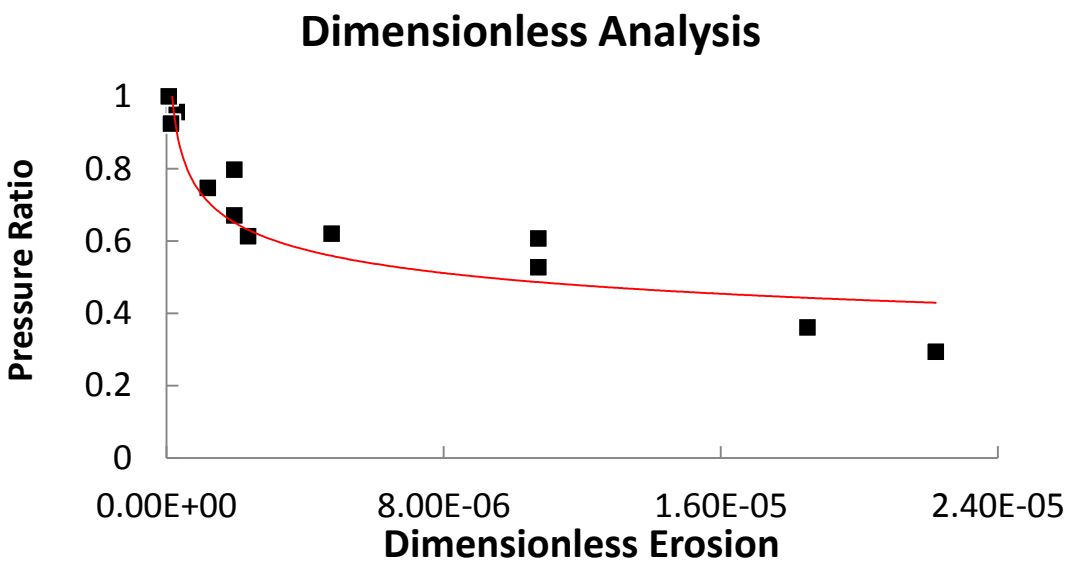

Figure 4-39. Dimensionless analysis of formation damage represented by the pressure ratio and dimensionless erosion time.

The resulting relationship between the dimensionless variables appears to be a power relation. Formation damage is proportional to the dimensionless pressure meaning that the lower the pressure ratio, the more damage caused in a particular simulation. Then higher values of dimensionless erosion represent higher overall erosion. The first data point corresponds to the injection rate for which erosion begins on Figure 4-23. Ultimately, the analysis can be used to estimate parameters for the model or get a sense of possible induced damage at certain flowing conditions.

CHAPTER 5: CONCLUDING REMARKS AND RECOMMENDATIONS

5.1 Concluding Remarks

The potential of having formation failure prompted by fluid injection in the form of individual particle erosion and transport in poorly consolidated reservoirs has been modelled. Unlike most research performed in this area in which damage is attributed to hydraulic fracturing, erosion is capable of explaining the often perceived transport of sediment within the reservoir as well as into the wellbore. Using the pressure gradient as the driving force for particle erosion makes the most physical sense and promotes the field observation that rock failure at really low flowing pressures is possible.

Although qualitatively, the simulated erosion patterns and resulting wellbore pressures obtained are in-line with both experimental results and field observations. The two outstanding observations in this matter are: 1) during a well startup pressure drops as in stimulation treatments in hard rock are not perceived and 2) unlike fractures, erosion due to its nature and driving principle is more likely to create individual tube shape channels than fractures extending vertically throughout the targeted interval.

Some of the theoretical studies on the present subject propose ring-shaped erosion, however, the results obtained demonstrate that this assumption does not hold as erosion can be enhanced in rather random paths resulting from initially weak heterogeneities. Not only is it important to account for the different patterns obtained horizontally but also for the vertical component of these. Even before including the gravitational effects, the three dimensional simulation of formation erosion significantly differentiates itself from that in two dimensions. Also, the simulation of fluid injection in three dimensions allows for more realistic completions geometries and different scenarios usually observed in the field which have a deep impact on the erosion patterns. All together makes of the more computationally expensive three dimensional simulation worth doing.

A model calibration procedure has been developed and different ways of assessing erosion during injection operations through standard well tests have been performed. Under actual injection operations though it is hard to understand what the physical occurrences are once a well undergoing injection and erosion is shut-in. After shut-in, the pore pressure close to the wellbore falls leaving little support to the

voids created through fluid flow induced erosion which may lead to overlaying rock collapse ultimately generating permeability impairments.

Simulations of formation failure when injecting fluid into a formation with vertically varying properties evidences the possibility of out of zone injection. This is the case when injection is promoted in specific layers which may end up establishing connectivity between initially isolated formations. When this is the case, the EOR objectives of increasing oil sweep and reservoir pressure maintenance may not be achieved compromising the economic yield of a project.

Given the observations in the present study, it can be stated that formation damage during injection operations might be avoided by promoting well design concepts that minimize the pressure gradient at the wellbore sandface and its surroundings. For instance, absolute injection rates are not the most important consideration in this regard but rather the injection velocity. Desirably lower injection velocities can be obtained by having longer completed zones with more and bigger perforations in cased holes. Historically, injectors' completions intend to have as high permeability as achievable while keeping the proppant size six times that of the original formation sand. However, this leads to high pressure gradients in different areas around the completed zone promoting formation failure which creates voids that can absorb the completions. Completions displaced away from the wellbore can lose communication with the wellbore decreasing the injectivity. Completions, especially frac-packs should be designed to evenly distribute flow across their interphase with the formation. Designing wells bearing the concepts elucidated may yield more resilient wells and improve entire fields' performance.

5.2 Recommendations

Some assumptions which may affect the effective results have been made while performing this theoretical study. Removing all or some of these assumptions may be an important step towards improving the quality of the results obtained. However, assessing the need and relevance of each step taken forward towards a more complete solution is important to assure the problem remains of proper size given the resources available.

Rather than having constant formation compressibility, this can be made porosity dependent through multiple correlations available. An effect of the formation compressibility is expected on the diffusivity equation changing the flowing conditions as calculated in the finite element code.

The dynamic viscosity should vary depending on the eroded particle concentration. Correlations for such purpose are widely available in completions books for calculating the viscosity of completion fluids carrying proppants. Aside from being a more realistic approach, the incorporation of a varying viscosity relaxes the assumption of having equal fluid and mobile grain velocity.

Similarly to the past two observations but exclusive of the three dimensional formulation, having varying density relative to the volumetric concentration of mobile sand will make the gravitational term in the diffusivity equation to have an effect on the results. A weighted average of the fluid and sand grains dependent on their volumetric fraction in pore space may be enough for an accurate yet simple calculation. Steps back in the formulated boundary value problem have to be taken reversing the implementation of the flowing potential concept.

A more consistent proposition for the deposition model should be taken. It is clear that particle deposition is a function of hydrodynamic principles not incorporated in the current model. Coming to such a solution should not pose a big challenge but the impact on the results is rather unclear.

An additional modification that could be performed to the model is the computation of formation stresses. The latter is probably one of the most computationally expensive changes that could be performed adding multiple degrees of freedom to the problem formulation. Although computationally expensive, the compressional stresses are probably one of the most significant missing items on the formulation here presented.

REFERENCES

fshar, M. H., & Rohani, M. (2008). Water hammer simulation by implicit method of characteristic. *International Journal of Pressure Vessels and Piping*, *85*(12), 851–859.

Al-Abduwani, F. A. H., Bedrikovetsy, P., Farajzadeh, R., van den Broek, W., & Currie, P. K. (n.d.). External Filter Cake Erosion: Mathematical Model and Experimental Study. Society of Petroleum Engineers. http://doi.org/10.2118/94635-MS

Alkindi, A., Prince-Wright, R., Moore, W. R., Walsh, J. M., Morgenthaler, L. N., & Kuijvenhoven, C. (2008). Challenges for waterflooding in a deepwater environment. *SPE Production & Operations*, *23*(03), 404–410.

Ameen, S., & Dahi Taleghani, A. (2015). Dynamic Modeling of Channel Formation During Fluid Injection Into Unconsolidated Formations. *SPE Journal*, (20(4)), 689–700.

Åström, B. T., Pipes, R. B., & Advani, S. G. (1992). On flow through aligned fiber beds and its application to composites processing. *Journal of Composite Materials*, *26*(9), 1351–1373.

Bachman, R. C., Harding, T. G., Settari, A. T., & Walters, D. A. (2003). Coupled Simulation of Reservoir Flow Geomechanics and Formation Plugging With Application to High-Rate Produced Water Reinjection. In *SPE Reservoir Simulation Symposium*. Society of Petroleum Engineers.

Bandiziol, D., & Massonnat, G. (1992). Horizontal Permeability Anisotropy Characterization by Pressure Transient Testing and Geological Data. http://doi.org/10.2118/24667-MS

Beheshti, A. A., & Ataie-Ashtiani, B. (2008). Analysis of threshold and incipient conditions for sediment movement. *Coastal Engineering*, *55*(5), 423–430.

Bonnefille, R. (1963). Essais de synthese des lois de debut d'entrainment des sediment sous l'action d'un courant en regime uniform. *Bull. Du CREC*, *5*.

Bourdarot, G., & Daviau, F. (1989). Vertical permeability: Field cases. In *SPE Annual Technical Conference and Exhibition*. Society of Petroleum Engineers.

Cao, Z., Pender, G., & Meng, J. (2006). Explicit formulation of the Shields diagram for incipient motion of sediment. *Journal of Hydraulic Engineering*, *132*(10), 1097–1099.

Chappell, S. D. (2006). Waterflooding in Deepwater Environments. Offshore Technology Conference. http://doi.org/10.4043/18345-MS

Charlez, P., Lemonnier, P., Ruffet, C., Boutéca, M. J., & Tan, C. (1996). Thermally induced fracturing: analysis of a field case in North Sea. In *European Petroleum Conference*. Society of Petroleum Engineers.

Cheng, N.-S. (2004). Analysis of bedload transport in laminar flows. *Advances in Water*

Resources, *27*(9), 937–942.

Cheremisinoff, N. P. (1998). *Liquid filtration*. Butterworth-Heinemann.

Chien, N. (1801). Mechanics of sediment transport. Institute of Water Resources and Hydro-Power Research Translated under the guidance of John S. McNown Late Engineering College Dean, University of Kansas.

Chin, L. Y., & Montgomery, C. T. (2004). A numerical model for simulating solid waste injection in soft rock reservoirs. In *SPE Annual Technical Conference and Exhibition*. Society of Petroleum Engineers.

Choi, S.-K., & Huang, W. S. (2011). Impact of Water Hammer in Deep Sea Water Injection Wells. In *SPE Annual Technical Conference and Exhibition*. Society of Petroleum Engineers.

Clifford, P. J., Berry, P. J., & Gu, H. (1991). Modeling the vertical confinement of injection-well thermal fractures. *SPE Production Engineering*, *6*(04), 377–383.

Dahm, T., Manthei, G., & Eisenblätter, J. (1998). Relative moment tensors of thermally induced microcracks in salt rock. *Tectonophysics*, *289*(1), 61–74.

Dancey, C. L., Diplas, P., Papanicolaou, A., & Bala, M. (2002). Probability of individual grain movement and threshold condition. *Journal of Hydraulic Engineering*, *128*(12), 1069–1075.

Delshad, M., Kim, D. H., Magbagbeola, O. A., Huh, C., Pope, G. A., & Tarahhom, F. (2008). Mechanistic interpretation and utilization of viscoelastic behavior of polymer solutions for improved polymer-flood efficiency. In *SPE Symposium on Improved Oil Recovery*. Society of Petroleum Engineers.

Dusseault, M. B. (2010). Deep injection disposal: environmental and petroleum geomechanics. In *ISRM International Symposium-6th Asian Rock Mechanics Symposium*. International Society for Rock Mechanics.

Economides, M. J., Nolte, K. G., Ahmed, U., & Schlumberger, D. (2000). *Reservoir stimulation* (Vol. 18). Wiley Chichester.

Ehlig-Economides, C., Ebbs, D., & Meehan, D. N. (1990). Factoring anisotropy into well design. *Oilfield Review*, 24–33.

Gadde, P. B., & Sharma, M. M. (2001). Growing injection well fractures and their impact on waterflood performance. In *SPE Annual Technical Conference and Exhibition*. Society of Petroleum Engineers.

Garon, A. M., Lin, C. Y., & Dunayevsky, V. A. (1988). Simulation of Thermally Induced Waterflood Fracturing in Prudhoe Bay. In *SPE California Regional Meeting*. Society of

Petroleum Engineers.

Germanovich, L. N., Hurt, R. S., Ayoub, J. A., Siebrits, E., Norman, D., Ispas, I., & Montgomery, C. T. (2012). Experimental study of hydraulic fracturing in unconsolidated materials. In *SPE International Symposium and Exhibition on Formation Damage Control*. Society of Petroleum Engineers.

Golovin, E., Chudnovsky, A., Dudley, J. W., & Wong, G. K. (2011). Injection rate effects on waterflooding mechanisms and injectivity in cohesionless sand. In *45th US Rock Mechanics/Geomechanics Symposium, San Francisco, California* (pp. 26–29).

Gravanis, E., Sarris, E., & Papanastasiou, P. (2015). Hydro-mechanical erosion models for sand production. *International Journal for Numerical and Analytical Methods in Geomechanics*.

Greyvenstein, G. P. (2002). An implicit method for the analysis of transient flows in pipe networks. *International Journal for Numerical Methods in Engineering*, *53*(5), 1127–1143.

Guo, Q., Abou-Sayed, A. S., & Engel, H. R. (2007). Feeling the Pulse of Drill Cuttings Injection Wells-A Case Study of Simulation Monitoring and Verification in Alaska. *SPE Journal*, *12*(04), 458–467.

Han, G., Ioannidis, M., & Dusseault, M. B. (2003). Semi-analytical solutions for the effect of well shut-down on rock stability. *Journal of Canadian Petroleum Technology*, *42*(12), 46–53.

Henthorne, L., Martin, C., & Satar, F. A. A. (2013). Maximizing Oil Recovery-Developing and Piloting Offshore Facilities to Customize Water for CEOR and Low Salinity Injection. In *IOR 2013-From Fundamental Science to Deployment*.

Her-Yuan, C., Hidayati, D. T., & Teufel, L. W. (1998). Estimation of Permeability Anisotropy and Stress Anisotropy From Interference Testing. Society of Petroleum Engineers. http://doi.org/10.2118/49235-MS

Herzig, J. P., Leclerc, D. M., & Goff, P. Le. (1970). Flow of suspensions through porous media—Application to deep filtration. *Industrial & Engineering Chemistry*, *62*(5), 8–35.

Hosseini, S. M. (2012). Hydraulic fracture mechanism in unconsolidated formations.

Hu, B., Sagen, J., Chupin, G., Haugset, T., Ek, A., & Sommersel, T. (2007). Integrated Wellbore-Reservoir Dynamic Simulation. In *Asia Pacific Oil and Gas Conference and Exhibition*. Society of Petroleum Engineers.

Huang, H., Zhang, F., Callahan, P., & Ayoub, J. (2012). Granular fingering in fluid injection into dense granular media in a Hele-Shaw cell. *Physical Review Letters*, *108*(25), 258001.

Huang, H., Zhang, F., Callahan, P., & Ayoub, J. A. (2011). Fluid injection experiments in two-

dimensional porous media. In *SPE Hydraulic Fracturing Technology Conference*. Society of Petroleum Engineers.

Hughes, T. J. R. (2012). *The finite element method: linear static and dynamic finite element analysis*. Courier Corporation.

Hustedt, B., Zwarts, D., Bjoerndal, H.-P., Al-Masfry, R. A., & van den Hoek, P. J. (2008). Induced fracturing in reservoir simulations: application of a new coupled simulator to a waterflooding field example. *SPE Reservoir Evaluation & Engineering*, *11*(03), 569–576.

Ispas, I., Eve, R., Hickman, R., Keck, R. G., Willson, S. M., & Olson, K. E. (2012). Laboratory Testing and Numerical Modelling of Fracture Propagation from Deviated Wells in Poorly Consolidated Formations. In *SPE Annual Technical Conference and Exhibition*. Society of Petroleum Engineers.

Khodaverdian, M., Sorop, T. G., Van den Hoek, P. J., Sathyamoorthy, S., & Okoh, E. (2010). Injectivity and fracturing in unconsolidated sand reservoirs: Waterflooding case study, offshore Nigeria. In *44th US Rock Mechanics Symposium and 5th US-Canada Rock Mechanics Symposium*. American Rock Mechanics Association.

Khodaverdian, M., Sorop, T., Postif, S., & Van den Hoek, P. (2009). Polymer Flooding in Unconsolidated Sand Formations–Fracturing and Geomechanical Considerations (SPE-121840). In *71st EAGE Conference & Exhibition*.

Larock, B. E., Jeppson, R. W., & Watters, G. Z. (1999). *Hydraulics of pipeline systems*. CRC press.

Lee, J. (1982). *Well testing*. New York: Society of Petroleum Engineers.

Lee, K., Huh, C., & Sharma, M. M. (2011). Impact of Fractures Growth on Well Injectivity and Reservoir Sweep during Waterflood and Chemical EOR Processes. In *SPE Annual Technical Conference and Exhibition*. Society of Petroleum Engineers.

Liu, H.-K. (1957). Mechanics of sediment-ripple formation. *Journal of the Hydraulics Division*, *83*(2), 1–23.

Luo, Z., & Bryant, S. L. (2010). Influence of thermo-elastic stress on CO2 injection induced fractures during storage. In *SPE International Conference on CO2 Capture Storage and Utilization*. Society of Petroleum Engineers.

Mahadevan, A., Orpe, A. V, Kudrolli, A., & Mahadevan, L. (2012). Flow-induced channelization in a porous medium. *EPL (Europhysics Letters)*, *98*(5), 58003.

McCabe, W. L., Smith, J. C., & Harriott, P. (1993). *Unit operations of chemical engineering* (Vol. 5). McGraw-Hill New York.

McDowell-Boyer, L. M., Hunt, J. R., & Sitar, N. (1986). Particle transport through porous media. *Water Resources Research*, *22*(13), 1901–1921.

McLennan, J. D., & Abou-Sayed, A. S. (2002). Some advances in near wellbore geomechanics. In *SPE/ISRM Rock Mechanics Conference*. Society of Petroleum Engineers.

Mondal, S. (2011). Pressure transients in wellbores: water hammer effects and implications for fracture diagnostics.

Munoz Mazo, E. O., Montoya Moreno, J. M., & Schiozer, D. J. (2007). Study of Sweep Efficiency of Water Injection Under Fracturing-Conditions Process. In *Latin American & Caribbean Petroleum Engineering Conference*. Society of Petroleum Engineers.

Mutlu Sumer, B., Hatipoglu, F., Fredsøe, J., & Kaan Sumer, S. (2006). The sequence of sediment behaviour during wave-induced liquefaction. *Sedimentology*, *53*(3), 611–629.

Norman, W. D., & McCarty, R. A. (2006). The Resiliency of Frac-Packed Subsea Injection Wells. In *SPE Annual Technical Conference and Exhibition*. Society of Petroleum Engineers.

Olatunji, I., Ogunsina, O., Okosun, J., Kazeem, L., Ajayi, A., Adenuga, A., & Abiola, O. (2014). Managing Injectors Impairment in a Deepwater Field. In *SPE Nigeria Annual International Conference and Exhibition*. Society of Petroleum Engineers.

Paige, R. W., & Murray, L. R. (1994). Re-injection of produced water-Field experience and current understanding. *Rock Mechanics in Petroleum Engineering*.

Paphitis, D. (2001). Sediment movement under unidirectional flows: an assessment of empirical threshold curves. *Coastal Engineering*, *43*(3), 227–245.

Pedenaud, P. (2014). Water Injection the FLEX Filtration Solution. In *SPE Oilfield Water Management Conference and Exhibition*. Society of Petroleum Engineers.

Pedroso, C. A., Marques, L. C. do C., Pires, P. R. D. M., Paixao, L. C., & Luz Jr, E. B. (2009). Analysis of Fracture Growth Induced by the Injection of Water Above the Fracture Pressure in Nonconsolidated Sandstones and Soft Carbonates-Deviations from the Linear Elastic Elastic Model or Why Can't I Inject Even Above the Fracture Pressure? In *8th European Formation Damage Conference*. Society of Petroleum Engineers.

Penberthy, W. L., & Shaughnessy, C. M. (1992). *Sand control*. Richardson, TX: Henry L. Doherty Memorial Fund of AIME, Society of Petroleum Engineers.

Perkins, T. K., & Gonzalez, J. A. (1982). Effect of thermoelastic stresses on injection well fracturing. *Soc. Pet. Eng. AIME, Pap.;(United States)*.

Persson, P.-O., & Strang, G. (2004). A simple mesh generator in MATLAB. *SIAM Review*,

46(2), 329–345.

Prasad Saripalli, K., Bryant, S. L., & Sharma, M. M. (1999). Role of fracture face and formation plugging in injection well fracturing and injectivity decline. In *SPE/EPA exploration and production environmental conference* (pp. 415–430).

Rajagopalan, R., & Tien, C. (1976). Trajectory analysis of deep-bed filtration with the sphere-in-cell porous media model. *AIChE Journal*, *22*(3), 523–533.

Roque, C., Chauveteau, G., Renard, M., Thibault, G., Bouteca, M., & Rochon, J. (1995). Mechanisms of formation damage by retention of particles suspended in injection water. In *European formation damage control conference* (pp. 329–343).

Santarelli, F. J., Sanfilippo, F., Embry, J.-M., White, M., & Turnbull, J. B. (2011). The Sanding Mechanisms of Water Injectors and their QUantification in Terms of Sand Production: Example of the Buuzard Field (UKCS). In *SPE Annual Technical Conference and Exhibition*. Society of Petroleum Engineers.

Schrefler, B. A., & Lewis, R. W. (1998). *The finite element method in the static and dynamic deformation and consolidation of porous media*. John Wiley.

Sheppard, D. M., & Renna, R. (2005). Florida bridge scour manual. *Department of Transportation, 605*.

Shields, A. (1936). *Anwendung der Aehnlichkeitsmechanik und der Turbulenzforschung auf die Geschiebebewegung*. Preussischen Versuchsanstalt für Wasserbau.

Shutong, P., & Sharma, M. M. (1997). A model for predicting injectivity decline in water-injection wells. *SPE Formation Evaluation*, *12*(03), 194–201.

Silin, D. B., & Patzek, T. W. (2001). Control model of water injection into a layered formation. *SPE Journal*, *6*(03), 253–261.

Skartsis, L., Khomami, B., & Kardos, J. L. (1992). Resin flow through fiber beds during composite manufacturing processes. Part II: numerical and experimental studies of Newtonian flow through ideal and actual fiber beds. *Polymer Engineering & Science*, *32*(4), 231–239.

Slevinsky, B. A. (2002). A model for analysis of injection-well thermal fractures. In *SPE Annual Technical Conference and Exhibition*. Society of Petroleum Engineers.

Souilah, R., Ourir, A., Brocart, B., Pourpak, H., Ochi, J., Onaisi, A., & Lescanne, H. (2014). Produced Water Re-Injection in a Deep Offshore Environment-Angola Block 17. In *SPE International Symposium and Exhibition on Formation Damage Control*. Society of Petroleum Engineers.

Spiegelman, M. (1993). Flow in deformable porous media. Part 1 Simple analysis. *Journal of Fluid Mechanics*, *247*, 17–38.

Stevens, D. G., Murray, L. R., & Shah, P. C. (2000). Predicting Multiple Thermal Fractures in Horizontal Injection Wells; Coupling of a Wellbore and a Reservoir Simulator. In *SPE/DOE Improved Oil Recovery Symposium*. Society of Petroleum Engineers.

Suman, G. O., Ellis, R. C., & Snyder, R. E. (1983). *Sand Control Handbook: Prevent Production Losses and Avoid Well Damage with These Latest Field-proven Techniques*. Gulf Publishing Company, Book Division.

Svendson, A. P., Wright, M. S., Clifford, P. J., & Berry, P. J. (1991). Thermally induced fracturing of Ula water injectors. *SPE Production Engineering*, *6*(04), 384–390.

Tang, L., & Luo, P. (1998). The Effect of the Thermal Stress on Wellbore Stability. In *SPE India Oil and Gas Conference and Exhibition*. Society of Petroleum Engineers.

Tang, Y., & Ouyang, L.-B. (2010). A Dynamic Simulation Study of Water Hammer for Offshore Injection Wells To Provide Operation Guidelines. *SPE Production & Operations*, *25*(04), 509–523.

Tovar, J. J., & Navarro, W. (2008). The Impact of sandstone strength's behaviour as a result of temperature changes in Water Injectors. In *Europec/EAGE Conference and Exhibition*. Society of Petroleum Engineers.

Turekhanov, B., Bennaceur, H., Currie, P. K., Wolf, K.-H., & De Zwart, A. H. (2007). Particle trapping sequence during filtercake build-up revealed by coloured tracer particles. In *European Formation Damage Conference*. Society of Petroleum Engineers.

Van den Hoek, P. J., Matsuura, T., de Kroon, M., & Gheissary, G. (1999). Simulation of Produced Water Reinjection Under Fracturing Conditions. *SPE Production & Facilities*, *14*(03), 166–176.

van Oort, E., Van Velzen, J. F. G., & Leerlooijer, K. (1993). Impairment by suspended solids invasion: testing and prediction. *SPE Production & Facilities*, *8*(03), 178–184.

Vaziri, H. H., Nouri, A., Hovem, K. A., & Wang, X. (2008). Computation of sand production in water injectors. *SPE Production & Operations*, *23*(04), 518–524.

Walsh, M. P., Bryant, S. L., Schechter, R. S., & Lake, L. W. (1984). Precipitation and dissolution of solids attending flow through porous media. *AIChE Journal*, *30*(2), 317–328.

Walters, D. A., Settari, A., & Kry, P. R. (2002). Coupled geomechanical and reservoir modeling investigating poroelastic effects of cyclic steam stimulation in the Cold Lake reservoir. *SPE Reservoir Evaluation & Engineering*, *5*(06), 507–516.

Wang, D., Seright, R. S., Shao, Z., & Wang, J. (2007). Key Aspects of Project Design for Polymer Flooding. In *SPE Annual Technical Conference and Exhibition*. Society of Petroleum Engineers.

Wang, X., Hovem, K. A., Moos, D., & Quan, Y. (2008). Water Hammer Effects on Water Injection Well Performance and Longevity. In *SPE International Symposium and Exhibition on Formation Damage Control*. Society of Petroleum Engineers.

Wang, Y., Wang, D., Sun, Z., Shi, C., Wang, G., & Li, D. (2004). Hydraulic fracturing of polymer injection wells. In *SPE Asia Pacific Oil and Gas Conference and Exhibition*. Society of Petroleum Engineers.

Webb, T., Omar, N. F., Daungkaew, S., Lim, L. C., Tibbles, R. J., Munoz, I. J., & Morales, H. (2009). Eliminating the Poroelastic Problems Associated with Water Injection in the Kikeh Deep Water Development. In *8th European Formation Damage Conference*. Society of Petroleum Engineers.

Wennberg, K. E., & Sharma, M. M. (1997). Determination of the filtration coefficient and the transition time for water injection wells. In *European formation damage conference* (pp. 353–364).

William, C. L., & Gary, J. P. (2005). Standard handbook of petroleum and natural gas engineering. *Elsevier*, 194–255.

Wright, C. A., Conant, R. A., Golich, G. M., Bondor, P. L., Murer, A. S., & Dobie, C. A. (1995). Hydraulic fracture orientation and production/injection induced reservoir stress change in diatomite waterfloods. In *Society of Petroleum Engineers. Western regional meeting* (pp. 139–152).

Wu, W., & Wang, S. S. Y. (2006). Formulas for sediment porosity and settling velocity. *Journal of Hydraulic Engineering*, *132*(8), 858–862.

Wylie, E. B., Streeter, V. L., & Suo, L. (1993). *Fluid transients in systems*. Prentice Hall Englewood Cliffs, NJ.

Zhang, F., Damjanac, B., & Huang, H. (2013). Coupled discrete element modeling of fluid injection into dense granular media. *Journal of Geophysical Research: Solid Earth*, *118*(6), 2703–2722.

VITA

Juan Felipe Bautista was born in Bogota, Colombia on September 1990. He obtained his Bachelors of Science in Chemical Engineering from Universidad de los Andes in the Colombian Capital in October 2013. He joined the Craft and Hawkins Department of Petroleum Engineering part of Louisiana State University to pursue his Master's degree in Petroleum Engineering where he performed theoretical research on poorly cemented formations' failure due to liquid injection.